

Extraction of Single and Double Differential Cross-Sections on Argon for CC1 μ 2p0 π Event Topologies in the SBND

Emilio Peláez Cisneros

July 22, 2024

Abstract

The precise measurement of cross-sections for a variety of interactions is critical to the success of upcoming flagship neutrino experiments. Of special interest are neutrino interactions that leave the nucleus in a 2-particle 2-hole state (2p2h). This note will present cross-section measurements for the production of 2p2h states on Argon. Using SBND data collected from the **period** of operation, we select events corresponding to a charged-current ν_μ interaction that left the Argon nucleus in a 2p2h state. These interactions produce a topology with one muon and two protons in the final state (CC1 μ 2p0 π). This analysis targets both single differential and double differential cross-section measurements for CC1 μ 2p0 π event topologies in a variety of kinematic variables. Comparisons are made to a set of theoretical models that explore different cross-section modeling configurations. Code for this analysis is available on [GitHub](#).

Contents

1	Introduction and motivation	2
2	Generator analysis	2
2.1	Signal definition	2
2.2	Generators	2
2.3	Variables definition	3
2.4	Pre-FSI events	16
2.5	Double differential plots	16
2.6	Pure MEC events	16
3	SBND analysis	32
3.1	Fiducial volume	32
3.2	Signal definition	32
3.3	Variable plots	33
3.4	Signal efficiency	33
3.5	Migration and response matrices	33
3.6	Systematics	35
4	Closure test	46
5	Cross-section results	46
6	Appendices	49
6.1	Cross section systematics	49
7	References	62

1 Introduction and motivation

2 Since many current and next generation neutrino oscillation experiments will utilize dense nuclear targets,
3 such as liquid argon (LAr), it is critical to characterize the impact of nuclear effects on neutrino cross-sections.
4 One area of interest are neutrino events that eject 2 nucleons from the nucleus, leaving it with 2 holes: known
5 as 2-particle 2-hole states (2p2h). The general picture is that the neutrino has a charged-current interaction
6 with a neutron in the nucleus, producing a proton with significant momentum; this proton interacts with
7 another proton, producing the 2p2h state. While the majority of 2p2h states are caused by Meson Exchange
8 Currents (MEC) [15], some nuclear effects, such as Short-Range Nucleon-Nucleon correlations (SRC) [10],
9 can also produce these states. In an accelerator-based liquid argon time projection chamber (LArTPC)
10 experiment, such as SBND, a charged-current (CC) muon neutrino (ν_μ) interaction that results in a 2p2h
11 state would have a final state topology of 1 muon, 2 protons, and no charged or neutral pions. While
12 there are existing measurements of CC1 μ 2p0 π events on argon, the analyses were statistically limited and
13 no cross-sections were extracted [1, 19]. There was a previous report with single differential cross-section
14 measurements from the MicroBooNE detector [20], but this document presents the first double differential
15 cross-section measurements of CC1 μ 2p0 π topologies on argon, using data collected from the period of SBND
16 operations.

17 2 Generator analysis

18 2.1 Signal definition

19 We choose charged-current muon neutrino interactions that result in one muon, two protons, no charged pions
20 with $P_\pi > 70$ MeV/c, no neutral pions or heavier mesons, and any number of neutrons. These interactions
21 are denoted as CC1 μ 2p0 π . We require the momentum of the muon and protons to be in the following ranges
22 (in MeV/c):

$$100 < P_P < 1200 \quad 300 < P_\mu < 1000 \quad (1)$$

23 2.2 Generators

24 The following generators are used to create events, which are then discriminated using the signal definition
25 above: NuWro, GiBUU, NEUT, GENIE G18, GENIE AR23. Information about these generators is
26 summarized in Table 1.

Name	Generator/Configuration
G18	GENIE v3.0.6 G18_10a_02_11a
AR23	G18 with SuSAv2 MEC model
NuWro	NuWro 19.02.1
NEUT	NEUT v5.4.0
GiBUU	GiBUU 2021

Table 1: Generator and configuration data.

27 The GENIE configurations we used are:

- 28 (i) GENIE G18 [2, 3]: This modern model configuration uses the local Fermi gas (LFG) model [9],
29 the Nieves CCQE scattering prescription [23], which includes Coulomb corrections for the outgoing
30 muon [11], and random phase approximation (RPA) corrections [22]. Additionally, it uses the
31 Nieves MEC model [25], the KuzminLyubushkin-Naumov Berger-Sehgal RES [6, 27, 16], Berger-Sehgal
32 COH [7] and Bodek-Yang DIS [28] scattering models with the PYTHIA [26] hadronization part, and
33 the hA2018 FSI model [4].
- 34 (ii) GENIE AR23: Same as the G18 model configuration but using the SuSAv2 MEC model.

35 The alternative event generators are:

- 36 (i) NuWro [12]: Includes the LFG model [9], the Llewellyn Smith model for QE events [18], the Nieves
37 model for MEC events [24], the AdlerRarita-Schwinger formalism to calculate the Δ resonance explicitly [13],
38 the Berger-Sehgal (BS) COH [7] scattering model, an intranuclear cascade model for FSI [24],
39 and a coupling to PYTHIA [26] for hadronization.
- 40 (ii) NEUT [14]: Corresponds to the combination of the LFG model [8, 9], the Nieves CCQE scattering
41 prescription [23], the Nieves MEC model using a lookup table [25], the Berger Sehgal RES [6, 13, 5]
42 and BS COH [7] scattering models, FSI with medium corrections for pions [2, 3], and PYTHIA [26]
43 purposes.
- 44 (iii) GiBUU [21]: Uses similar models to GENIE, but they are implemented in a coherent way by solving
45 the Boltzmann-Uehling-Uhlenbeck transport equation [21]. The modeling includes the LFG model [9],
46 a standard CCQE expression [17], an empirical MEC model, and a dedicated spin dependent resonance
47 amplitude calculation following the MAID analysis [21]. The DIS model is from PYTHIA [26]. GiBUU's
48 FSI treatment propagates the hadrons through the residual nucleus in a nuclear potential consistent
49 with the initial state.

50 2.3 Variables definition

51 Given the momentum vectors for the leading proton \vec{p}_L , recoil proton \vec{p}_R , and muon \vec{p}_μ , we define several
52 variables. First, we define the momenta and opening angle of each variable, denoted as $|\vec{p}|$ and $\cos(\theta_{\vec{p}})$, with
53 the appropriate index for each momentum vector. These variables are plotted in Figure 1.

54 We also define variables relating the multiple momentum vectors. First, the opening angle between the
55 protons in the lab frame, given by

$$\cos(\theta_{\vec{p}_L, \vec{p}_R}) = \frac{\vec{p}_L \cdot \vec{p}_R}{|\vec{p}_L| |\vec{p}_R|}. \quad (2)$$

56 Then, the opening angle between the total proton momentum ($\vec{p}_{\text{sum}} = \vec{p}_L + \vec{p}_R$) and the muon, given by

$$\cos(\theta_{\vec{p}_\mu, \vec{p}_{\text{sum}}}) = \frac{\vec{p}_\mu \cdot \vec{p}_{\text{sum}}}{|\vec{p}_\mu| |\vec{p}_{\text{sum}}|}. \quad (3)$$

57 The momentum transverse to the direction of the neutrino beam, which we denote $\delta\vec{P}_T$ and is given by

$$\delta\vec{P}_T = \vec{p}_T^\mu + \vec{p}_T^L + \vec{p}_T^R. \quad (4)$$

58 For the transverse momentum, we will be interested in its magnitude $|\delta\vec{P}_T|$. Finally, the angular orientation
59 of the transverse momentum with respect to the transverse muon is defined as

$$\delta\alpha_T = \cos^{-1} \left(\frac{-\vec{p}_T^\mu \cdot \delta\vec{P}_T}{|\vec{p}_T^\mu| |\delta\vec{P}_T|} \right). \quad (5)$$

60 We plot the differential cross sections of these variables for the given generators in Figure 2. We can also
61 see the cross section by event type for all variables and all generators in Figures 3 to 12.

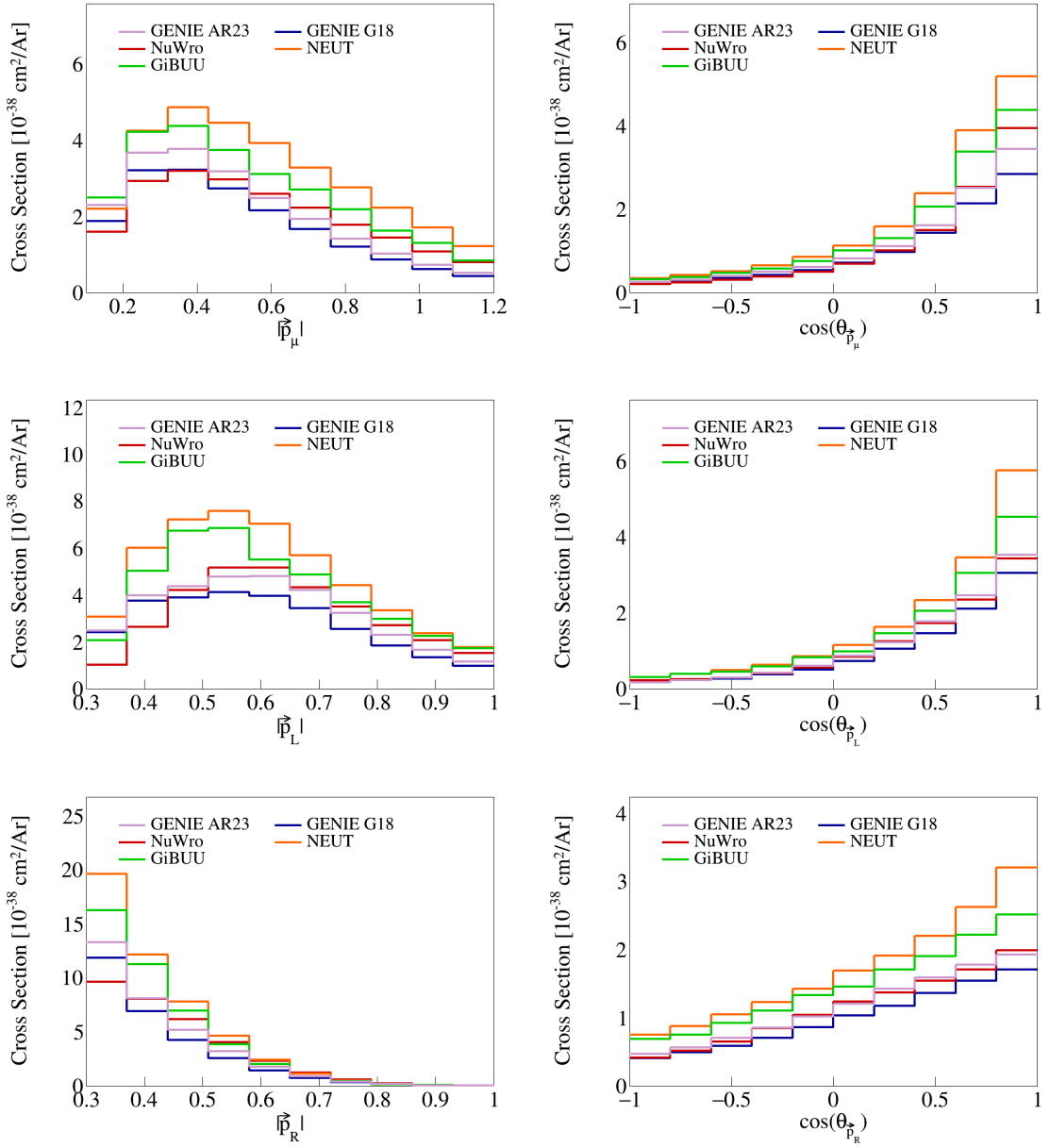


Figure 1: Cross sections for momentum and opening angles of individual particles.

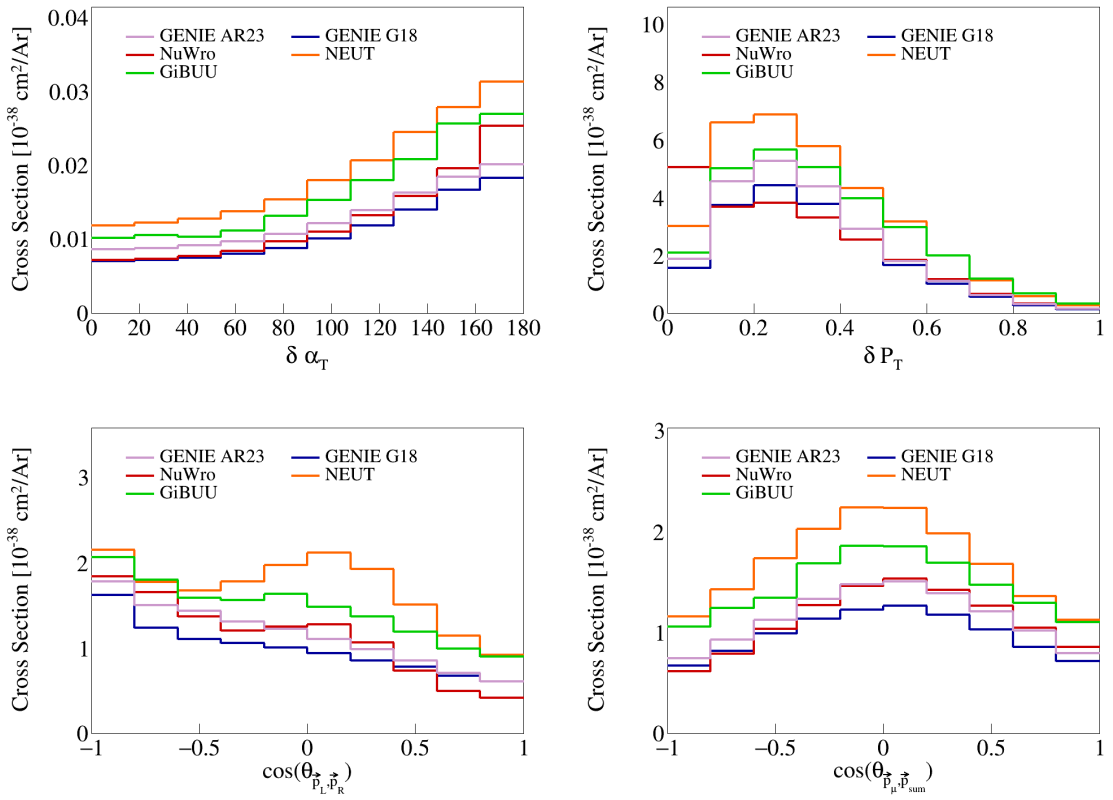


Figure 2: Cross sections for opening angles and transverse momentum.

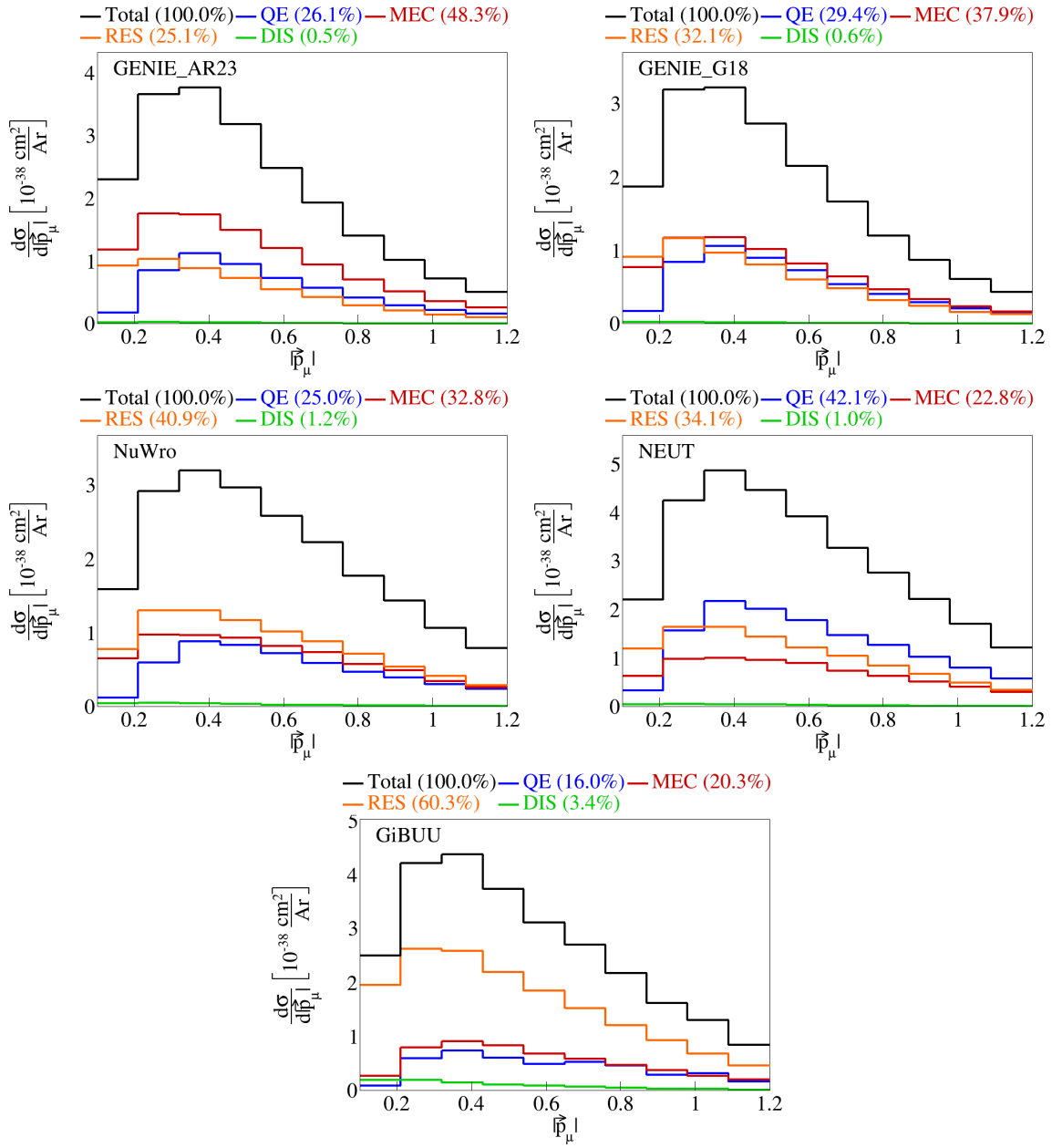


Figure 3: Event interaction breakdown for $|\vec{p}_\mu|$.

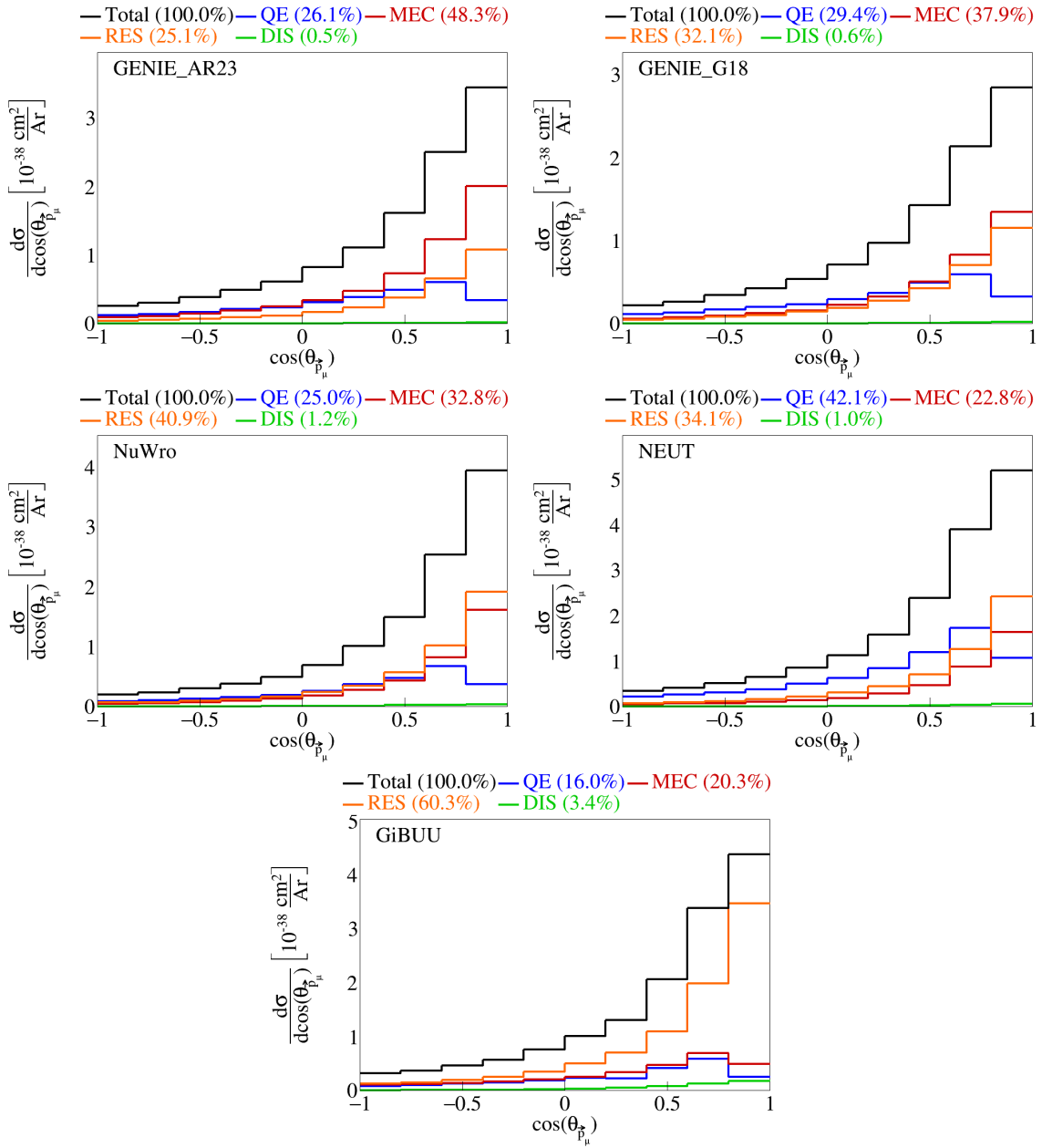


Figure 4: Event interaction breakdown for $\cos(\theta_{\vec{p}_\mu})$.

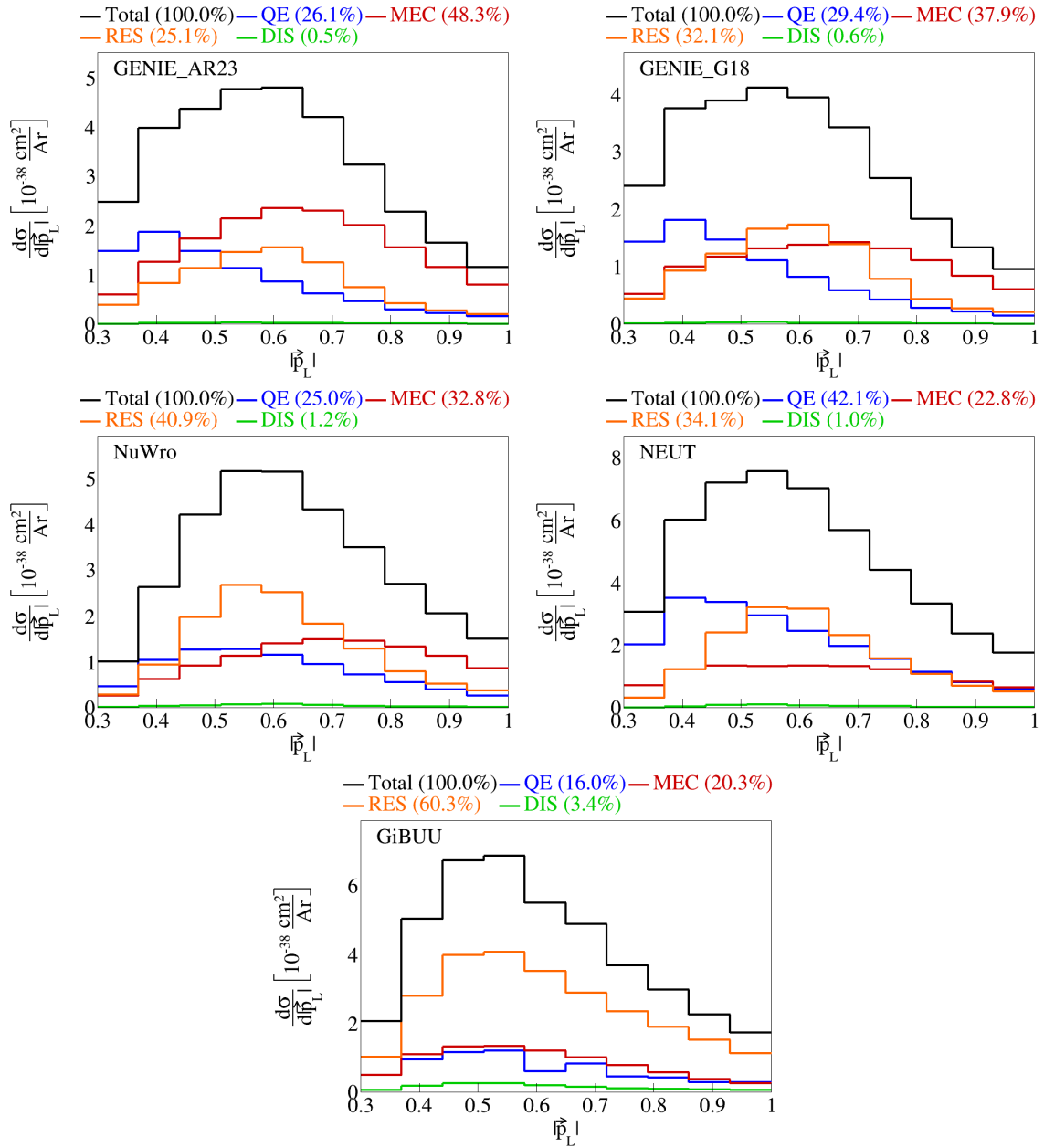


Figure 5: Event interaction breakdown for $|\vec{p}_L|$.

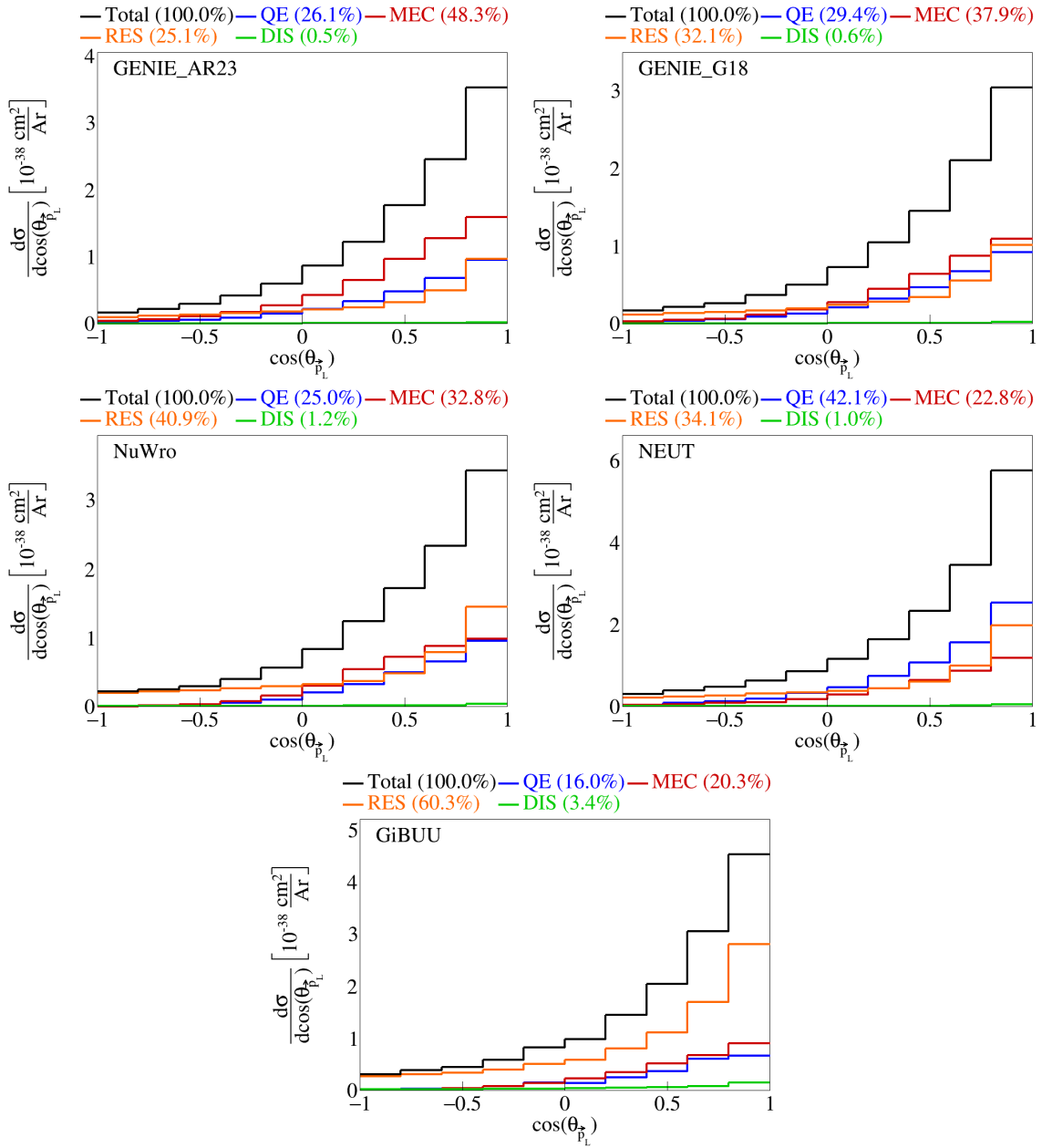


Figure 6: Event interaction breakdown for $\cos(\theta_{\vec{p}_L})$.

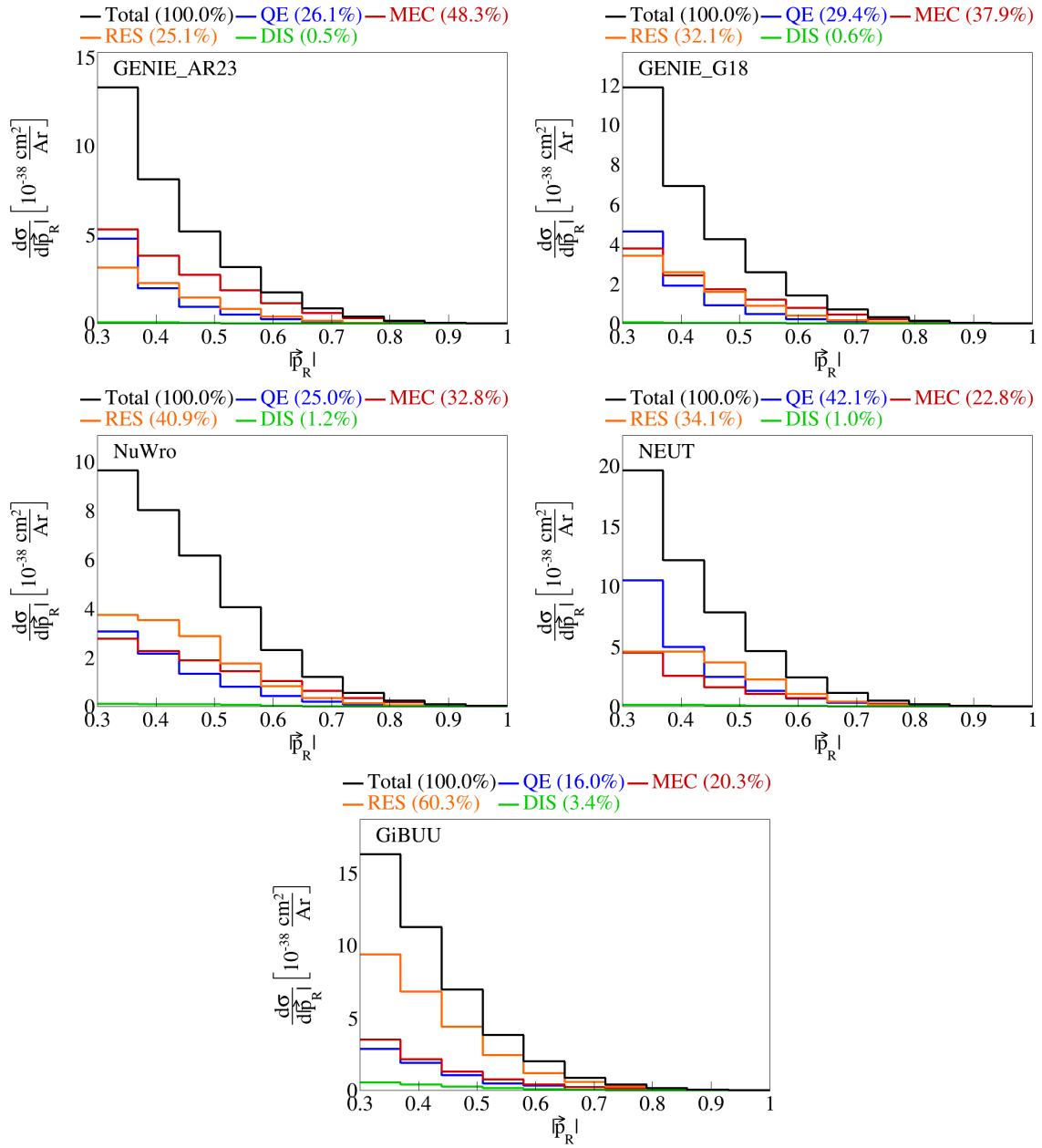


Figure 7: Event interaction breakdown for $|\vec{p}_R|$.

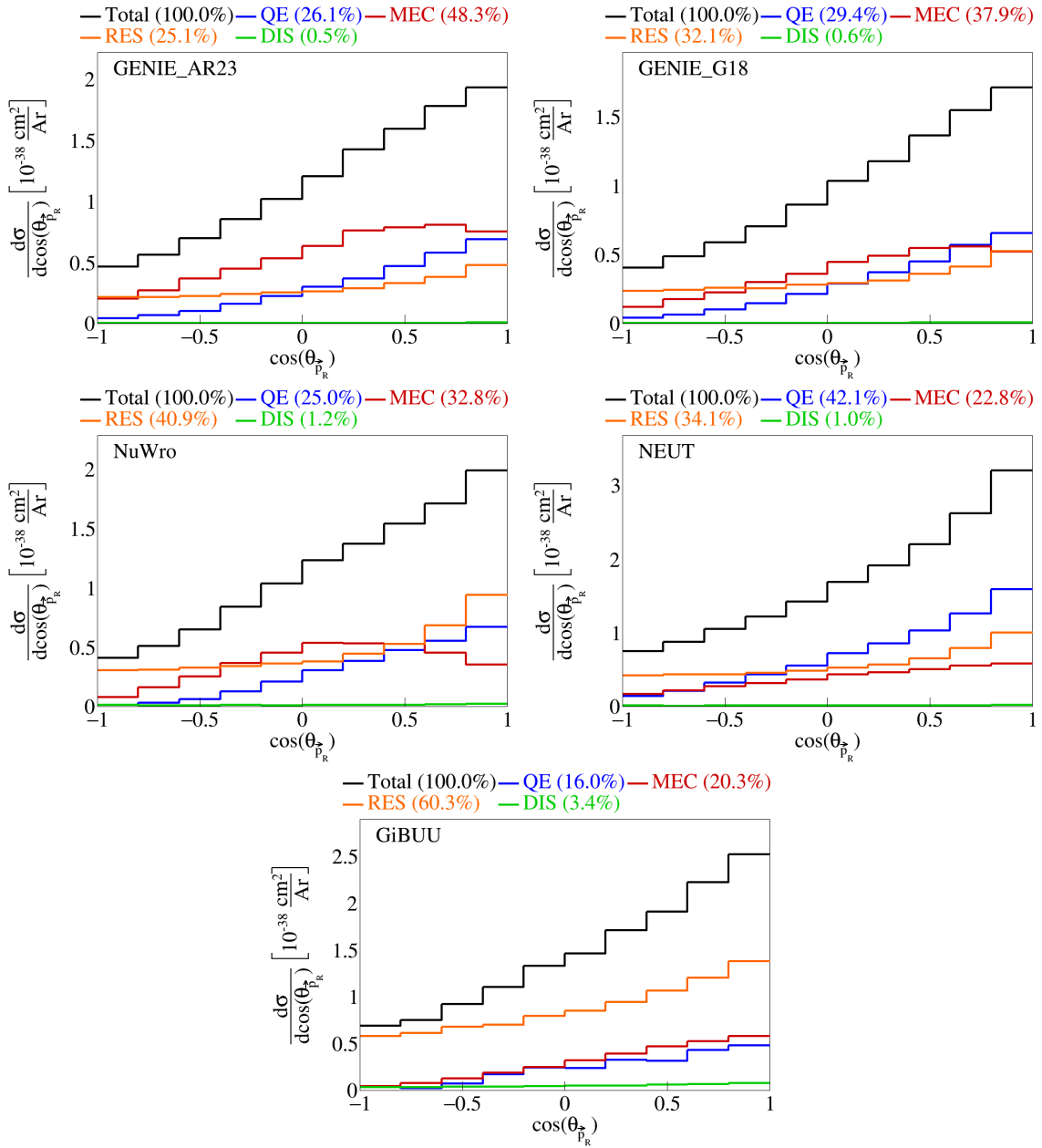


Figure 8: Event interaction breakdown for $\cos(\theta_{\vec{p}_R})$.

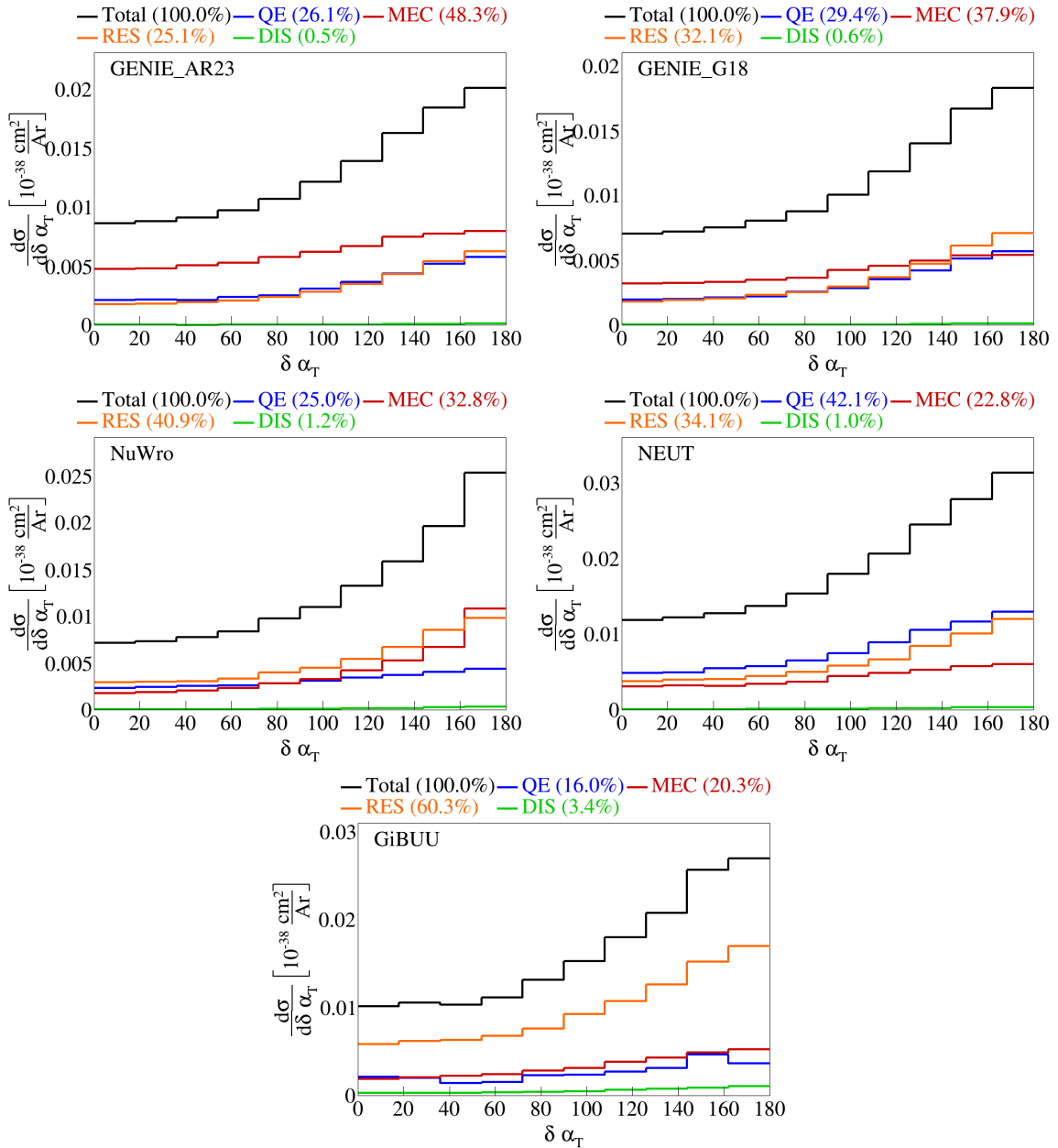


Figure 9: Event interaction breakdown for $\delta \alpha_T$.

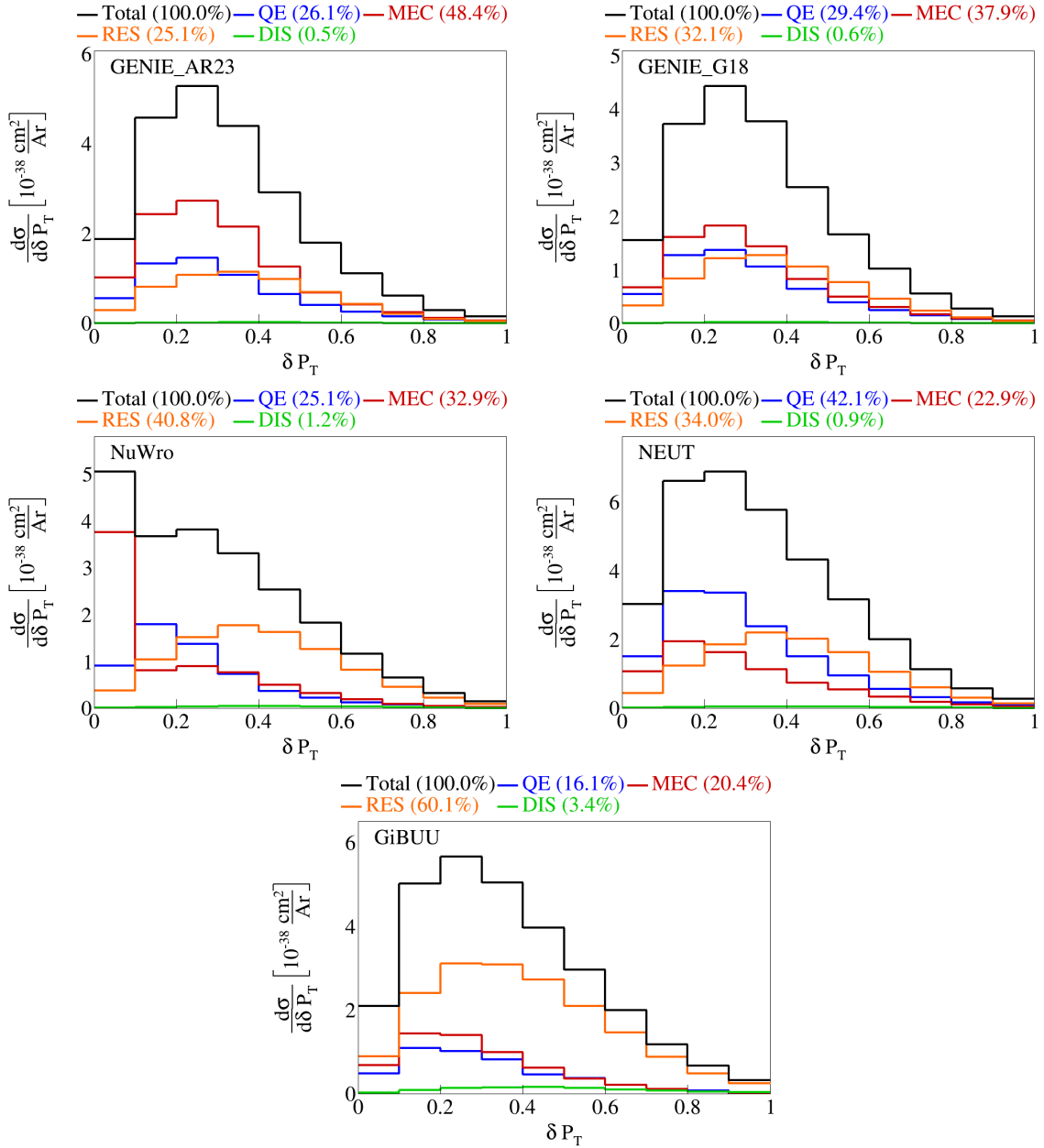


Figure 10: Event interaction breakdown for $|\delta \vec{P}_T|$.

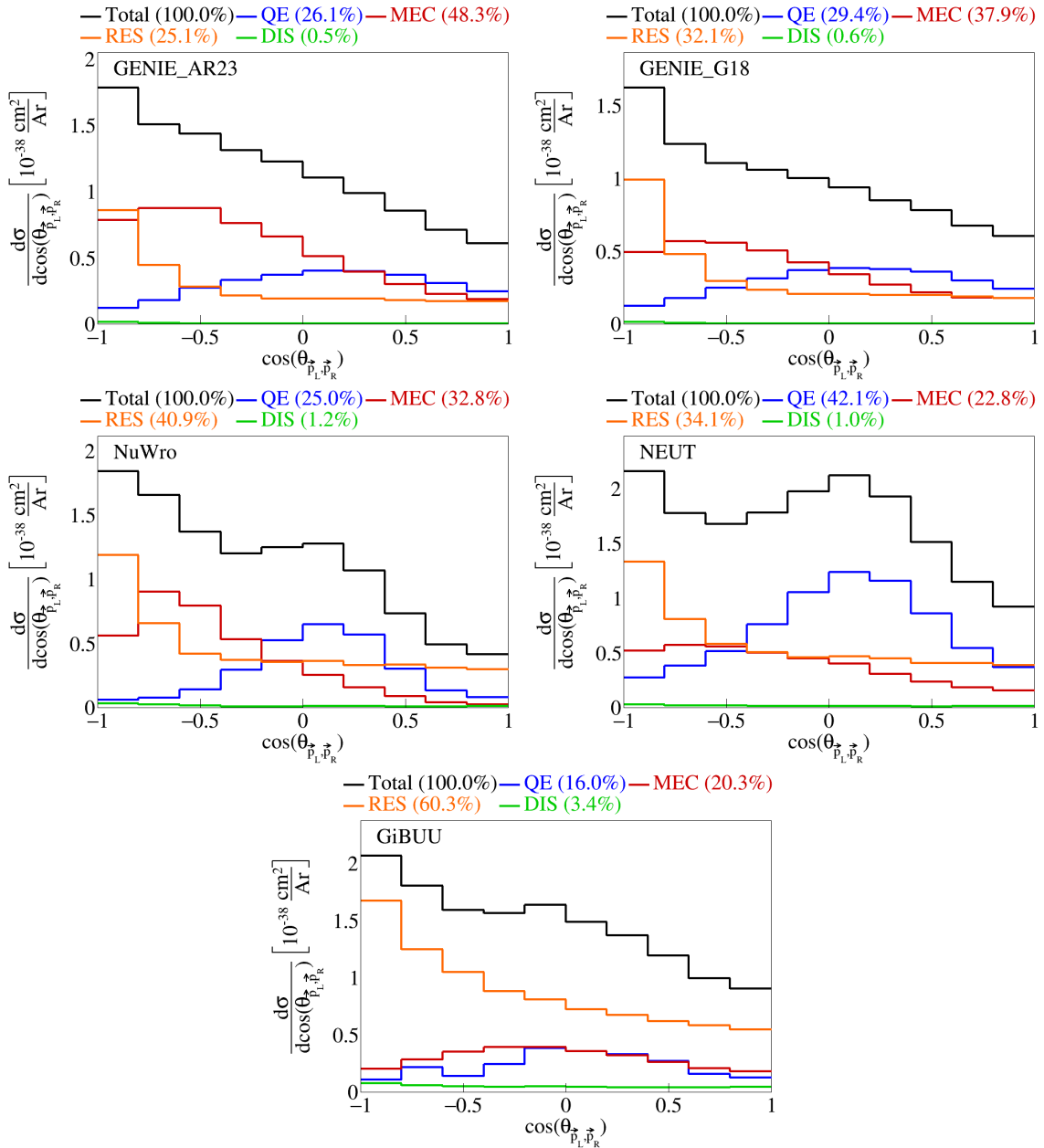


Figure 11: Event interaction breakdown for $\cos(\theta_{\vec{p}_L, \vec{p}_R})$.

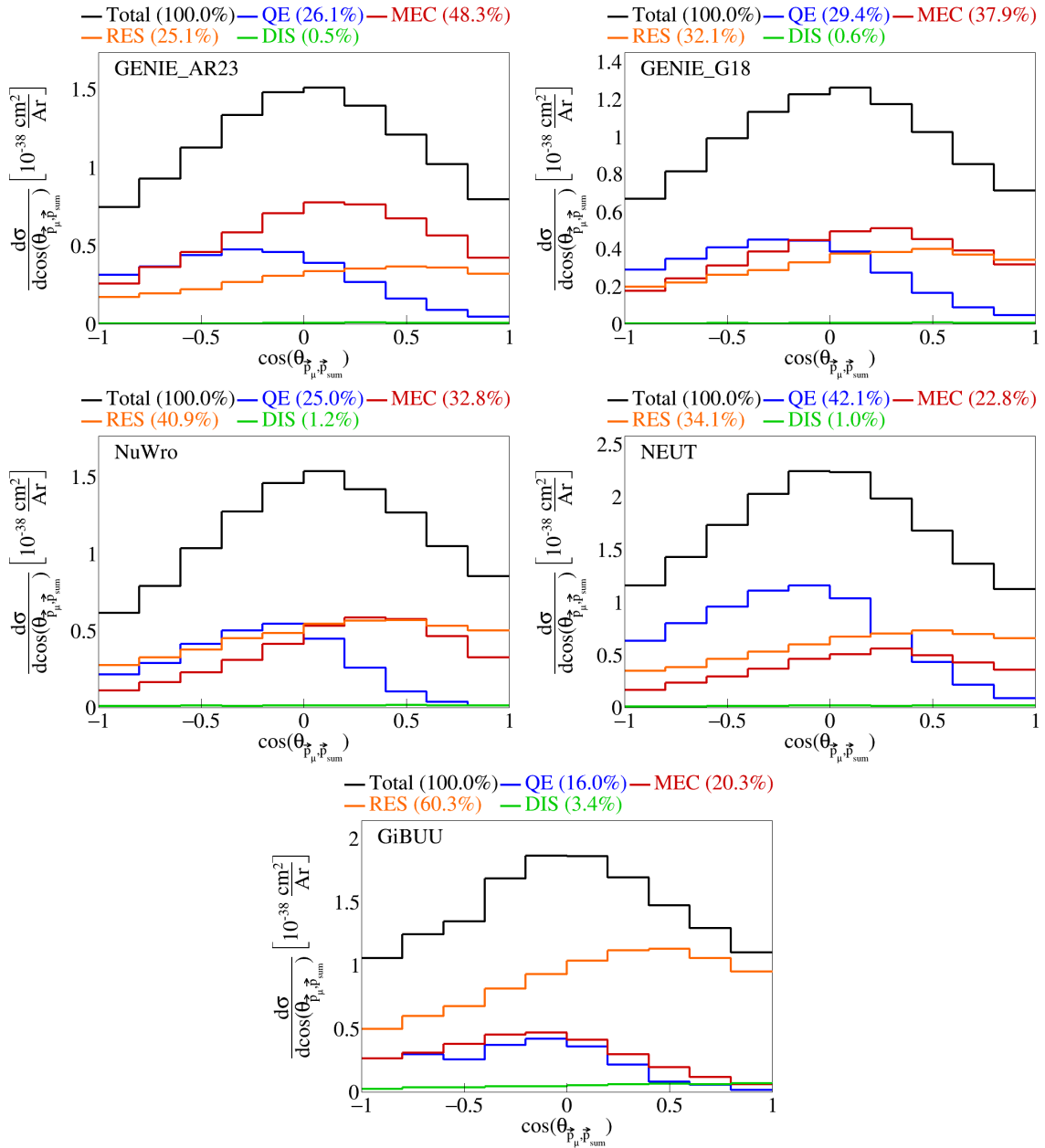


Figure 12: Event interaction breakdown for $\cos(\theta_{\vec{p}_\mu, \vec{p}_{\text{sum}}})$.

62 **2.4 Pre-FSI events**

63 To investigate why the percentage of MEC events for some generators is low, we performed event selection
64 before any final state interactions took place and plotted the interaction breakdown. For both GENIE tunes,
65 NEUT, and NuWro, we got 100% MEC events pre-FSI. For GiBUU, only 4.1% MEC versus 76.2% RES and
66 16% DIS events pre-FSI. The interaction breakdown for $|\vec{p}_\mu|$ for all the generators are shown in Figure 13.
67 Since GiBUU is the outlier, we checked the specific interaction mode for the resonance events. We got that
68 10 has 39.3%, 11 has 34.7%, 12 has 0.0136%, 13 has 26 %, and 27, 22, and 23 all have zero percent of the
69 resonance events. We also checked the event interaction breakdown for GiBUU samples generated without
70 final state interactions, in which we found that 100% of the events are MEC, shown in Figure 14.

71 Note that the difference between these two GiBUU samples is that in the former, the samples were
72 generated with final state interactions, and then we look at the state before the final state interactions
73 reportedly took place, and in the latter the event generation was done without any final state interactions.

74 **2.5 Double differential plots**

75 For our double differential variables, we look at δP_T , $\delta \alpha_T$, $\cos(\theta_{\vec{p}_L, \vec{p}_R})$, and $\cos(\theta_{\vec{p}_\mu, \vec{p}_{\text{sum}}})$ in $\cos(\theta_{\vec{p}_\mu})$. We
76 have two bins for $\cos(\theta_{\vec{p}_\mu})$, the first one going from -1 to 0.5 and the second from 0.5 to 1. Therefore, these
77 are irregular bins, with the first holding a larger range than the second. These plots are shown in Figure 15.
78 Note that, in these plots, the horizontal axis is defined by bin number of the double differential measurement,
79 not the value of the variable. This is because we are representing two variables in a single axis, but we can
80 slice the plots to get our usual horizontal axis.

81 We slice the double differential plots into two plots each, so that we have the variable of interest in the
82 horizontal axis instead of bin numbers, and each slice corresponds to one bin of $\cos(\theta_{\vec{p}_\mu})$. These plots are
83 shown in Figure 16, and the plots broke down by interaction are in Figures 17 to 20. In these plots, the
84 bins contents have been reweighted appropriately, by dividing the content of each bin by the width of the
85 bin for the variable in the axis multiplied by the width of the $\cos(\theta_{\vec{p}_\mu})$ slice. Note that the plots for the
86 $0.5 < \cos(\theta_{\vec{p}_\mu}) < 1$ slice have more events in general, although they span a smaller phase space of $\cos(\theta_{\vec{p}_\mu})$,
87 as it can be seen by the scale of the vertical axis. We performed the same double differential analysis for
88 the events before final state interactions. These are shown in Figure 21, and the corresponding interaction
89 breakdown plots are in Figures 22 to 25.

90 **2.6 Pure MEC events**

91 We also generated pure meson exchange current events using different configurations to get the MEC splines.
92 These were all generated using different tunes of GENIE: AR23, G18 with Empirical MEC model, and G18
93 with Nieves MEC model. The plots for the transverse kinematic variables are shown in Figure 26. The sliced
94 double differential plots are shown in Figure 27.

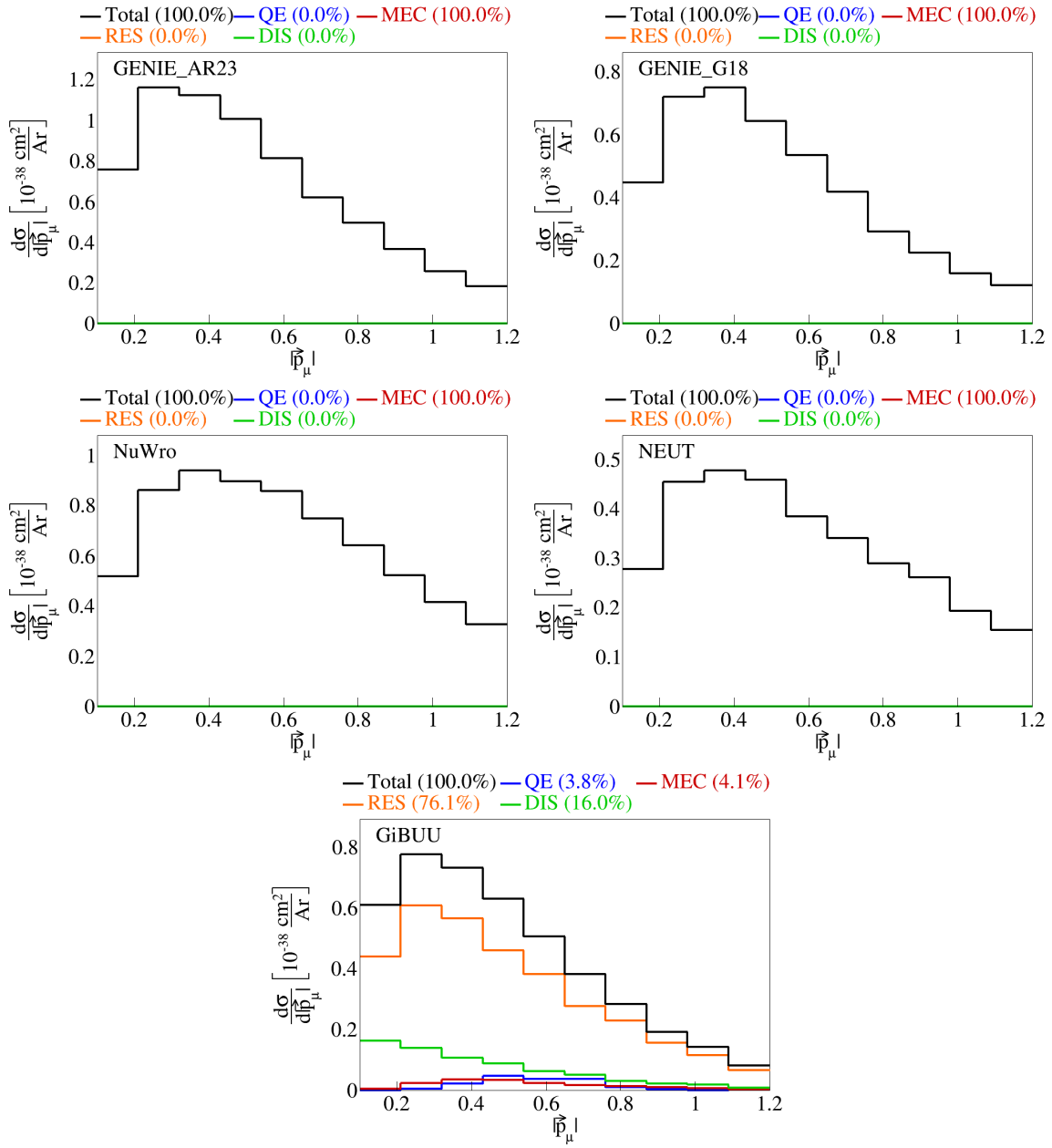


Figure 13: Event interaction breakdown of $|\vec{p}_\mu|$ before final state interactions.

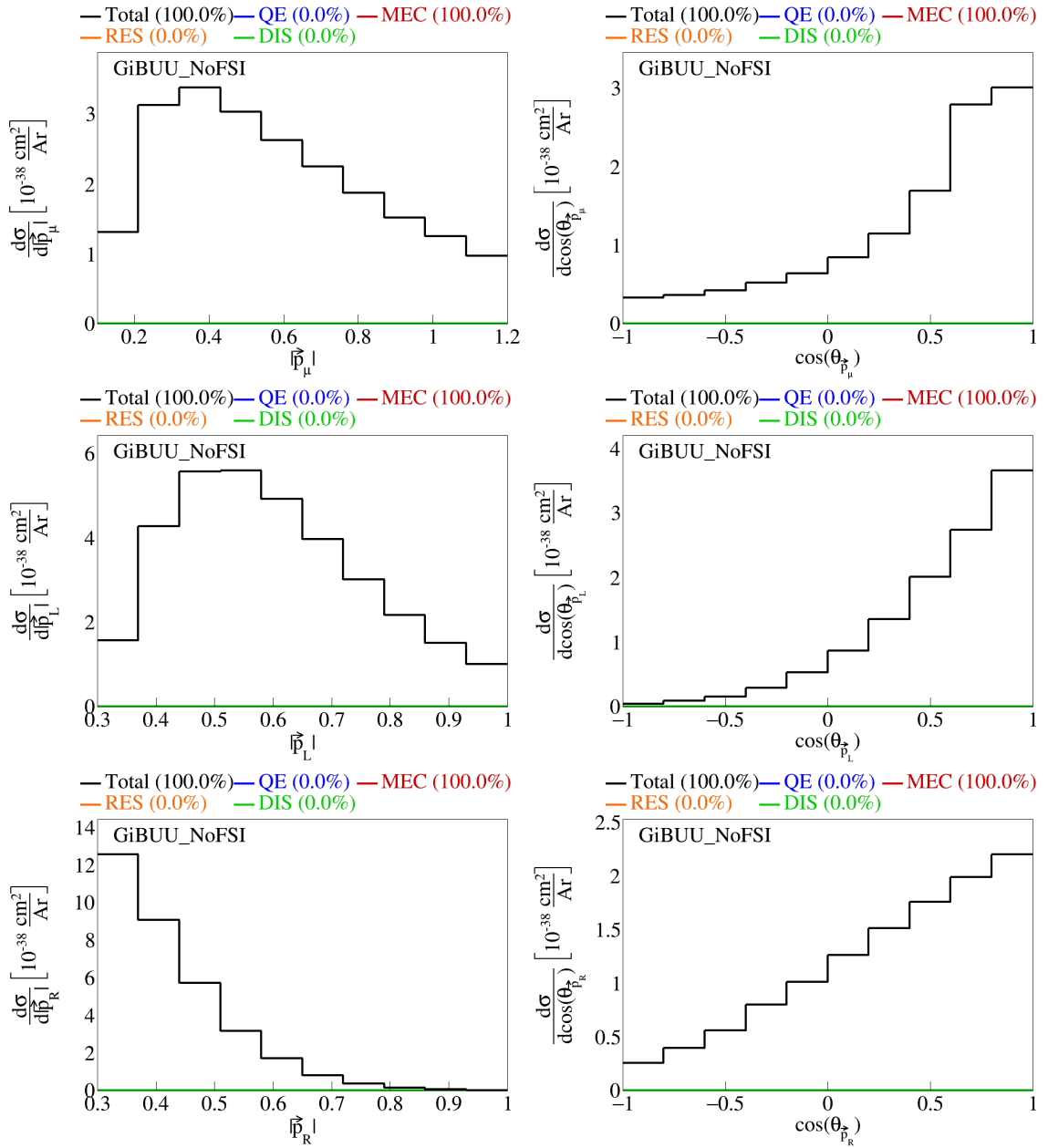


Figure 14: Event interaction breakdown for final events from GiBUU events with no FSI.

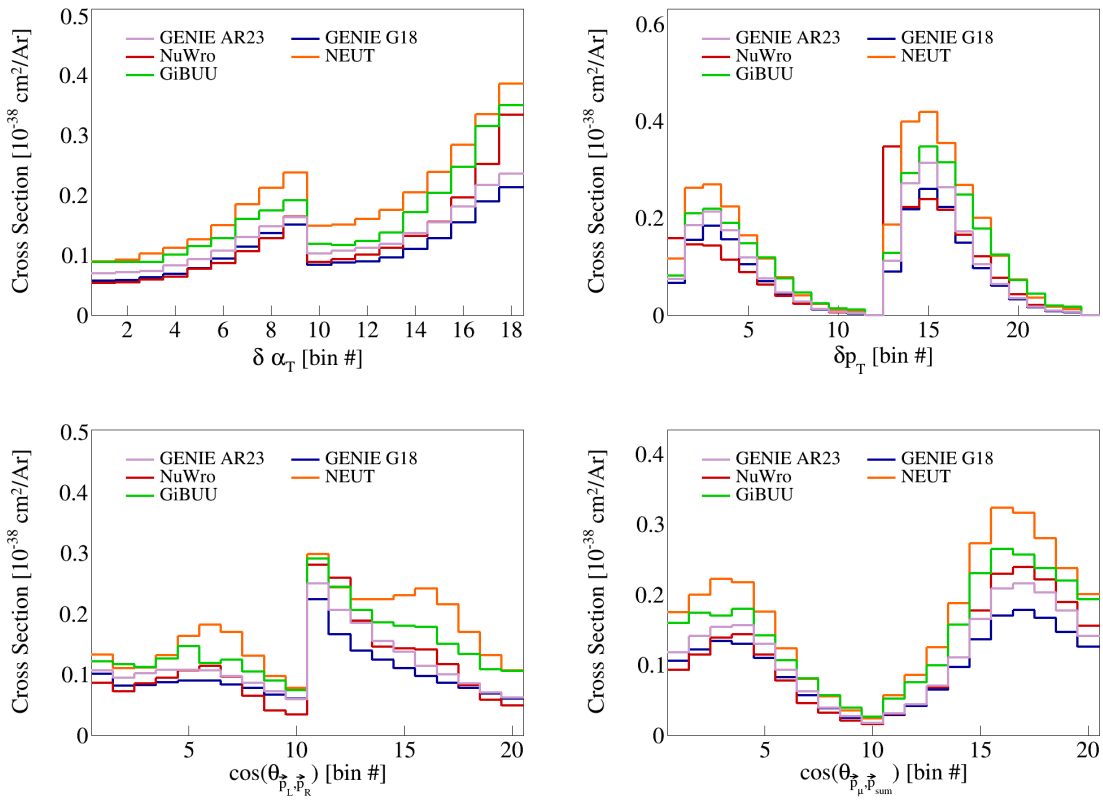


Figure 15: Double differential serial plots, all in $\cos(\theta_{\vec{p}_\mu})$.

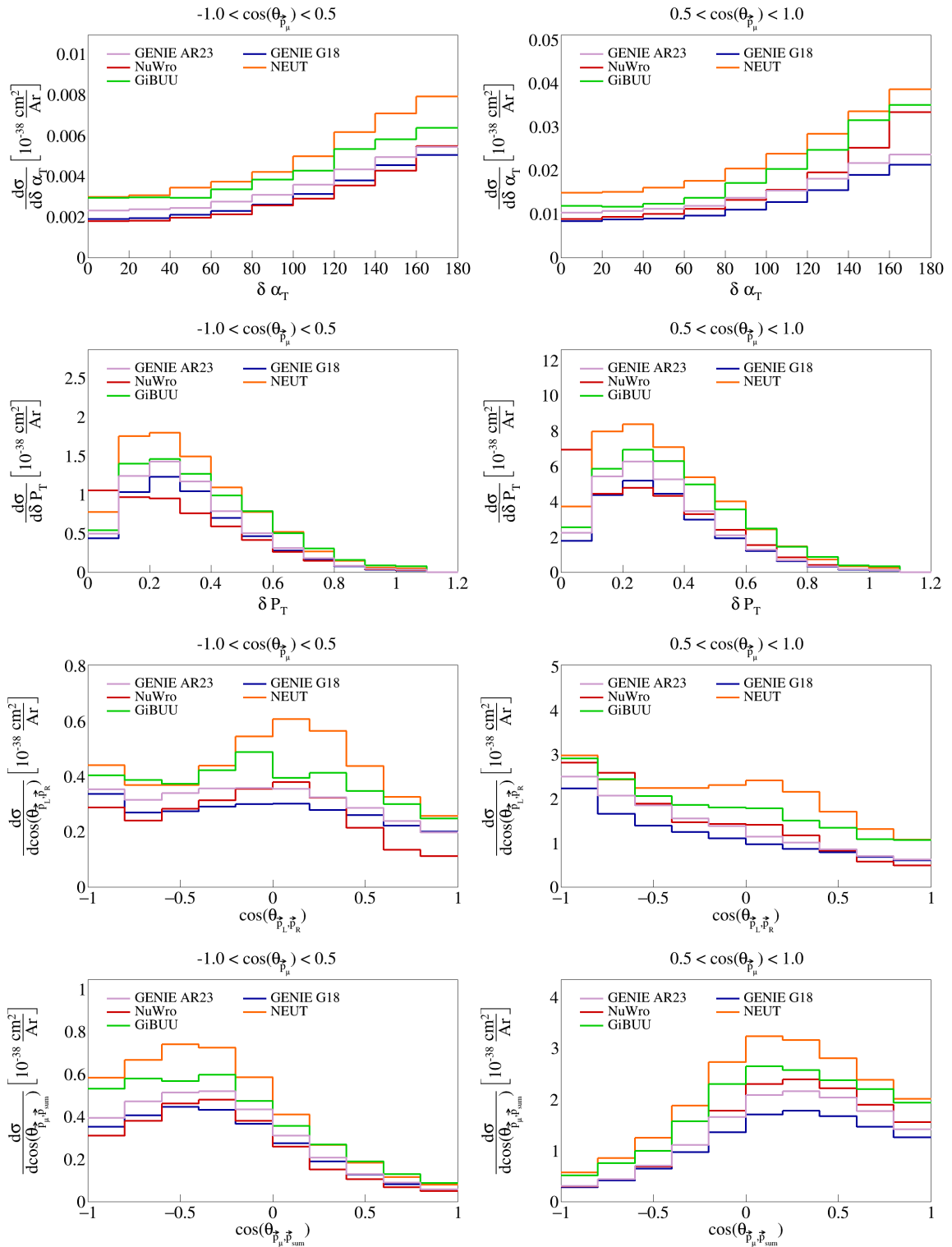


Figure 16: Sliced double differential plots.

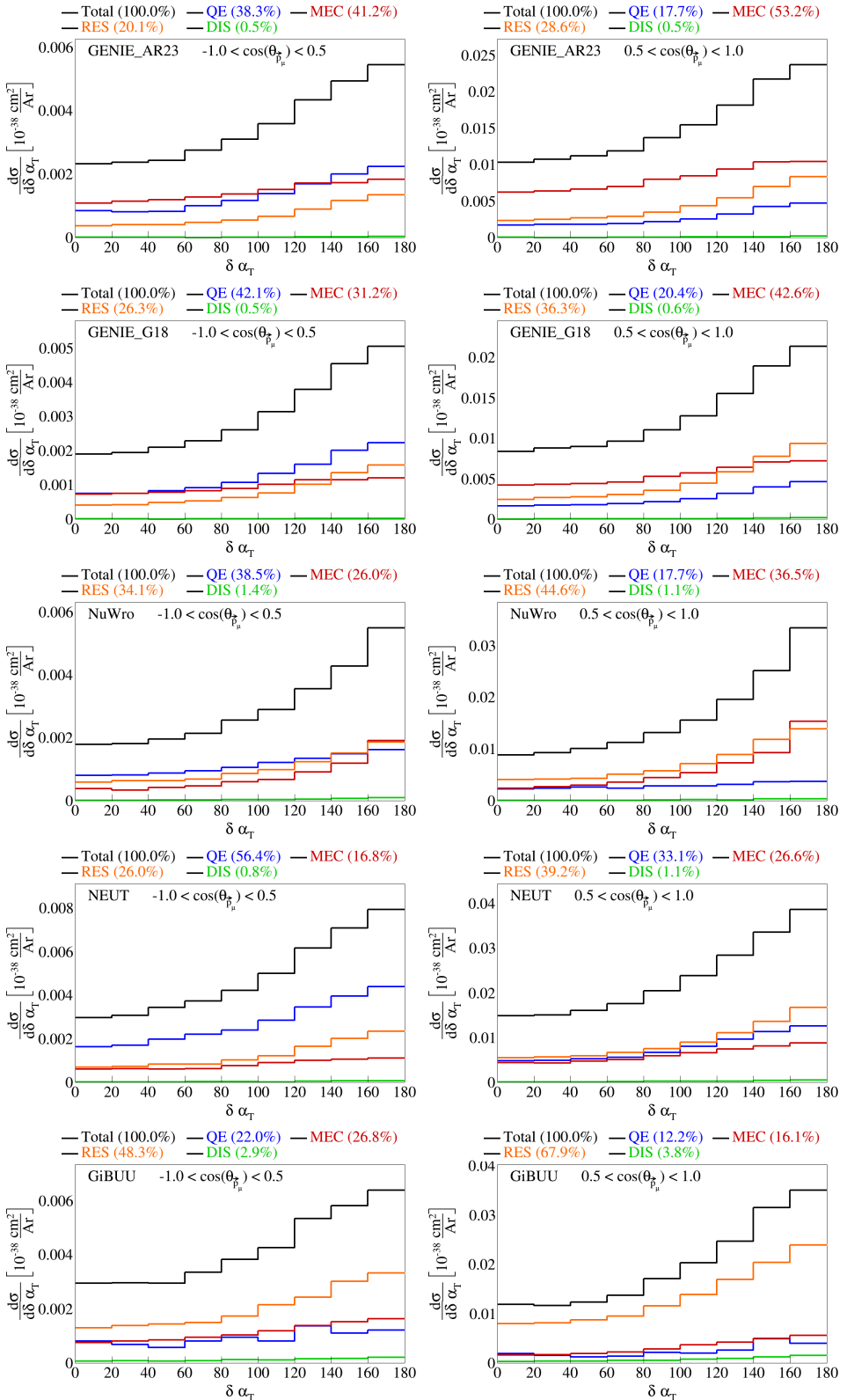


Figure 17: Interaction breakdown for sliced double differential plots for $\delta\alpha_T$ in $\cos(\theta_{\vec{p}_\mu})$.

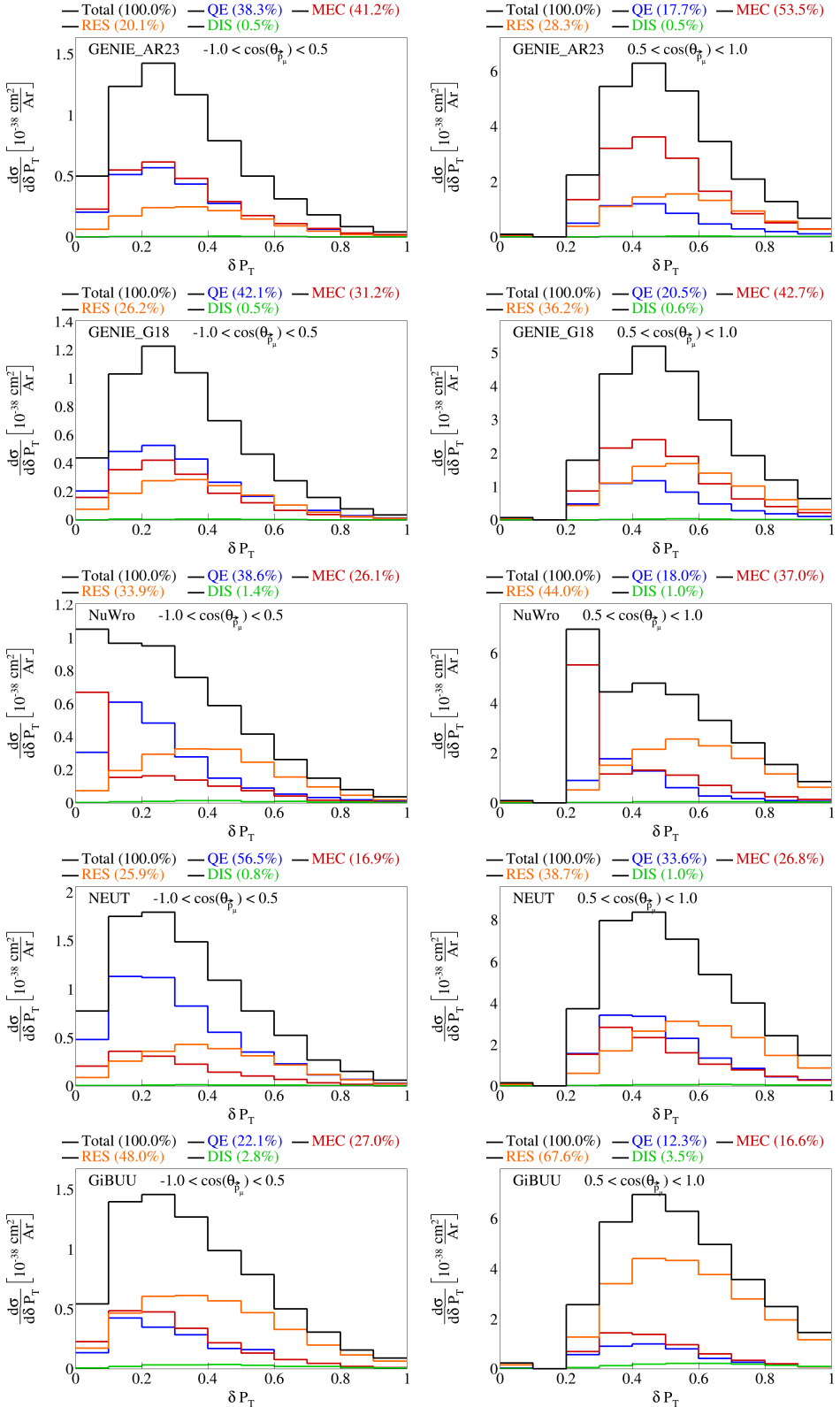


Figure 18: Interaction breakdown for sliced double differential plots for $|\delta \vec{P}_T|$ in $\cos(\theta_{\vec{p}_\mu})$.

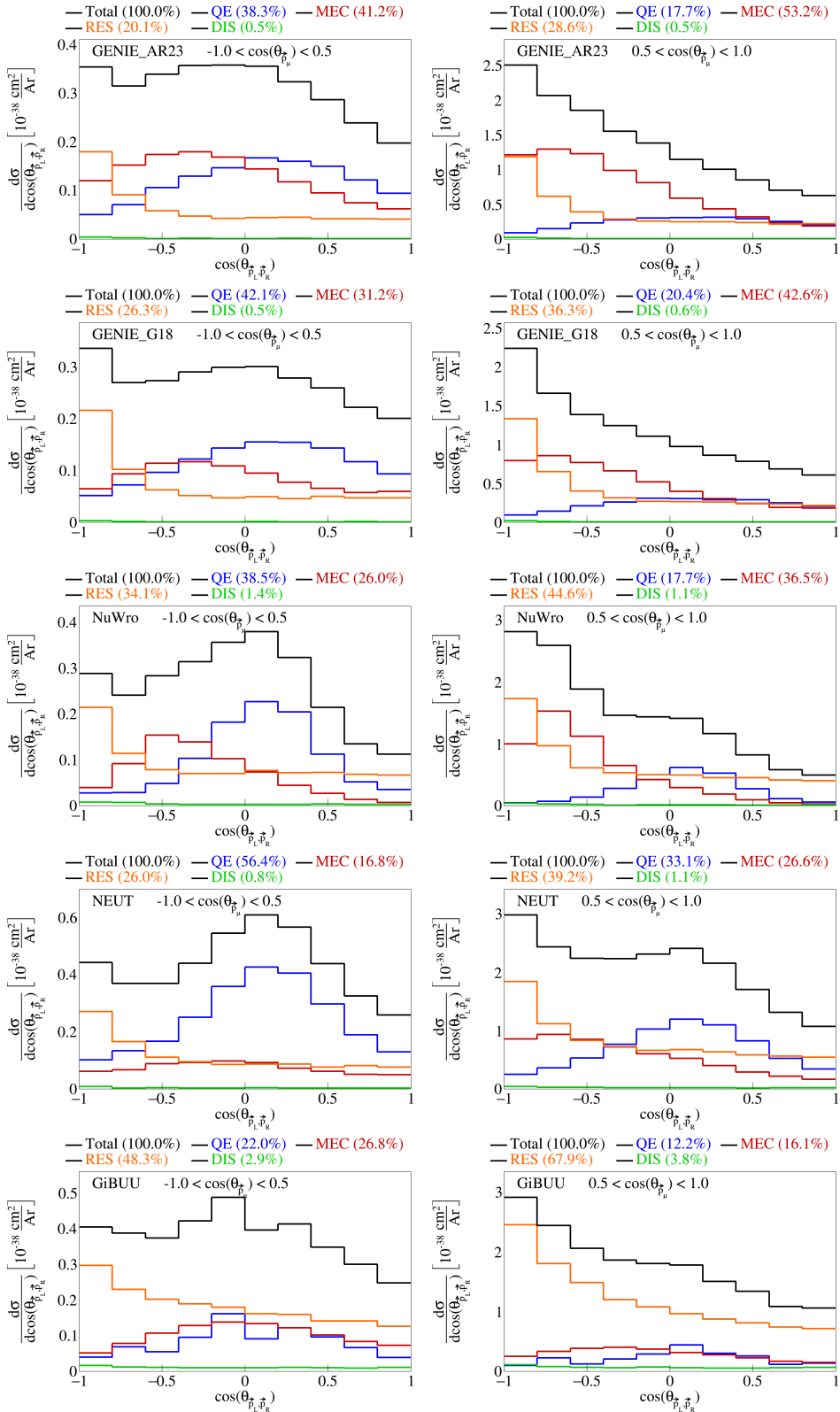


Figure 19: Interaction breakdown for sliced double differential plots for $\cos(\theta_{\vec{p}_L, \vec{p}_R})$ in $\cos(\theta_{\vec{p}_\mu})$.

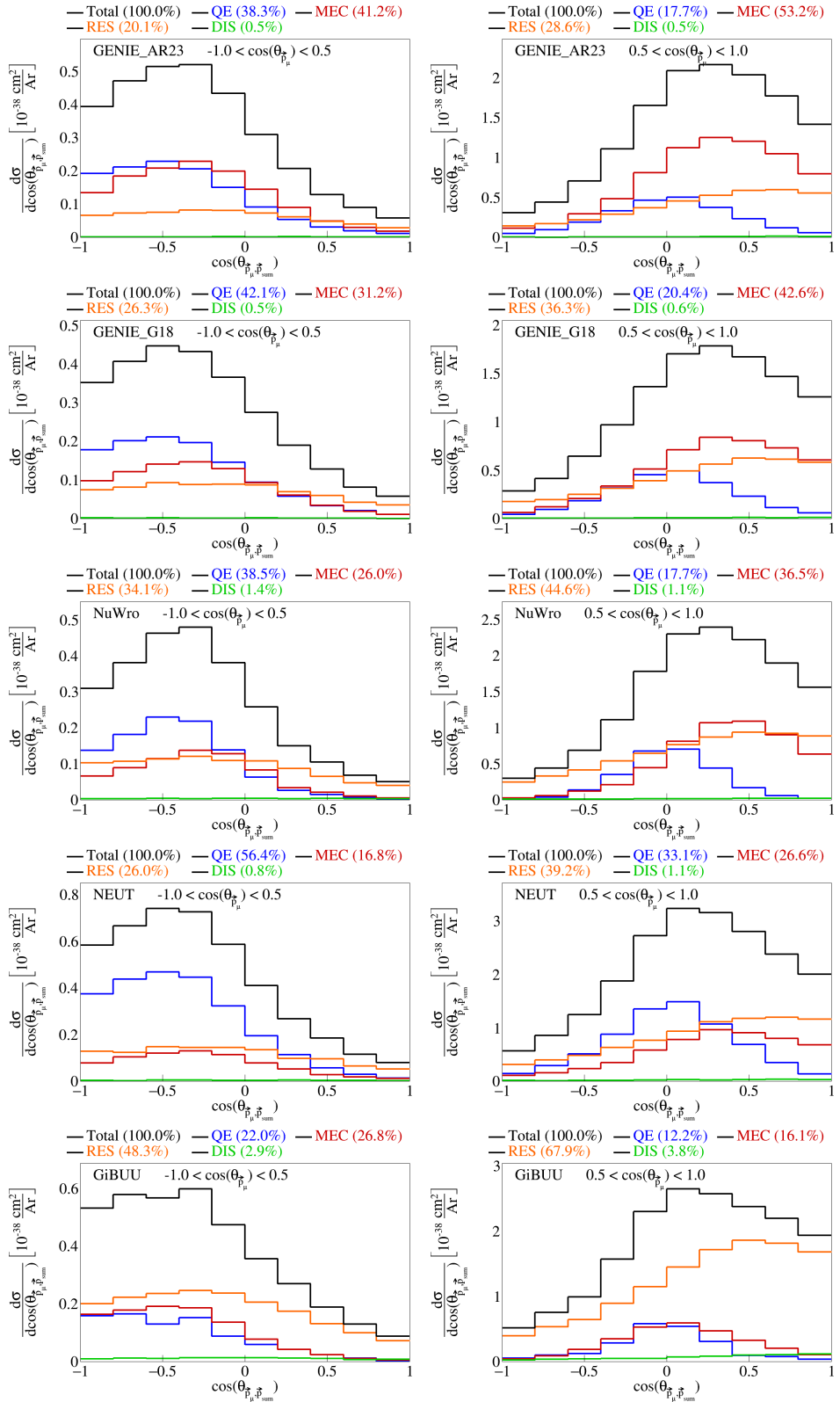


Figure 20: Interaction breakdown for sliced double differential plots for $cos(\theta_{\vec{p}_\mu}, \vec{p}_{sum})$ in $cos(\theta_{\vec{p}_\mu})$.

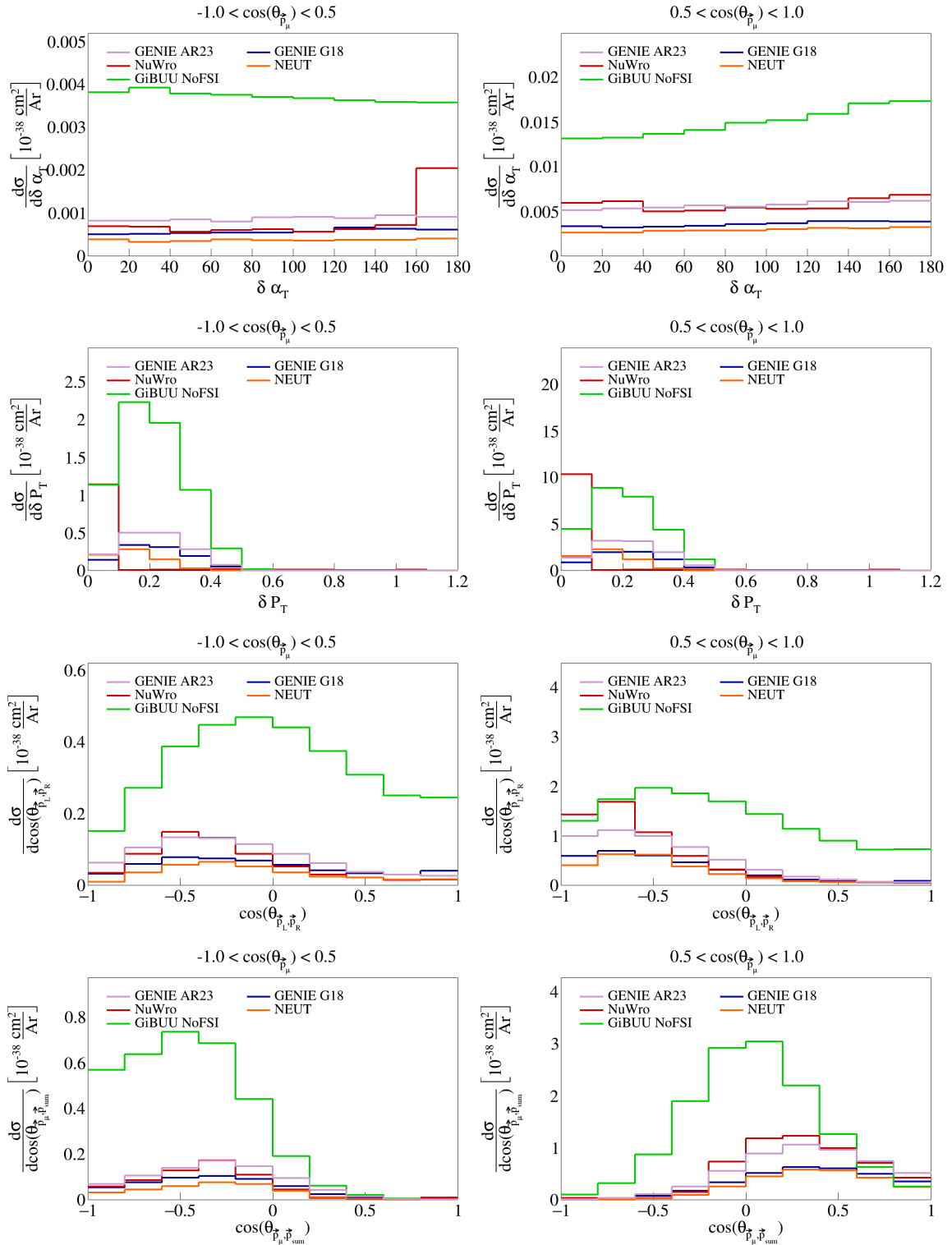


Figure 21: Sliced double differential plots for pre-FSI events.

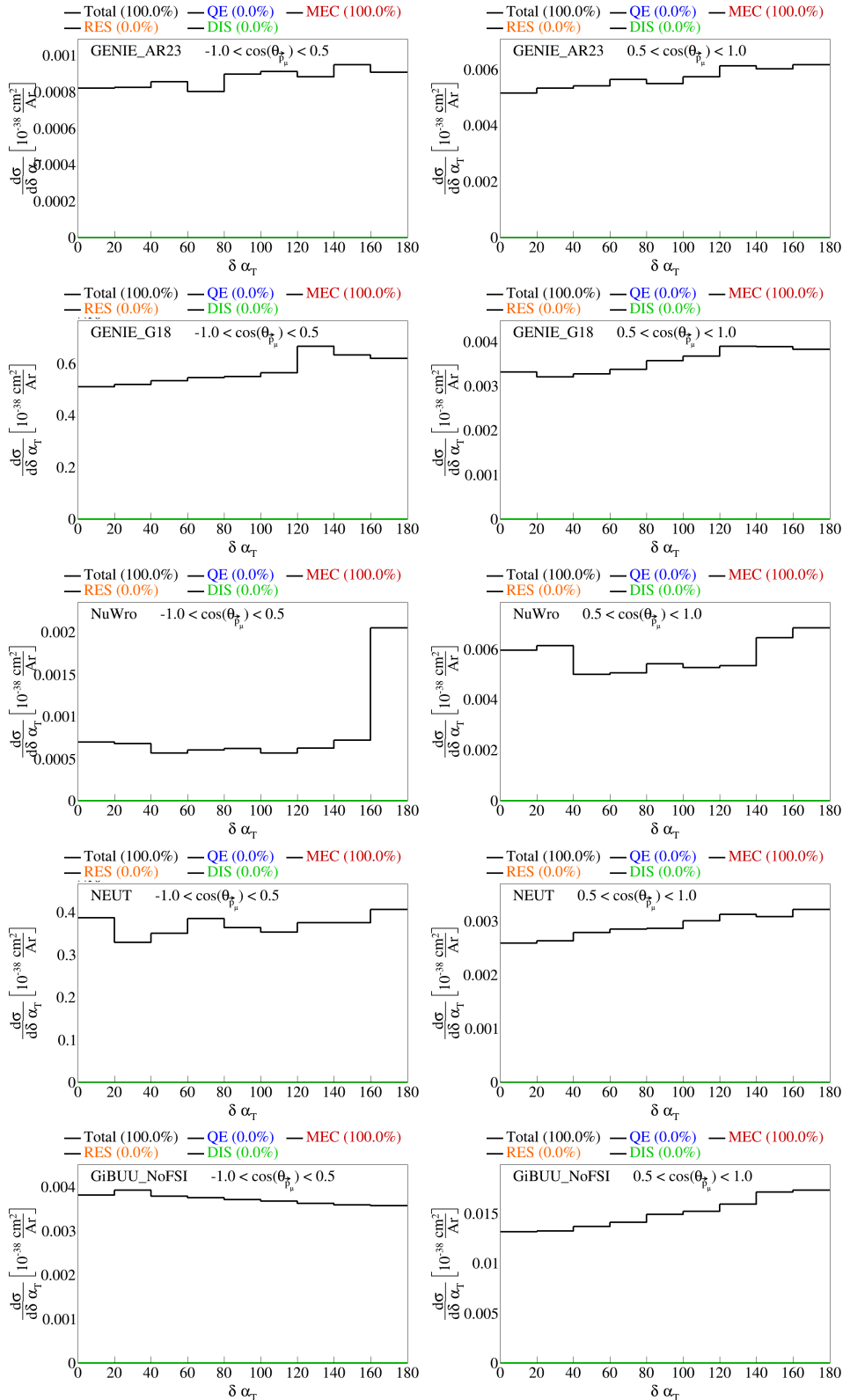


Figure 22: Interaction breakdown for sliced double differential plots for pre-FSI $\delta\alpha_T$ in $\cos(\theta_{\bar{p}_\mu})$.

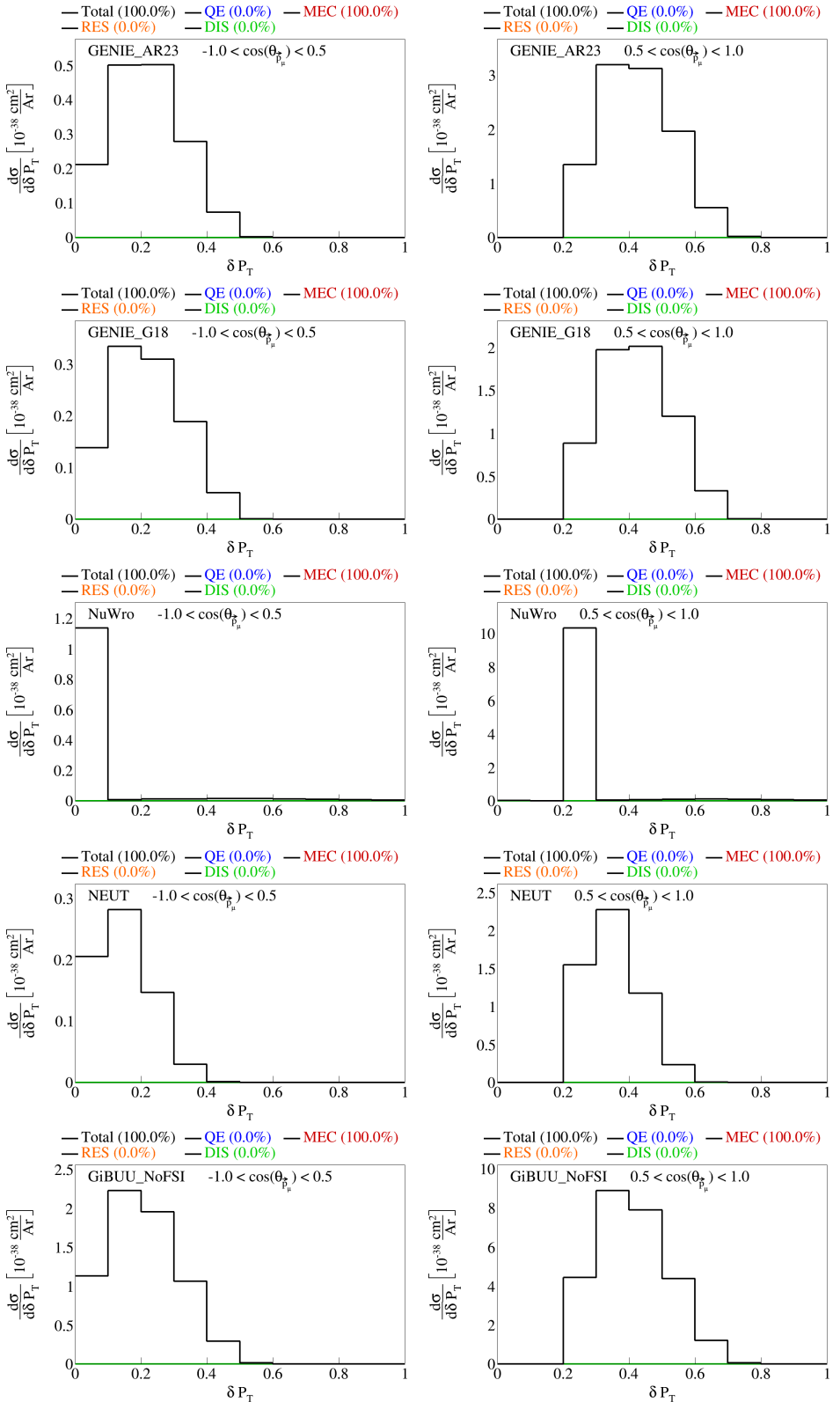


Figure 23: Interaction breakdown for sliced double differential plots for pre-FSI $|\delta \vec{P}_T|$ in $\cos(\theta_{\vec{P}_\mu})$.

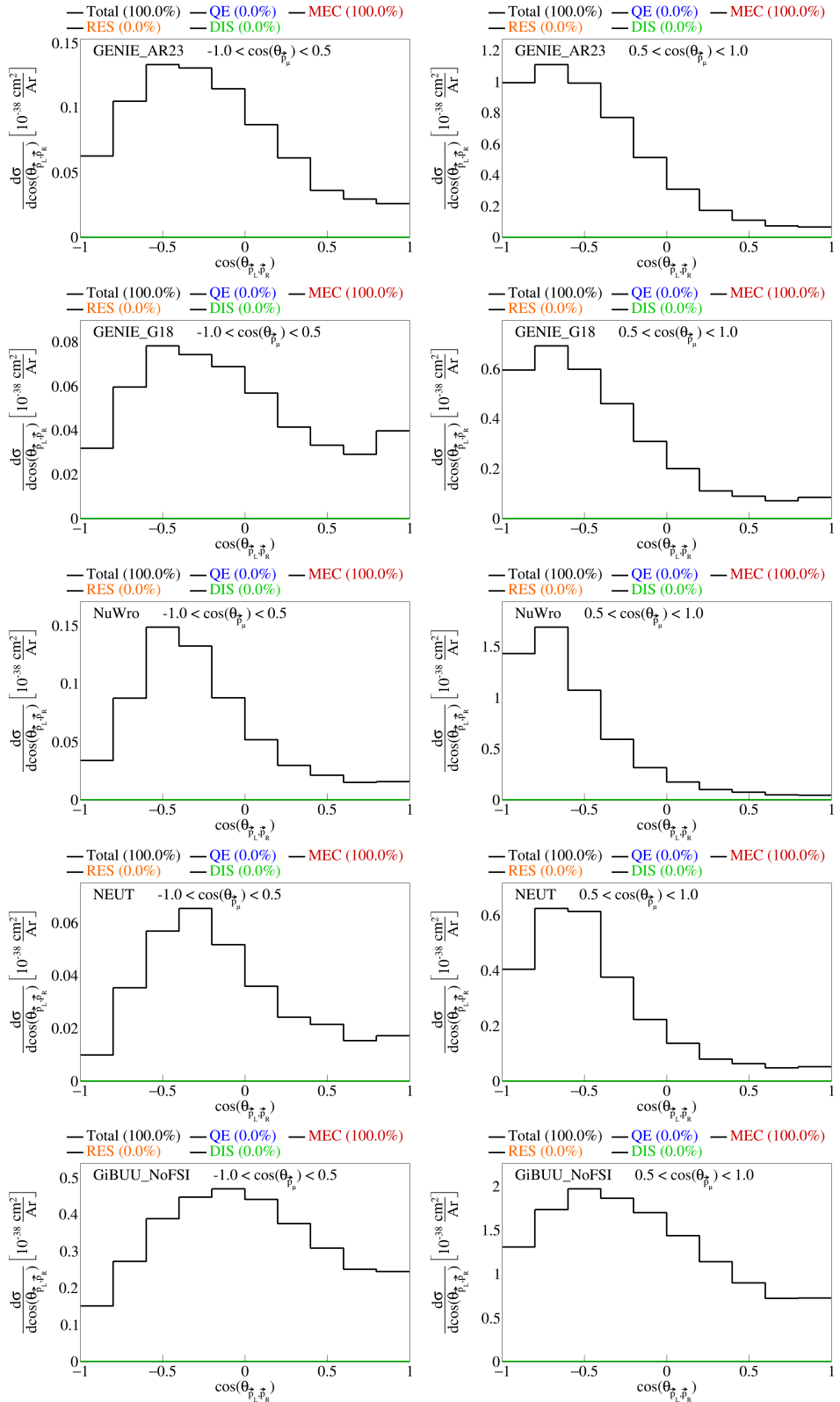


Figure 24: Interaction breakdown for sliced double differential plots for pre-FSI $\cos(\theta_{\vec{p}_L, \vec{p}_R})$ in $\cos(\theta_{\vec{p}_\mu})$.

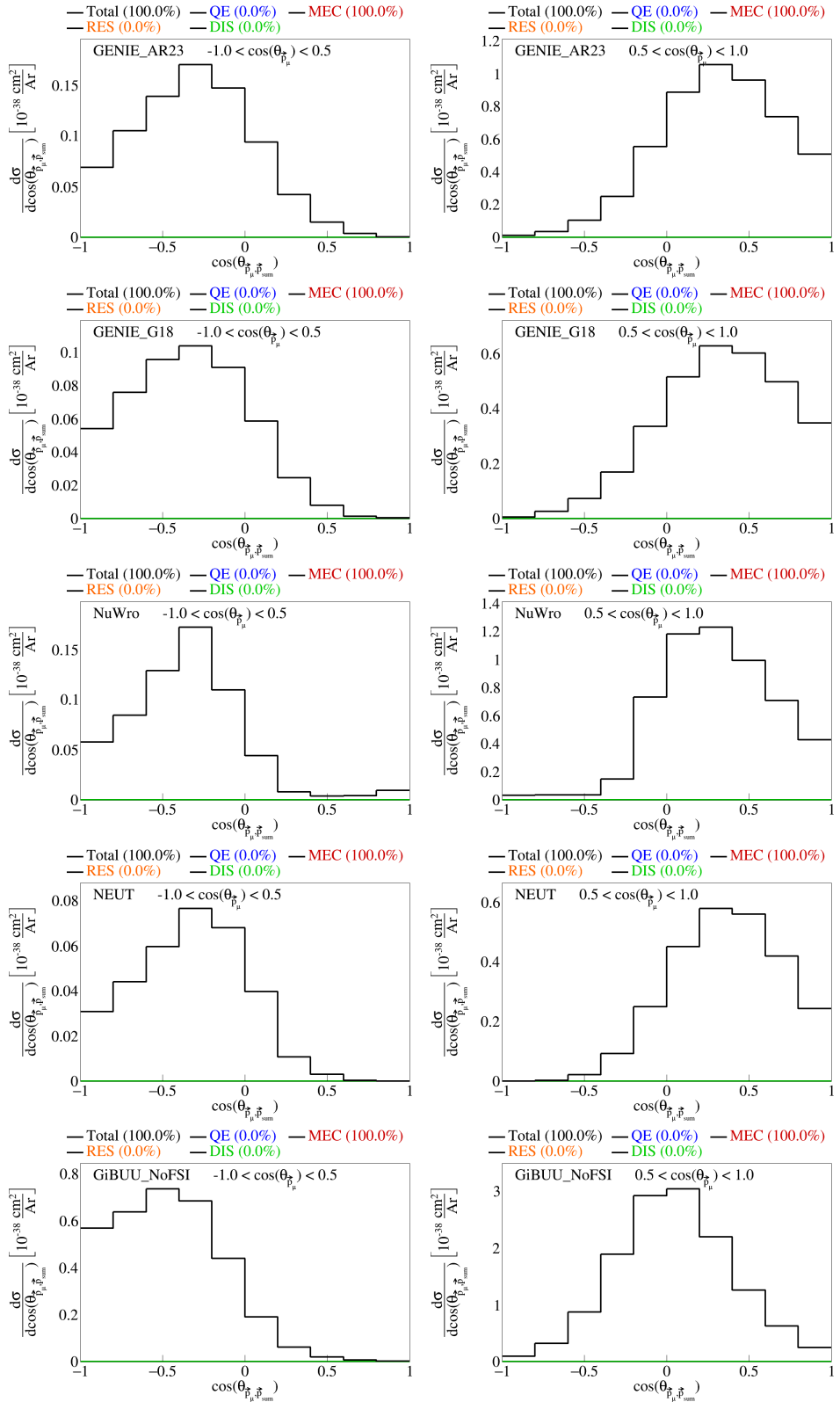


Figure 25: Interaction breakdown for sliced double differential plots for pre-FSI $\cos(\theta_{\vec{p}_\mu, \vec{p}_{\text{sum}}})$ in $\cos(\theta_{\vec{p}_\mu})$.

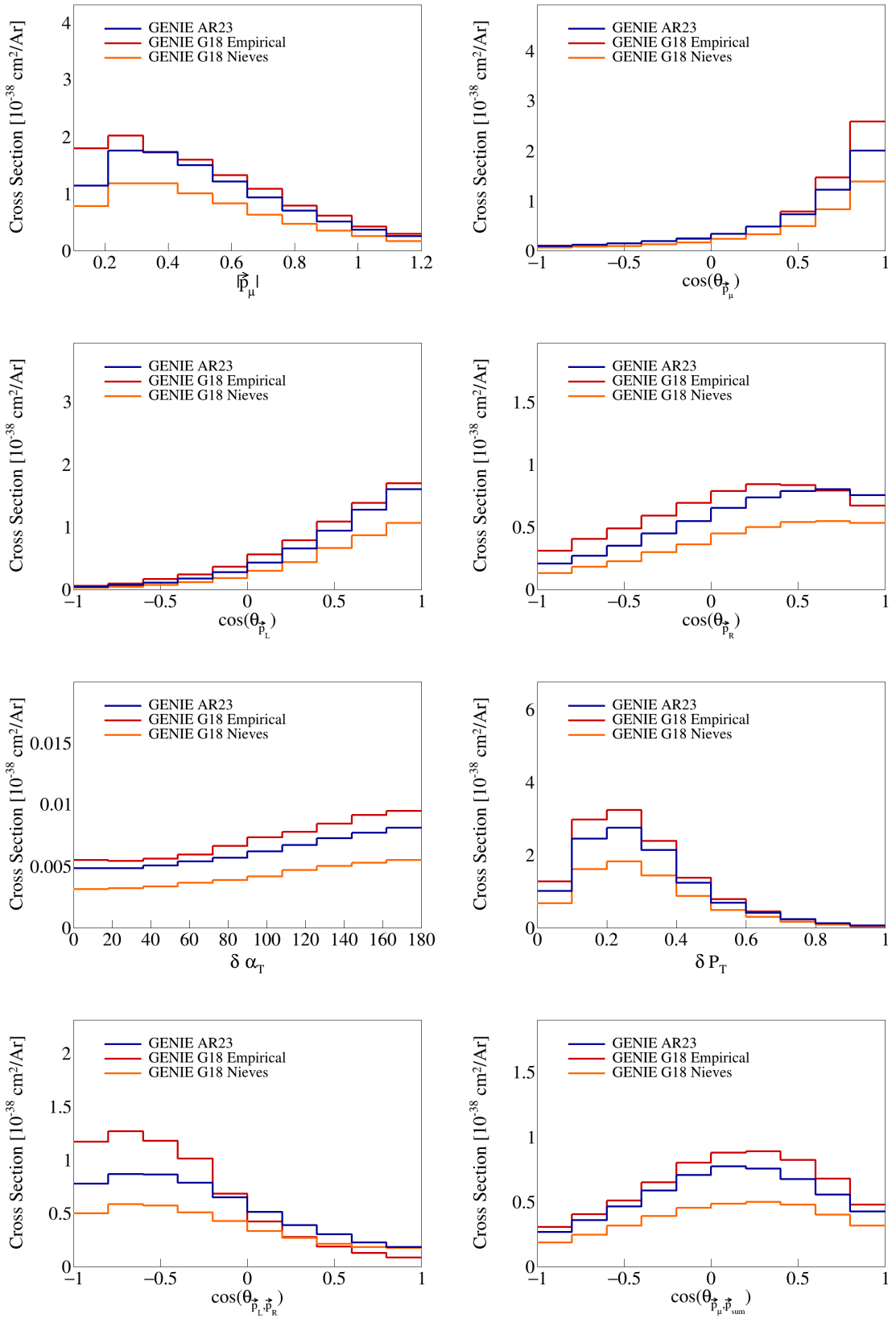


Figure 26: Variable plots for pure MEC events.

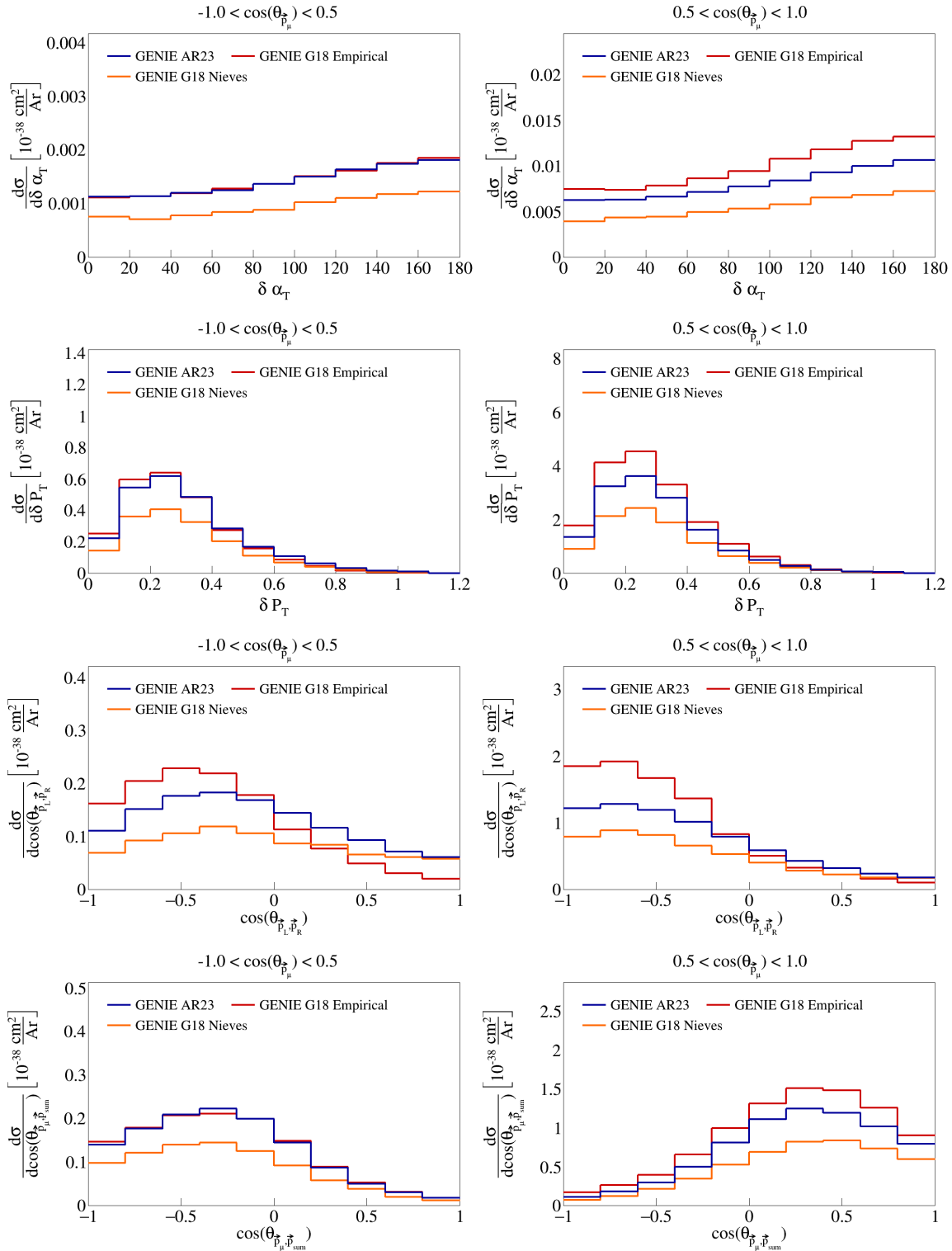


Figure 27: Sliced double differential plots for pure MEC events.

95 3 SBND analysis

96 The CAF files used for this analysis are available in the Fermilab gpvms at the path

97 `/pnfs/sbnd/persistent/users/apapadop/CAF_Files/*.flat.caf.root`

98 where the asterisk means that all the files in the directory with the extension `.flat.caf.root` will be used.

99 3.1 Fiducial volume

100 To perform the analysis of SBND data, we have to define the fiducial volume of the detector, which represents
101 a central part of the detector in which we will accept signals. The fiducial volume is given by the following
102 ranges:

$$5 < |x| < 180 \quad |y| < 180 \quad 10 < z < 450 \quad (6)$$

103 where x , y , and z are the coordinates in the detector frame, all in centimeters.

104 3.2 Signal definition

105 To perform analysis on experiment data, we will be using the CAFAna framework. This allows us to perform
106 cuts based on the reconstructed and Monte Carlo data (if available, i.e., only in the case of dealing with
107 simulated events), to discriminate events. To discriminate events based on their Monte Carlo data, we
108 perform a simple `TruthCut` that checks the following:

- 109 (i) That the neutrino interaction takes place in the fiducial volume.
- 110 (ii) That the neutrino is a muon neutrino.
- 111 (iii) That the interaction is a charged current interaction.
- 112 (iv) That there is only one muon in our allowed momentum range.
- 113 (v) That there are only two protons in our allowed momentum range.
- 114 (vi) That there are no charged/neutral pions in our defined momenta ranges.

115 Using the reconstructed event data, the cut we have to use is not as simple as in the Monte Carlo data
116 case. We now have to use a `Cut` that looks at different variables of the reconstructed event to determine if
117 it is a signal event. We perform the following cuts:

- 118 (i) Cosmic: that the event is not a cosmic event by Pandora's criteria, i.e., requiring `nu_score > 0.4` to
119 check how neutrino-like the event is, and `fmatch.score < 7` with $0 < fmatch.time < 1.8$ to check the
120 event comes from the beam.
- 121 (ii) Vertex in FV: that the reconstructed vertex for the neutrino interaction takes place in the fiducial
122 volume defined above.
- 123 (iii) One muon: that there is one muon track with $L_{\text{track}} > 50$ cm, starting point in the fiducial volume,
124 $\chi^2_\mu < 30$, $\chi^2_p > 60$, with momentum in our allowed range; if there are multiple candidate tracks, the
125 one with the longest track length is chosen.
- 126 (iv) Two protons: that there are two proton tracks with $\chi^2_p < 100$, full track in the fiducial volume, and
127 that these have momentum in our allowed range.
- 128 (v) No charged pions: that there are no other reconstructed tracks with momentum in the allowed range
129 for charged pions inside the fiducial volume.
- 130 (vi) No neutral pions: that there are no reconstructed particles with a positive `trackScore` less than 0.5
131 indicating a shower, so we don't allow any neutral pions.

Cut	Number of events	Global efficiency	Signal efficiency	Purity
All	1.31823e7	-	-	-
True signal events	273751	-	-	-
All reco events	6.61683e6	100%	-	-
Cosmic cut	5.46987e6	82.6659%	89.0567%	4.45703%
Vertex in FV cut	3.10952e6	46.9941%	87.5899%	7.7111%
One muon cut	2.14513e06	32.4193%	69.629%	8.88571%
Two protons cut	137309	2.07514%	16.3503%	32.5975%
No charged pions cut	65938	0.99652%	12.1369%	50.3881%
No neutral pions cut	54088.9	0.817444%	10.929%	55.313%

Table 2: Global efficiency, selection efficiency, and purity for cuts made in signal definition.

132 Using these two discriminators on simulated events, the reconstructed events that satisfy the signal definition,
 133 and distinguish between true signal events and background events.

134 We use a one-bin histogram with lower bound 0 and upper bound of 3 in the true energy variable to get
 135 total counts of generated events, true signal events, all reconstructed events, and efficiency and purity data
 136 after each of the cuts described above is applied to the reconstructed events. These results are shown in
 137 Table 2. Counts are obtained using ROOT’s command `Histo->Integral()`. Global efficiency is defined as
 138 the ratio between events that pass the cut and reconstructed events, signal efficiency as the ratio between
 139 true events that pass the cut and the all true signal events, and purity as the ratio between true signal events
 140 that pass the cut and all events that pass the cut. The numbers reported in this table are POT normalized
 141 to 6.6×10^{20} .

142 3.3 Variable plots

143 Using all the variable definitions as we did when studying the event generators, and the signal definition
 144 based on the cuts described in the previous section, we can generate plots for SBND data. The reconstructed
 145 single differential variables corresponding to vector opening angles and magnitudes are shown in Figure 28.
 146 In these figures, three lines are shown, corresponding to: all reconstructed (all the reconstructed events that
 147 pass our signal definition), signal (reconstructed events that pass signal definition and are true signal events
 148 as determined by the `TruthCut` from our previous section), and background (reconstructed events that pass
 149 signal definition but are not true signal events) events. Similarly, the variables relating multiple vectors are
 150 shown in Figure 29, and double differential sliced variables are shown in Figure 30.

151 3.4 Signal efficiency

152 Using the truth information about reconstructed events, we can also compute signal efficiency on a bin-by-
 153 bin basis. To be precise, signal definition on a bin *i* is defined as the ratio between the number of events
 154 generated in bin *i* and reconstructed in any bin over the number of events generated in bin *i*. These plots
 155 are shown in Figure 31 and Figure 32 for single-differential variables and Figure 33 for double differential
 156 variables.

157 3.5 Migration and response matrices

158 Further, we compute migration matrices which give us a measure of how reliable our reconstructed variables
 159 are. A given column in this matrix represents a bin of the truth variable, i.e., the value with which the
 160 event was generated. Then, each row corresponds to a reconstructed bin of the same variable, and each cell
 161 corresponds to the probability that an event generated with the truth value corresponding to the column gets
 162 reconstructed with the value corresponding to the row. For the migration matrix, we consider true signal
 163 events that were reconstructed and satisfy our signal definition in the denominator. Therefore, the values in
 164 each column must add up to 1. The migration matrices for the single differential variables are presented in

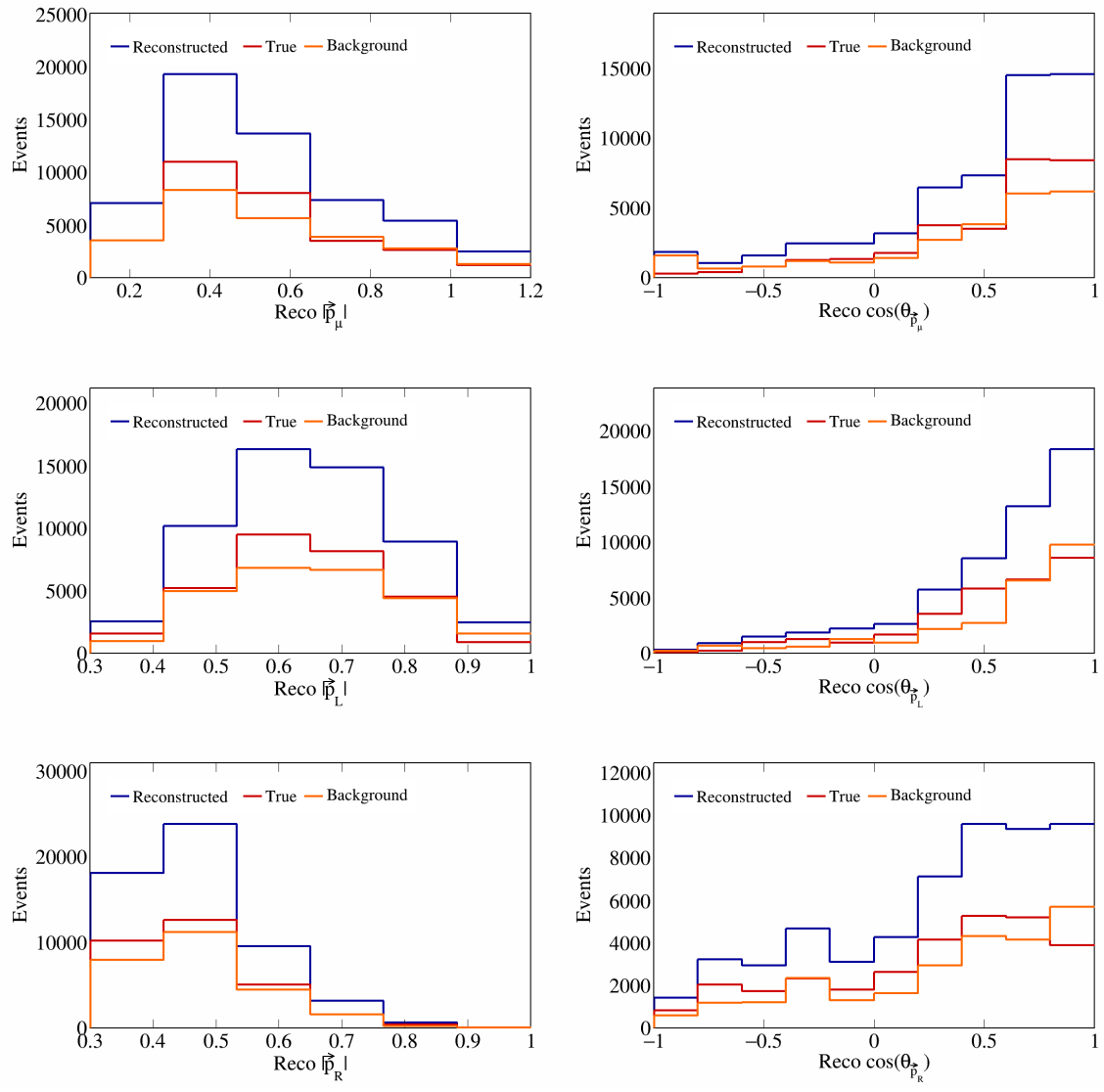


Figure 28: Vector directions and magnitudes for SBND data.

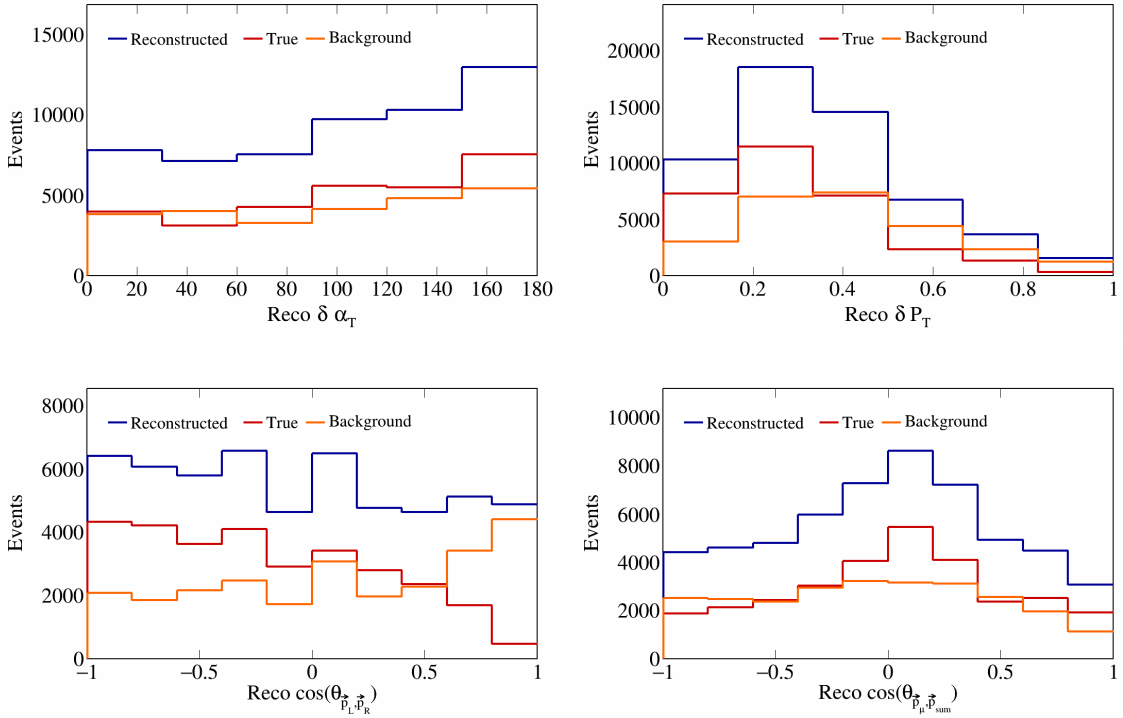


Figure 29: Vector opening angles and transverse momentum for SBND data.

165 Figure 34 and Figure 35. The migration matrices for the double differential variables (given in terms of the
 166 bin number) are presented in Figure 36.

167 Response matrices are computed in a similar manner, but using the total number of generated events in the
 168 denominator when computing the ratios, i.e., without requiring the events to be successfully reconstructed.
 169 Therefore, for these matrices, the columns of the response matrices do not have to add up to 1. The response
 170 matrices for single differential variables are presented in Figure 37 and Figure 38, and the double differential
 171 response matrices are given in Figure 39.

172 3.6 Systematics

173 To include systematic uncertainties in our study, we first consider cross sectional systematics. These are
 174 variations in the cross section models used to generate the events. They can be of two types: multisigma
 175 and multisim. For the former, we consider a 1σ variation of the affected parameters, and in the latter we
 176 consider one hundred universes, each with a random variation picked from a Gaussian distribution between
 177 0σ and 1σ . From these variations, we compute the covariance matrix as

$$178 E_{i,j} = \frac{1}{N_{\text{Univ}}} \sum_{s=1}^{N_{\text{Univ}}} (\tilde{\sigma}_i^{\text{Var},s} - \tilde{\sigma}_i^{\text{CV}})(\tilde{\sigma}_j^{\text{Var},s} - \tilde{\sigma}_j^{\text{CV}}) \quad (7)$$

179 where $\tilde{\sigma}_i^{\text{Var},s}$ represents the variation cross section of the variable in the i -th bin in the s -th universe, and
 180 $\tilde{\sigma}_i^{\text{CV}}$ is the central value (without any variation) of the cross section in the i -th bin. Then, the fractional
 covariance matrix is defined as

$$181 F_{i,j} = \frac{E_{i,j}}{\tilde{\sigma}_i^{\text{CV}} \tilde{\sigma}_j^{\text{CV}}}. \quad (8)$$

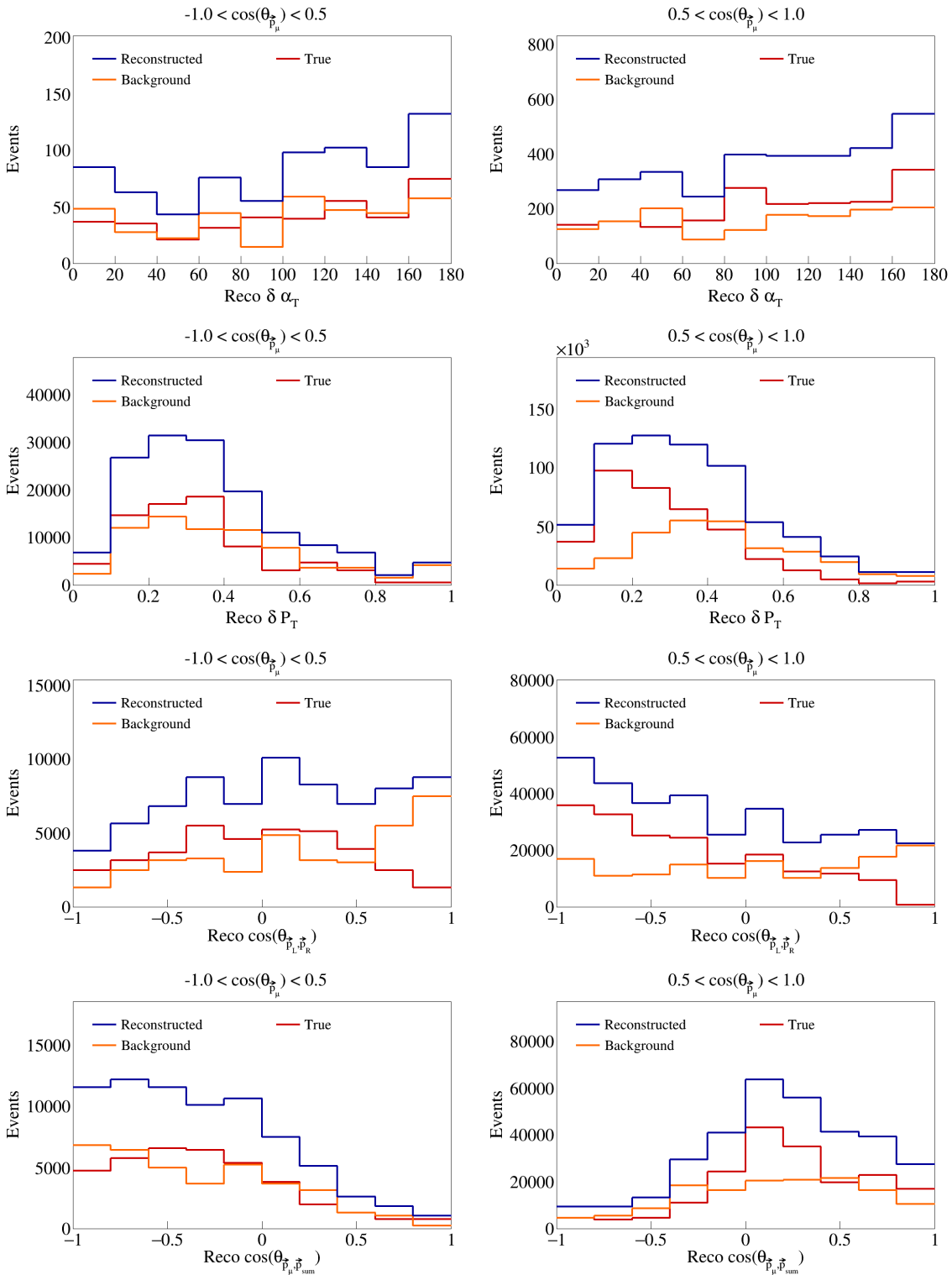


Figure 30: Sliced double differential plots for SBND events.

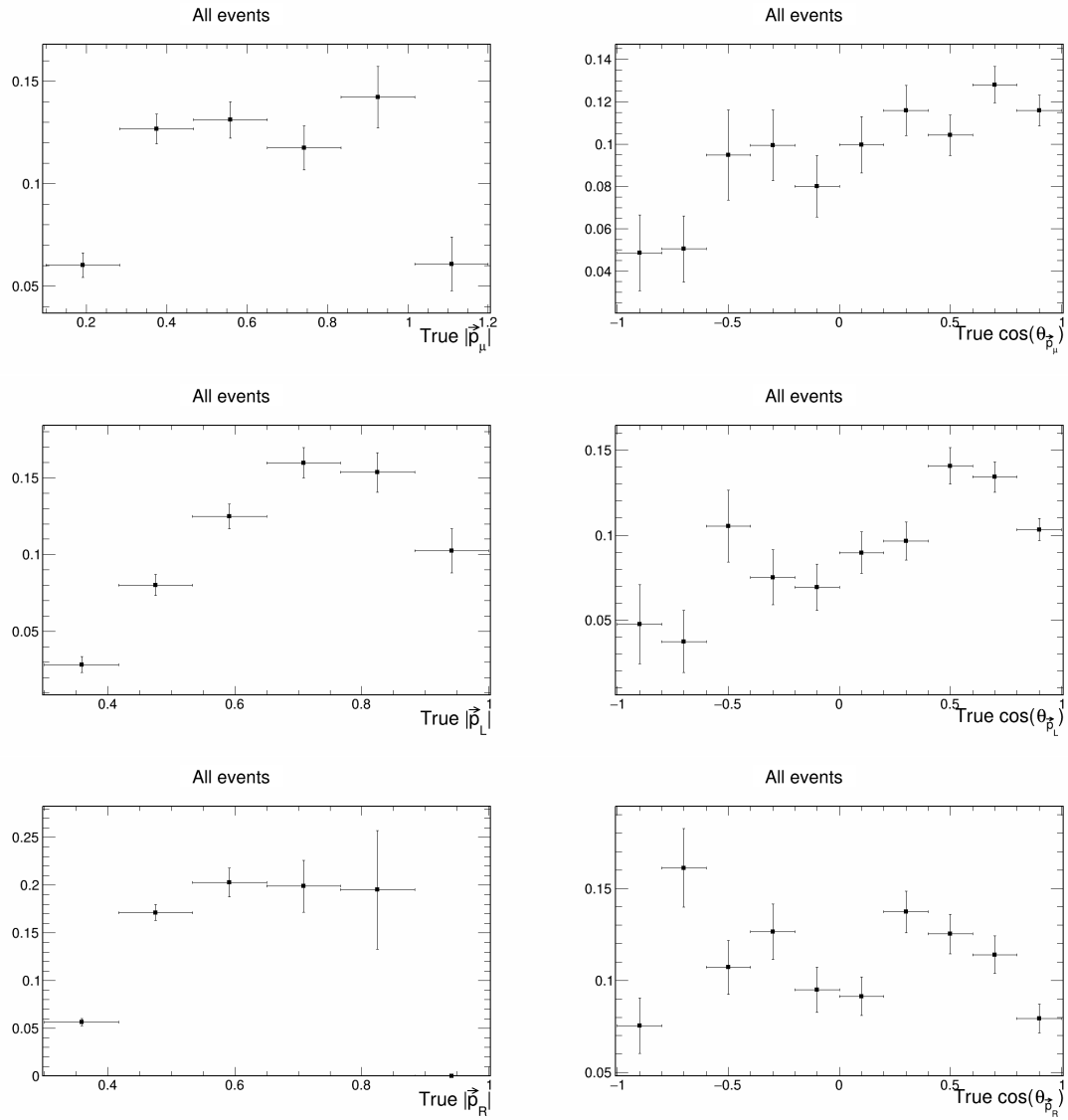


Figure 31: Signal efficiency plots for single differential vector directions and magnitudes.

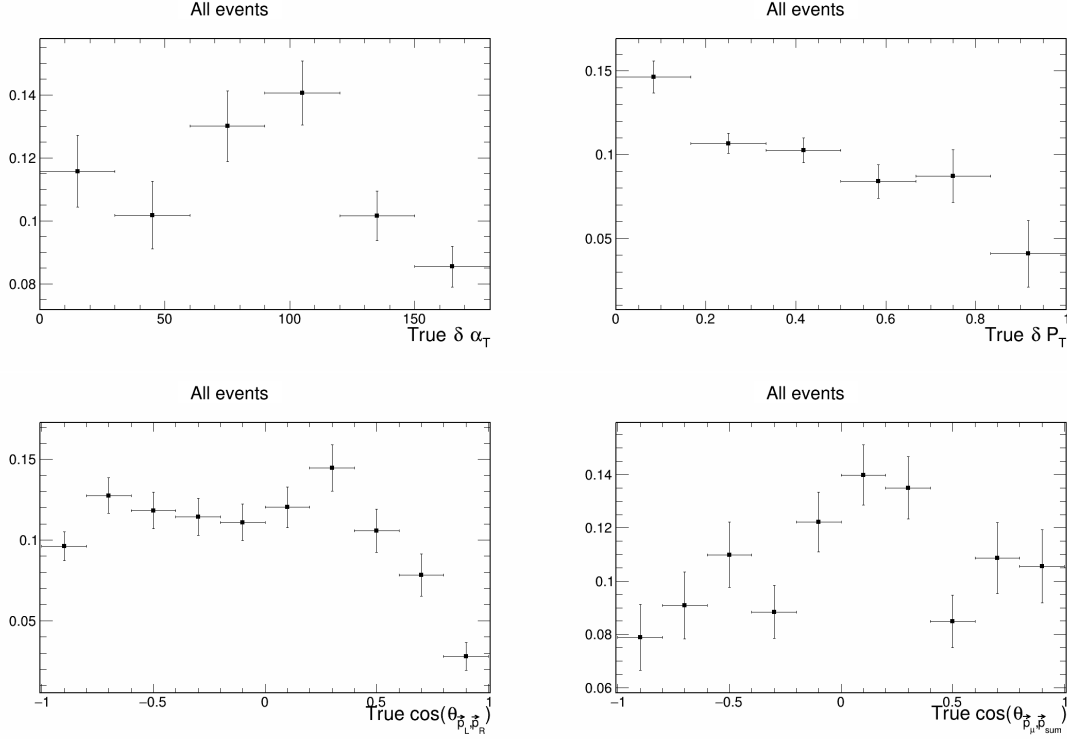


Figure 32: Signal efficiency plots for single differential vector opening angles and transverse momentum.

181 And the correlation matrix is defined as

$$\rho_{i,j} = \frac{E_{i,j}}{\sqrt{E_{i,i}E_{j,j}}}. \quad (9)$$

182 In the case of a multisigma systematic, $N_{\text{Univ}} = 1$, and for a multisim systematic, $N_{\text{Univ}} = 100$. The plots
183 for all the individual cross sectional systematics are shown in Appendix 6.1. There are a few systematics
184 that are currently crashing when trying to produce all plots. This are:

- 185 • MINERvAq0q3Weighting_SBND_v1_Mnv2p2hGaussEnhancement
- 186 • MiscInteractionSysts_SBND_v1_nuenuubar_xsec_ratio
- 187 • MiscInteractionSysts_SBND_v1_nuenumu_xsec_ratio
- 188 • NOvAStyleNonResPionNorm_SBND_v1_NR_nu_np_CC_1Pi

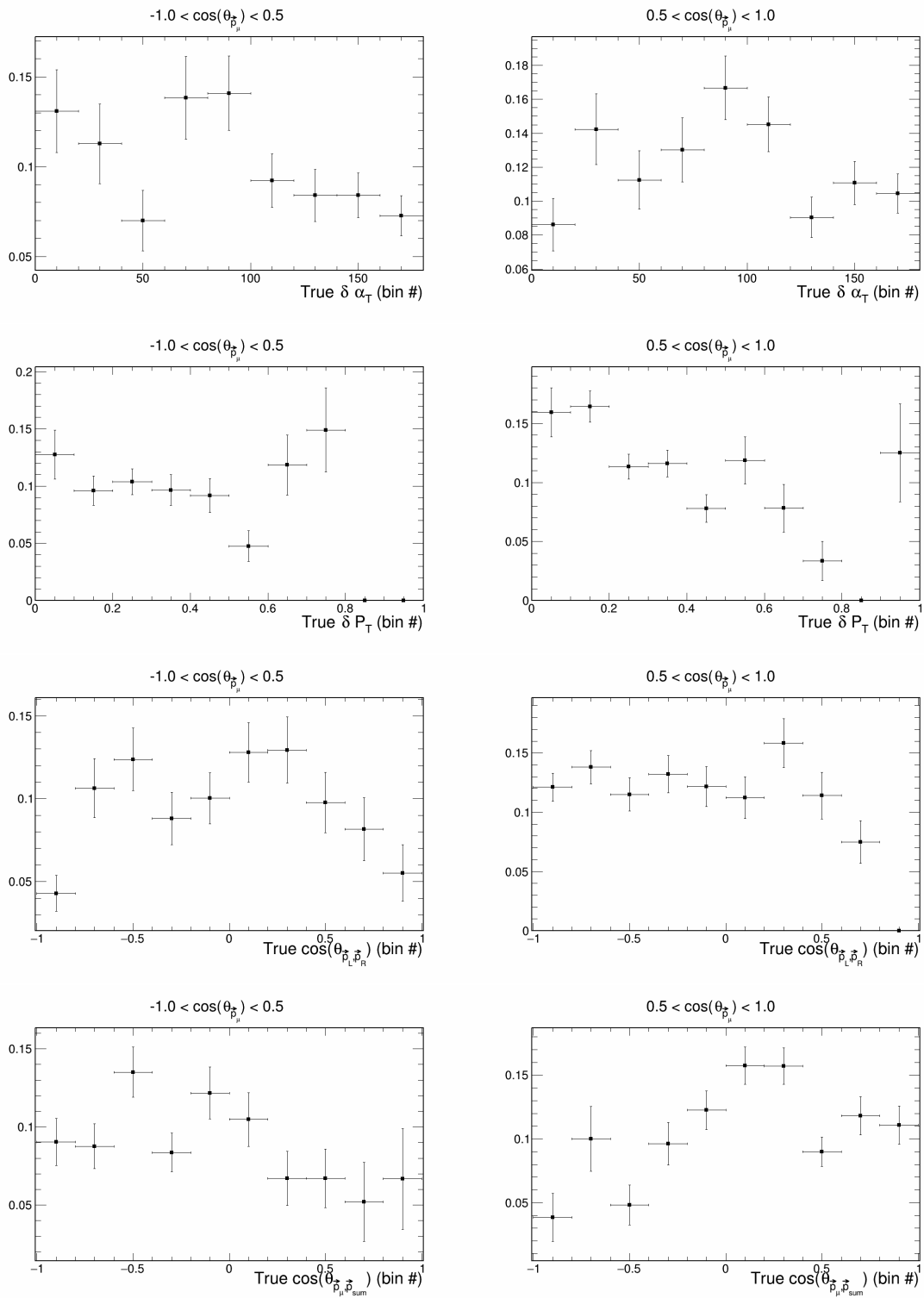


Figure 33: Signal efficiency plots for double differential variables.

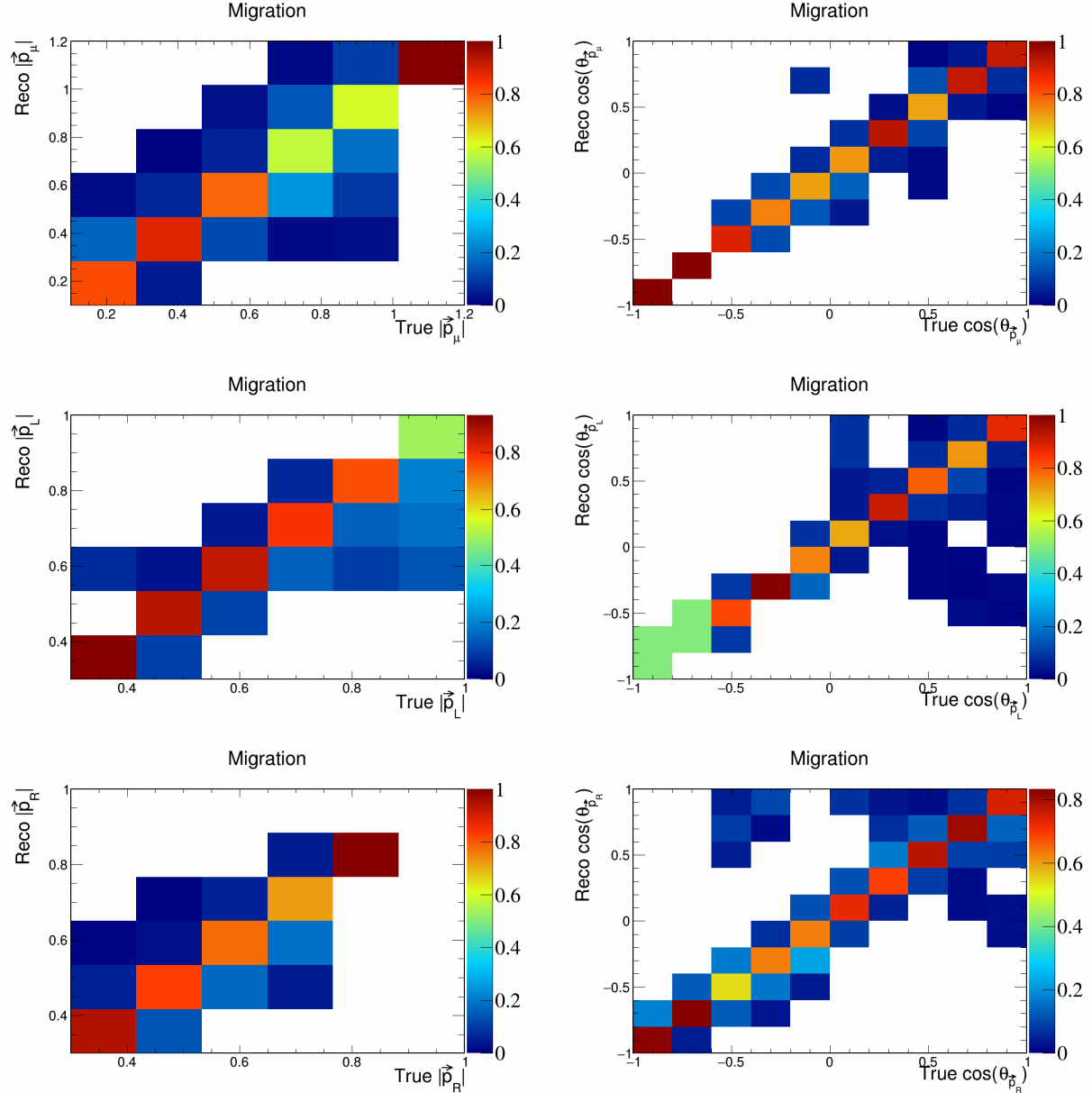


Figure 34: Migration matrices for signal differential vector directions and magnitudes.

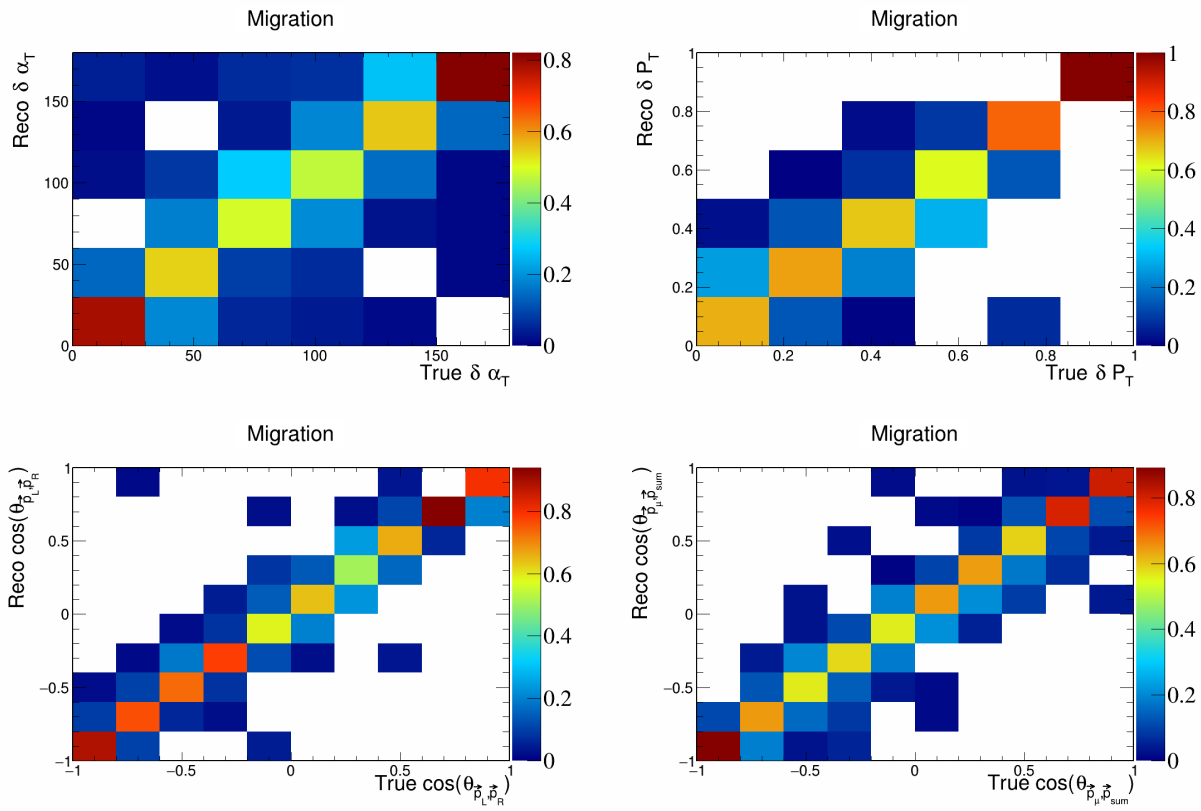


Figure 35: Migration matrices for signal differential vector opening angles and transverse momentum.

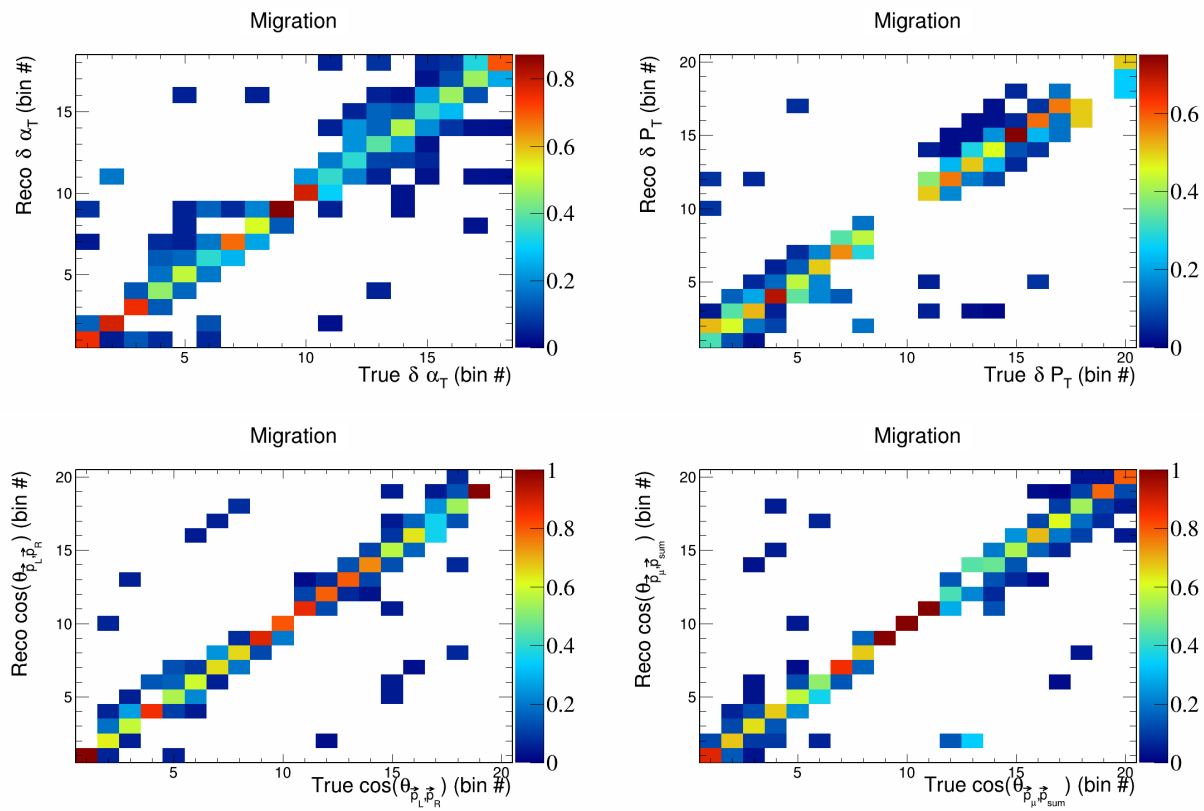


Figure 36: Migration matrices for double differential variables.

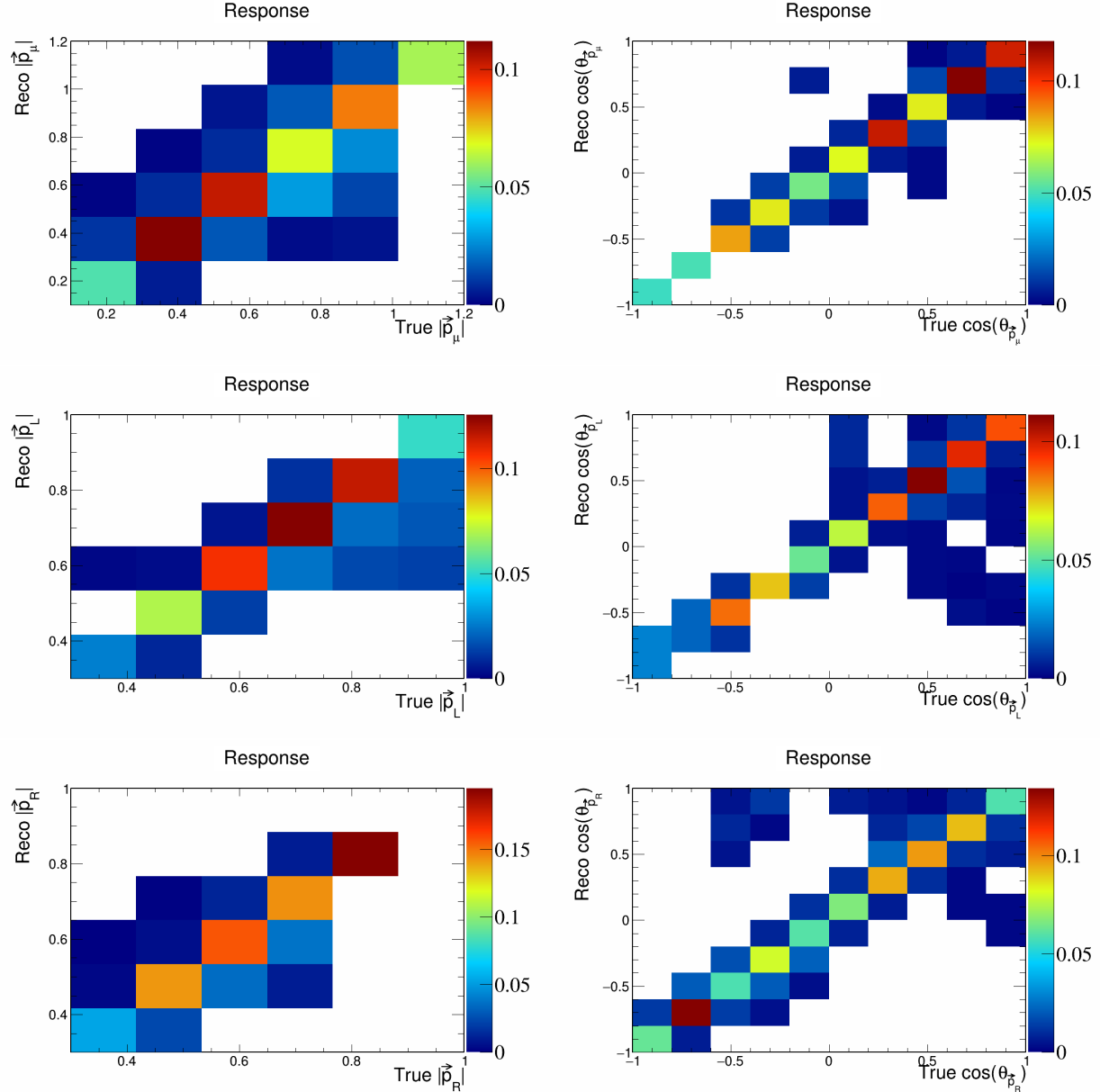


Figure 37: Response matrices for signal differential vector directions and magnitudes.

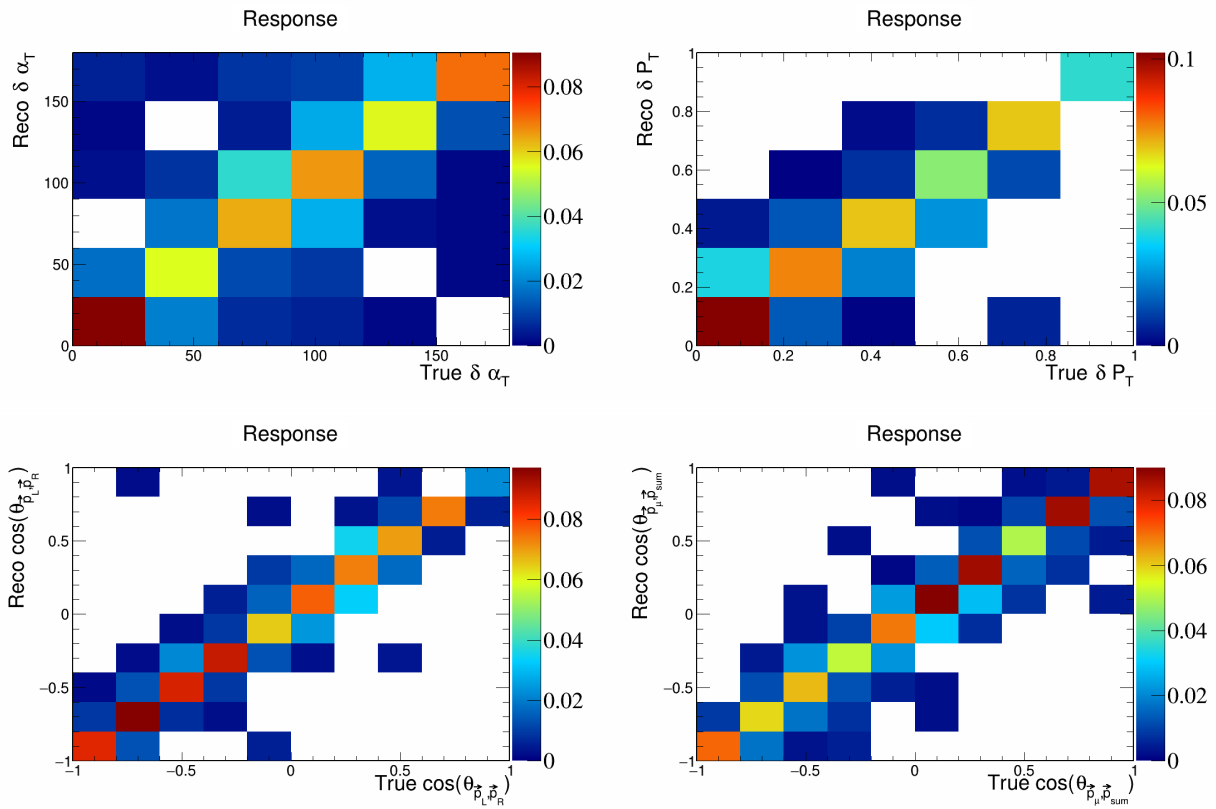


Figure 38: Response matrices for signal differential vector opening angles and transverse momentum.

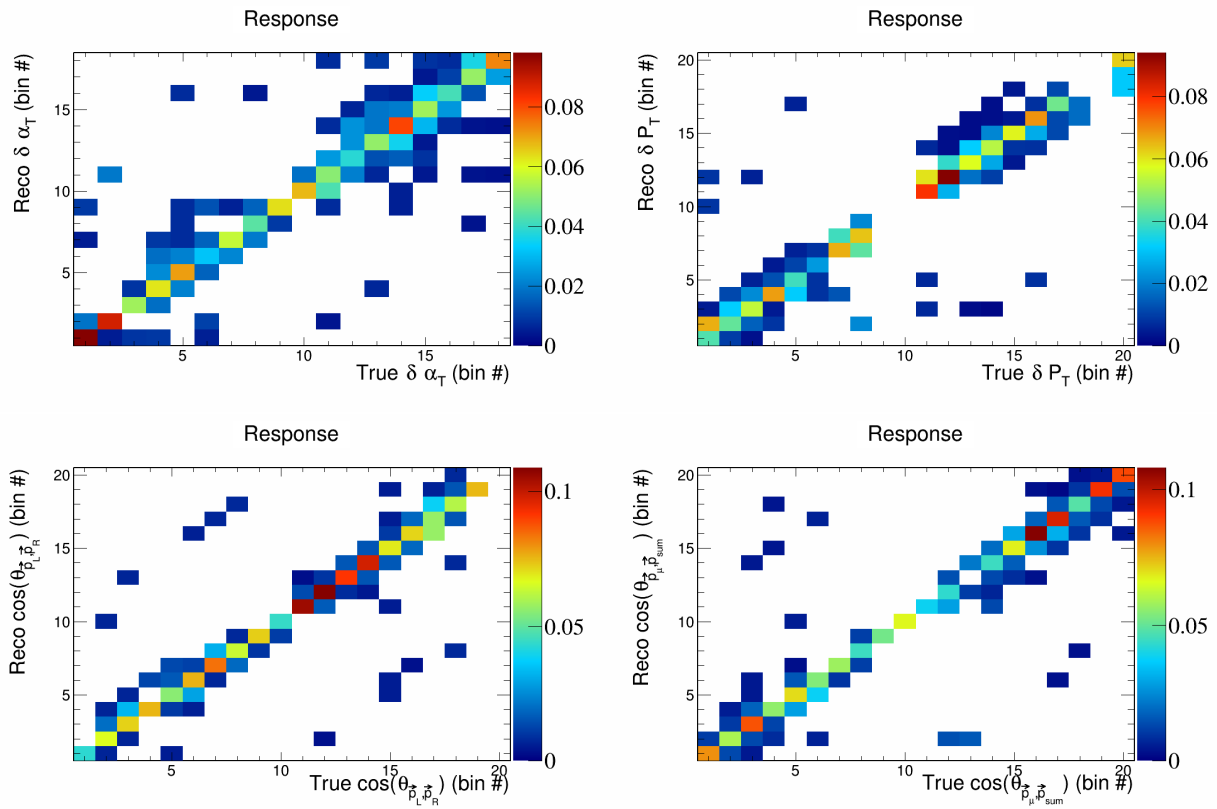


Figure 39: Response matrices for double differential variables.

₁₈₉ **4 Closure test**

₁₉₀ To ensure that the unfolding techniques that we will implement work correctly, we perform a closure test,
₁₉₁ meaning that we will perform the unfolding on simulated true signal events and check that the unfolded
₁₉₂ data matches the true signal data with added smearing. We can see that the plots that perform this test
₁₉₃ in Figure 40 and Figure 41. We also note that the overall shape and magnitude of our histograms match
₁₉₄ previously reported MicroBooNE analyses. **TODO: stop using dummy covariance matrices.**

₁₉₅ **5 Cross-section results**

₁₉₆ Placeholder.

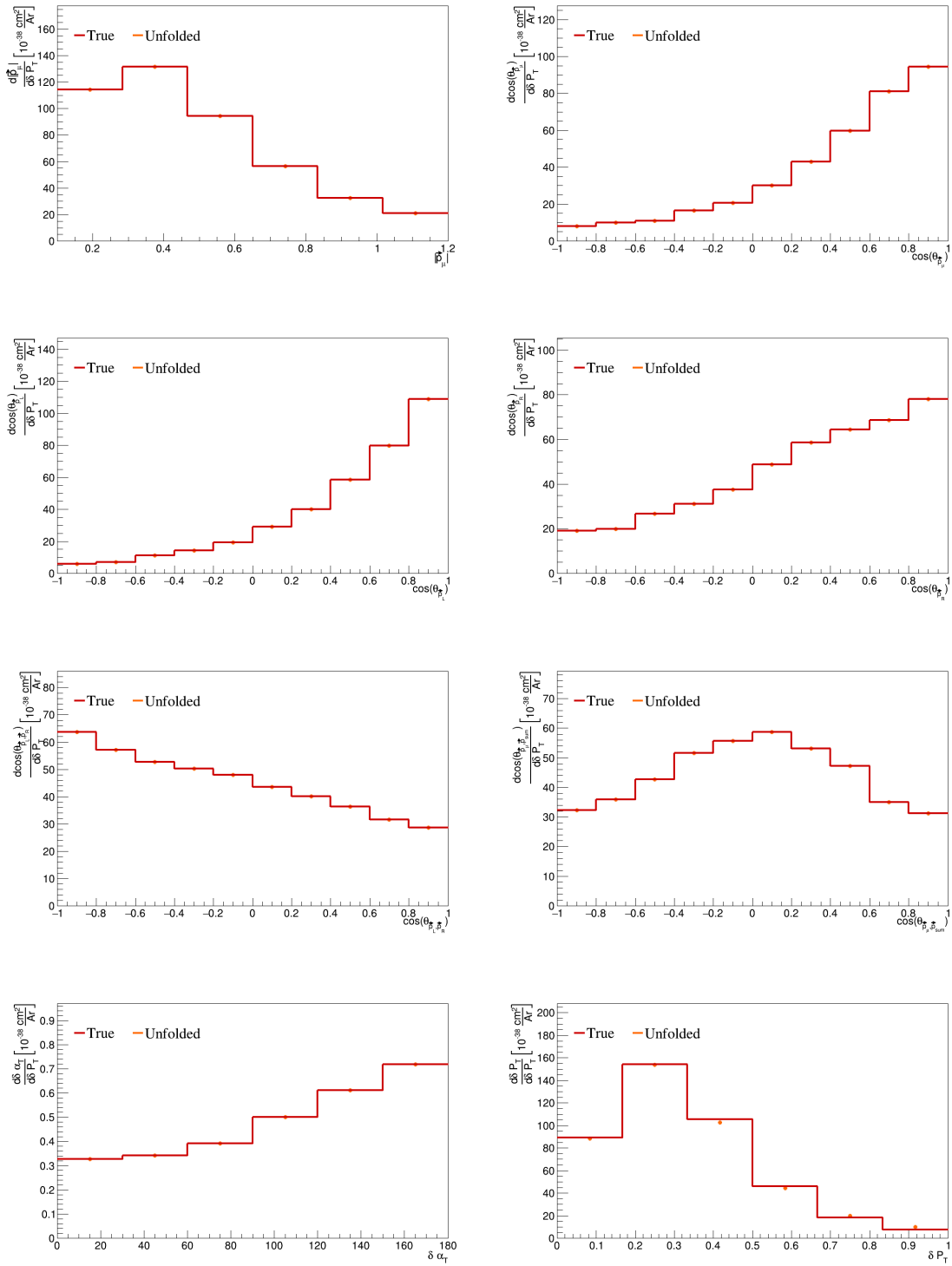


Figure 40: Closure test single differential plots.

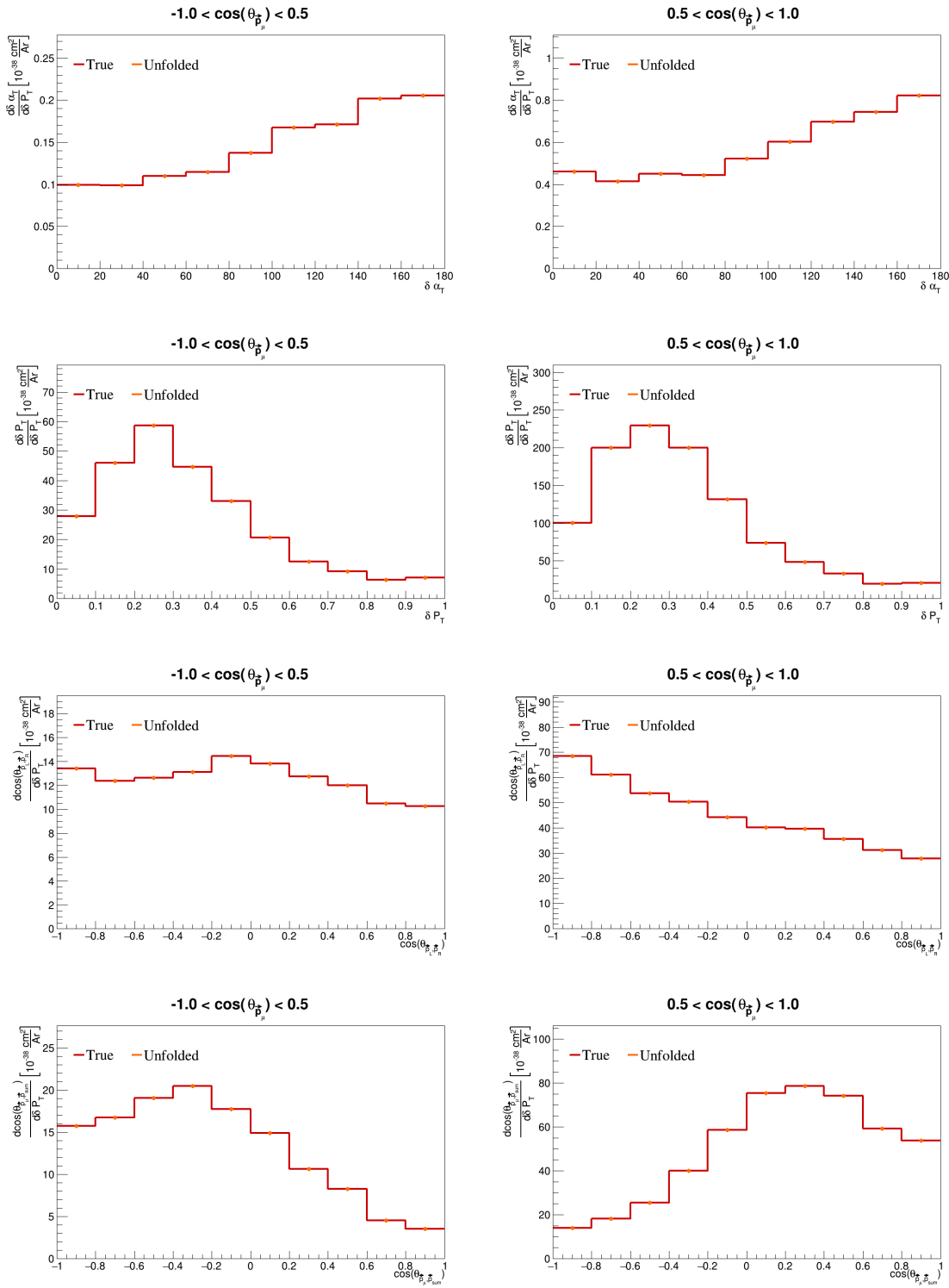


Figure 41: Closure test double differential plots.

197 **6 Appendices**

198 **6.1 Cross section systematics**

199 In this appendix, the variations, covariance matrices, fractional covariance matrices, and correlation matrices
200 are plotted for all of the cross section systematics and variables.

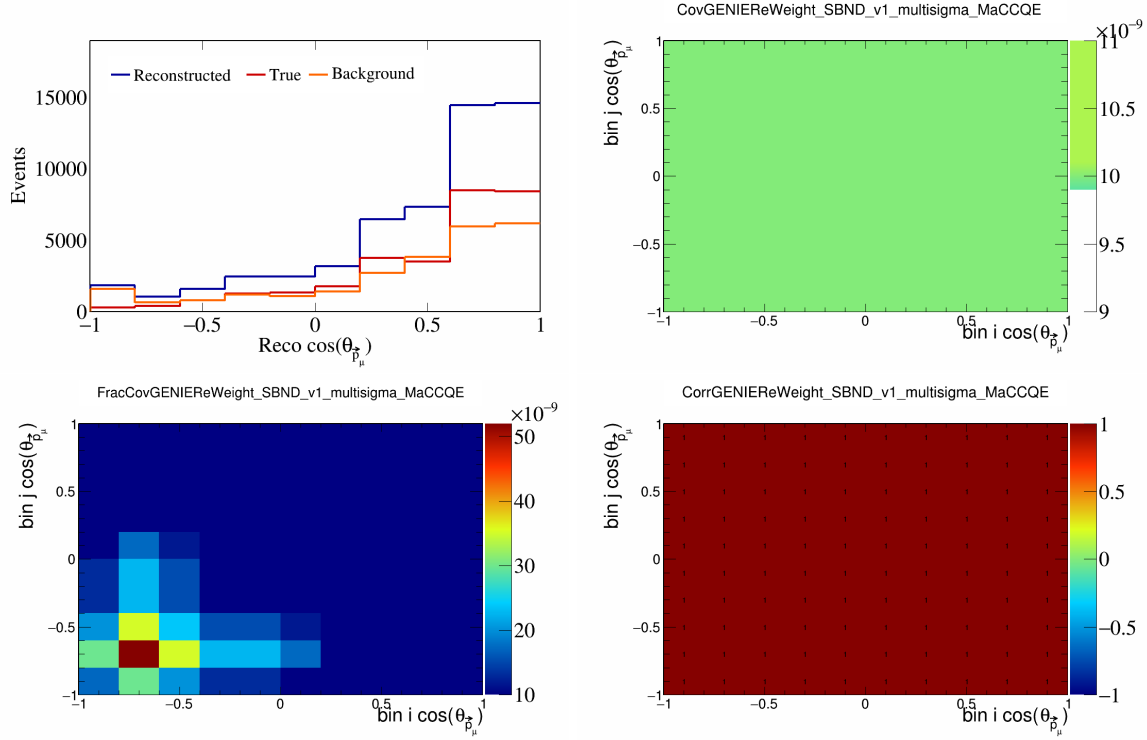


Figure 42: GenieMaCCQE variations for $\cos(\theta_{\vec{p}_\mu})$.

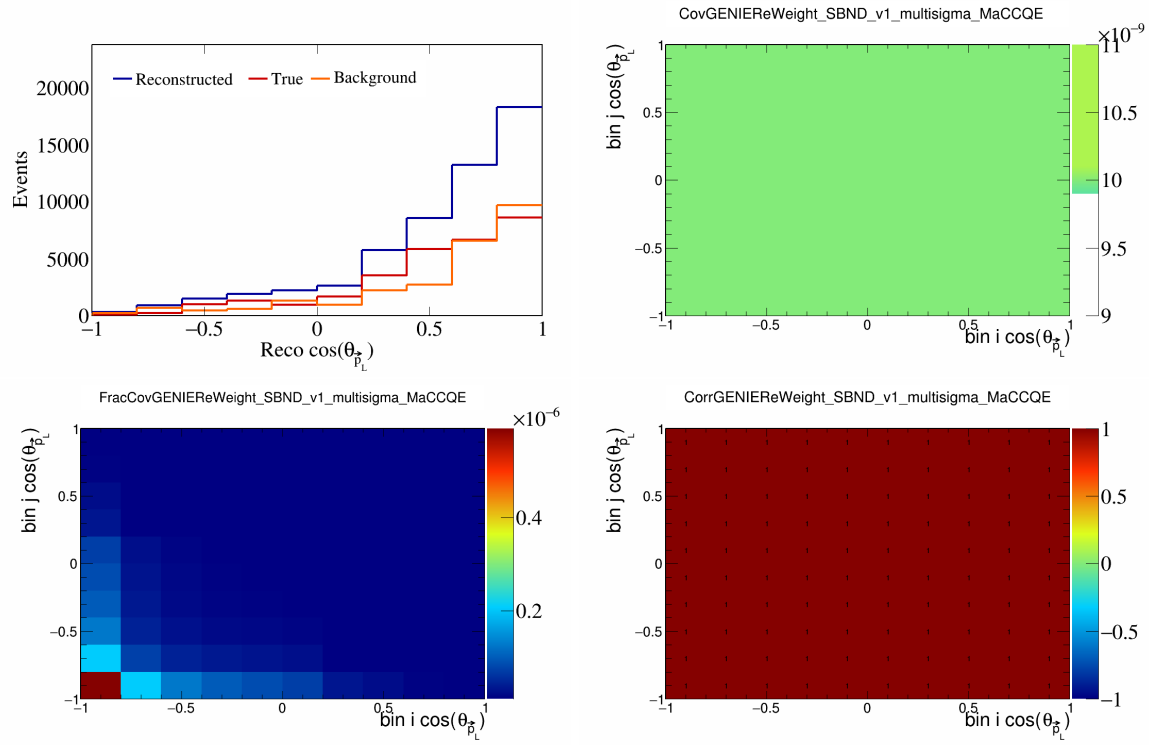


Figure 43: GenieMaCCQE variations for $\cos(\theta_{\vec{p}_L})$.

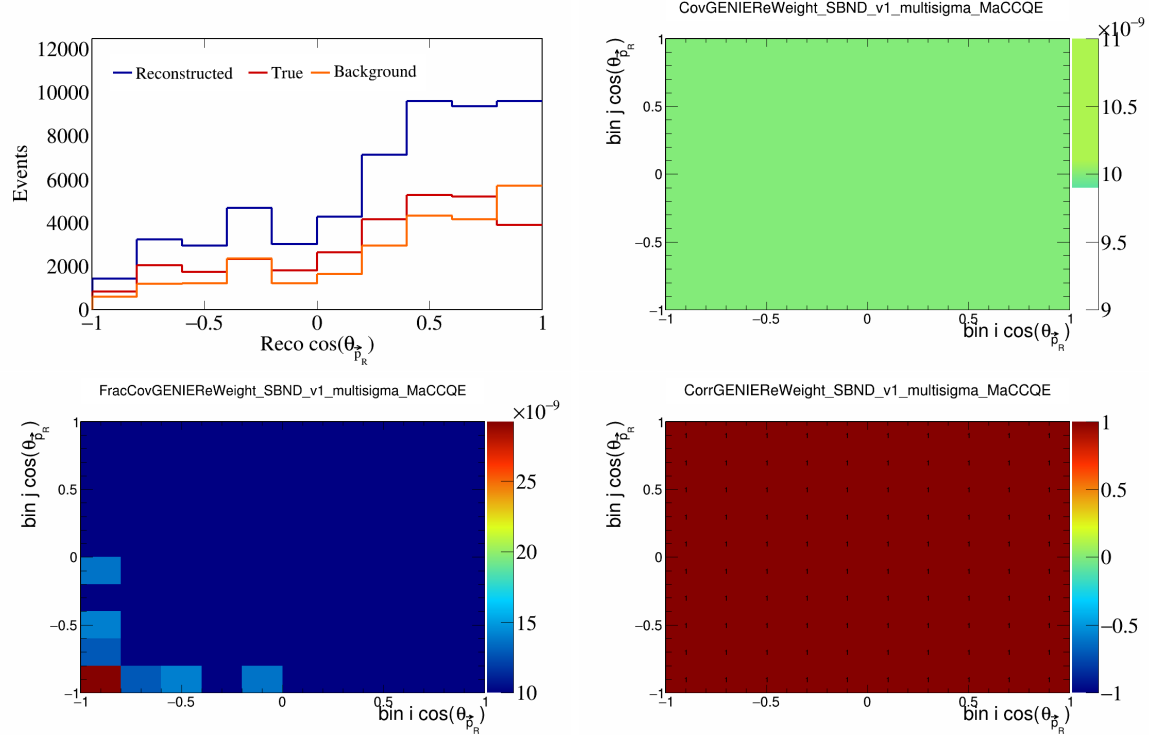


Figure 44: GenieMaCCQE variations for $\cos(\theta_{\vec{p}_R})$.

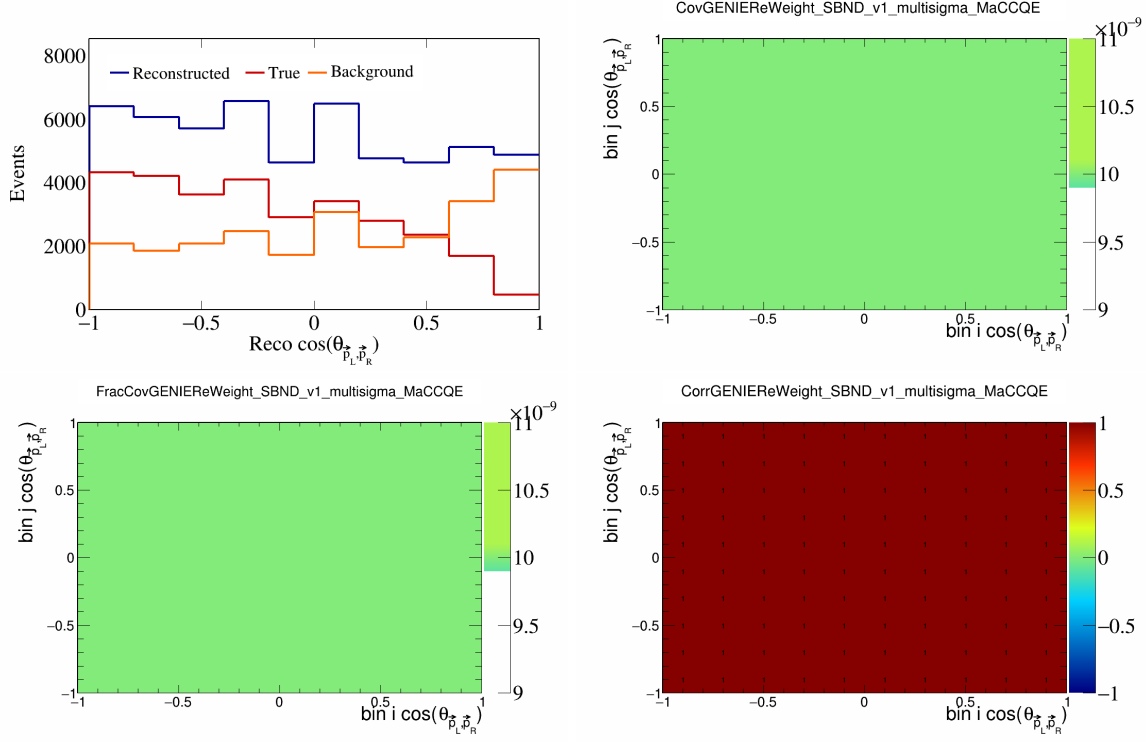


Figure 45: GenieMaCCQE variations for $\cos(\theta_{\vec{p}_L, \vec{p}_R})$.

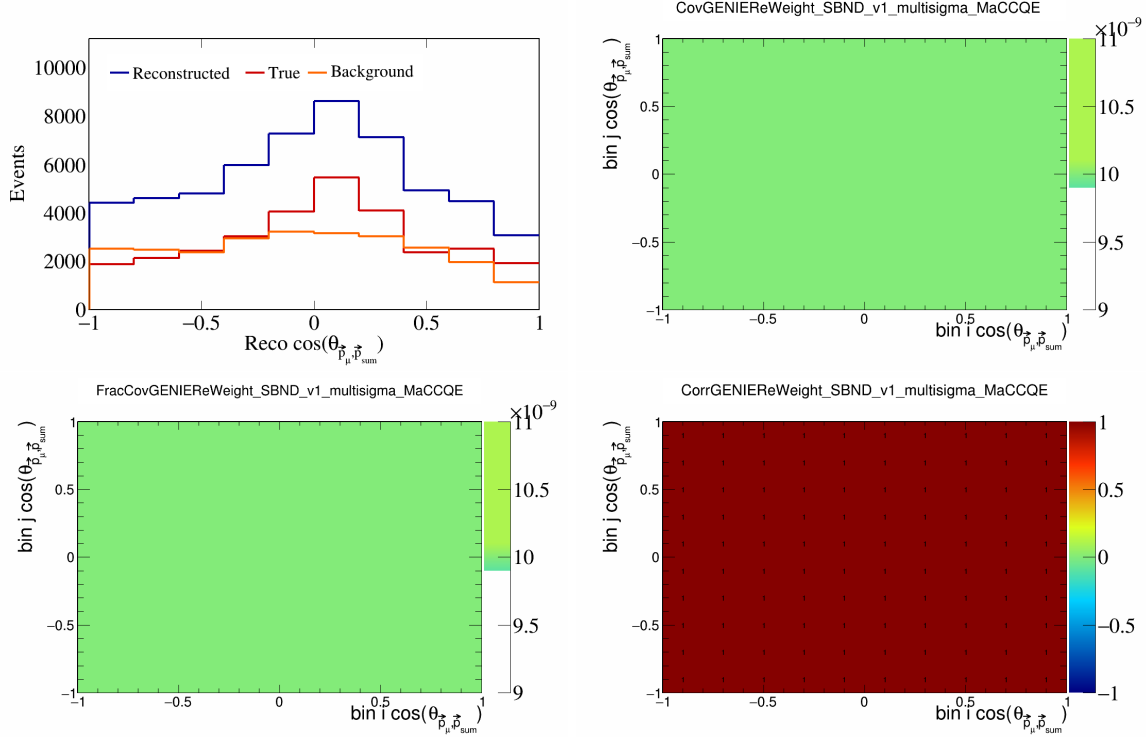


Figure 46: GenieMaCCQE variations for $\cos(\theta_{\vec{p}_\mu, \vec{p}_{\text{sum}}})$.

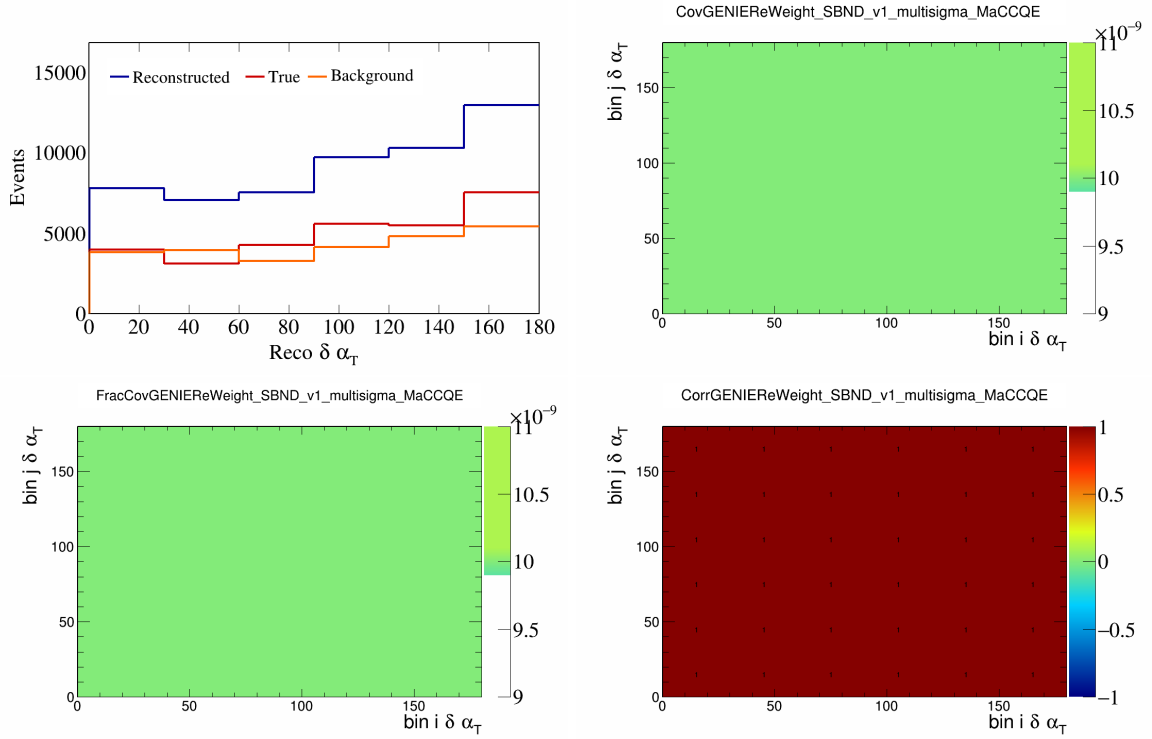


Figure 47: GenieMaCCQE variations for $\delta \alpha_T$.

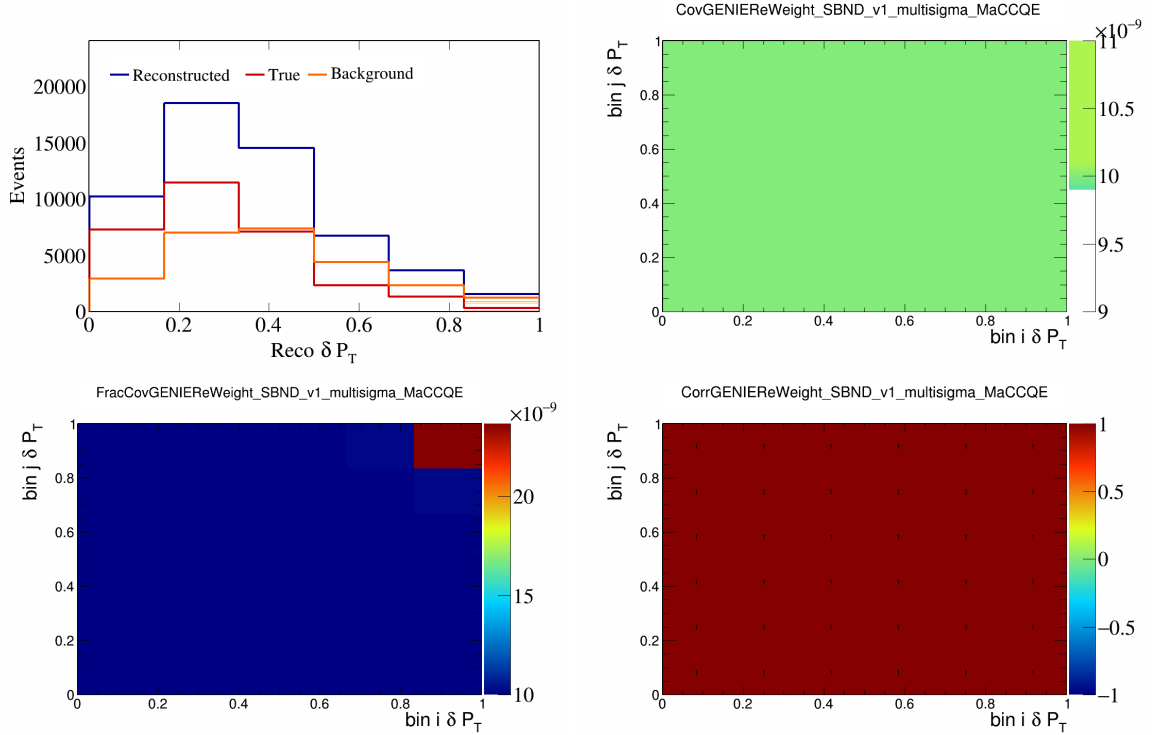


Figure 48: GenieMaCCQE variations for δP_T .

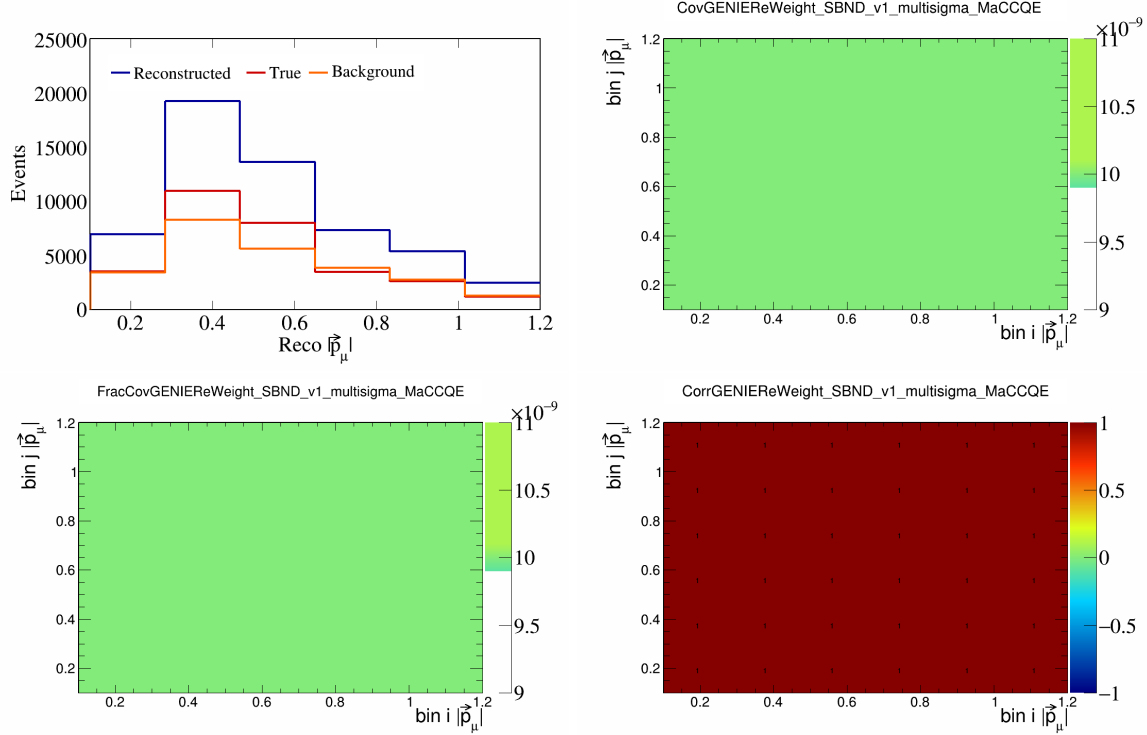


Figure 49: GenieMaCCQE variations for $|\vec{p}_\mu|$.

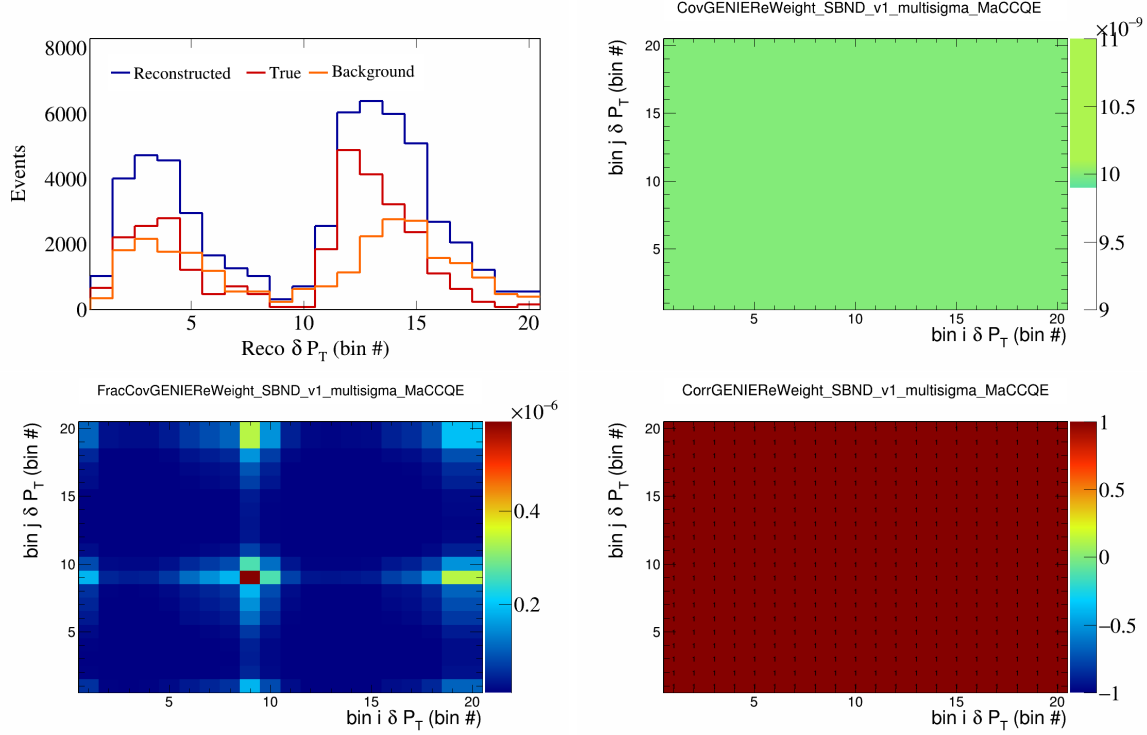


Figure 50: GenieMaCCQE variations for δP_T in $\cos(\theta_{\vec{p}_\mu})$.

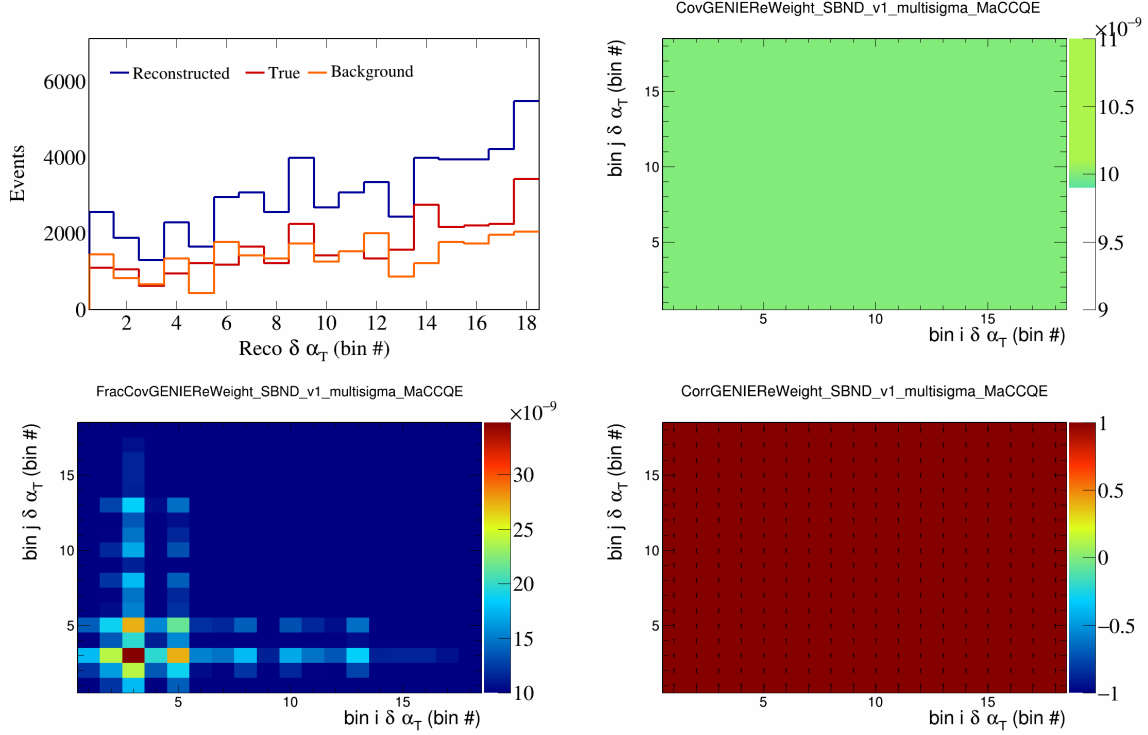


Figure 51: GenieMaCCQE variations for $\delta \alpha_T$ in $\cos(\theta_{\vec{p}_\mu})$.

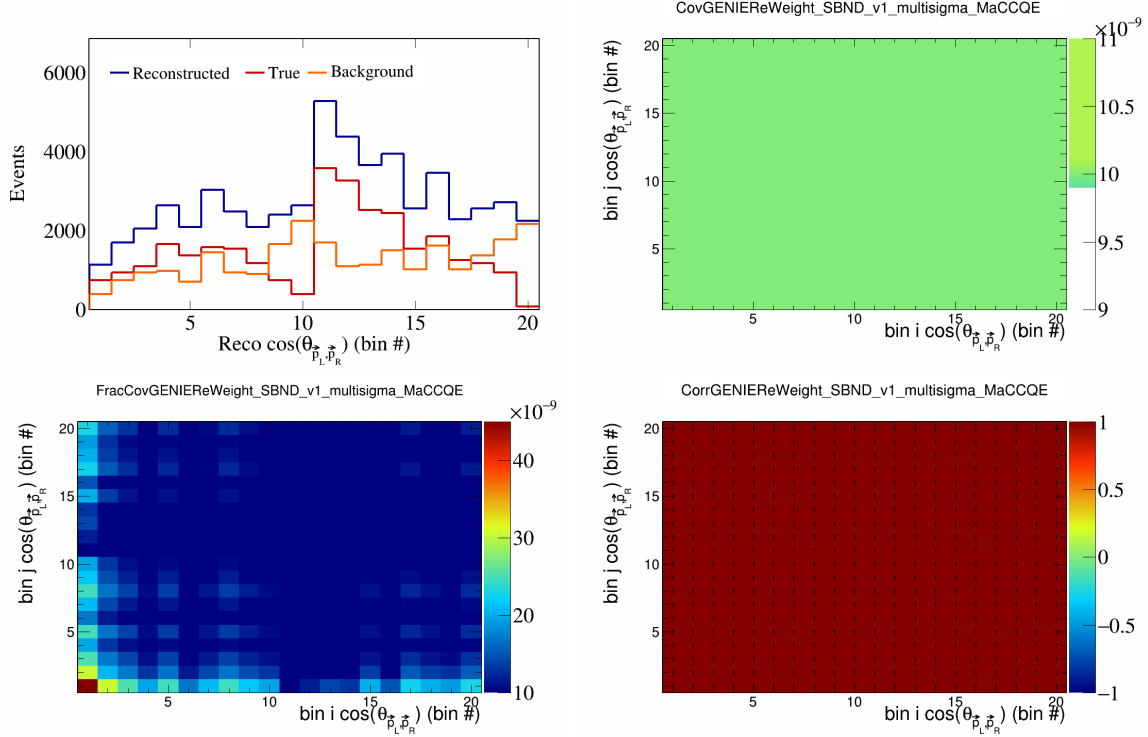


Figure 52: GenieMaCCQE variations for $\cos(\theta_{\vec{p}_L, \vec{p}_R})$ in $\cos(\theta_{\vec{p}_\mu})$.

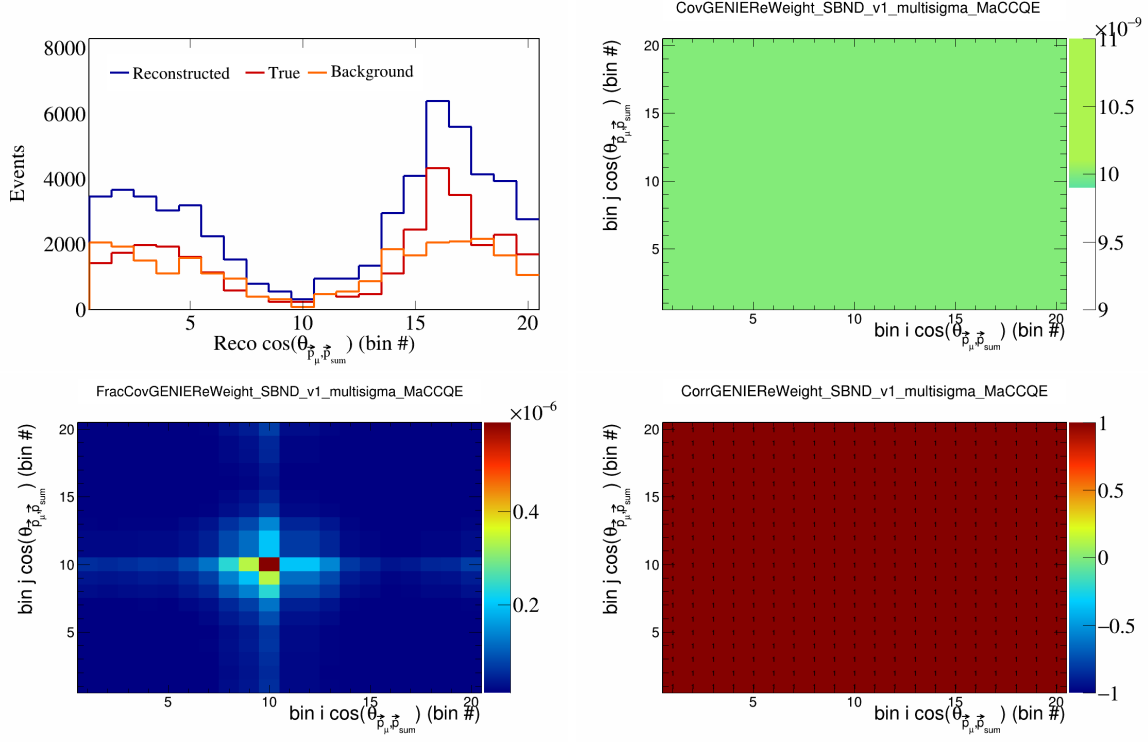


Figure 53: GenieMaCCQE variations for $\cos(\theta_{\vec{p}_\mu, \vec{p}_{\text{sum}}})$ in $\cos(\theta_{\vec{p}_\mu})$.

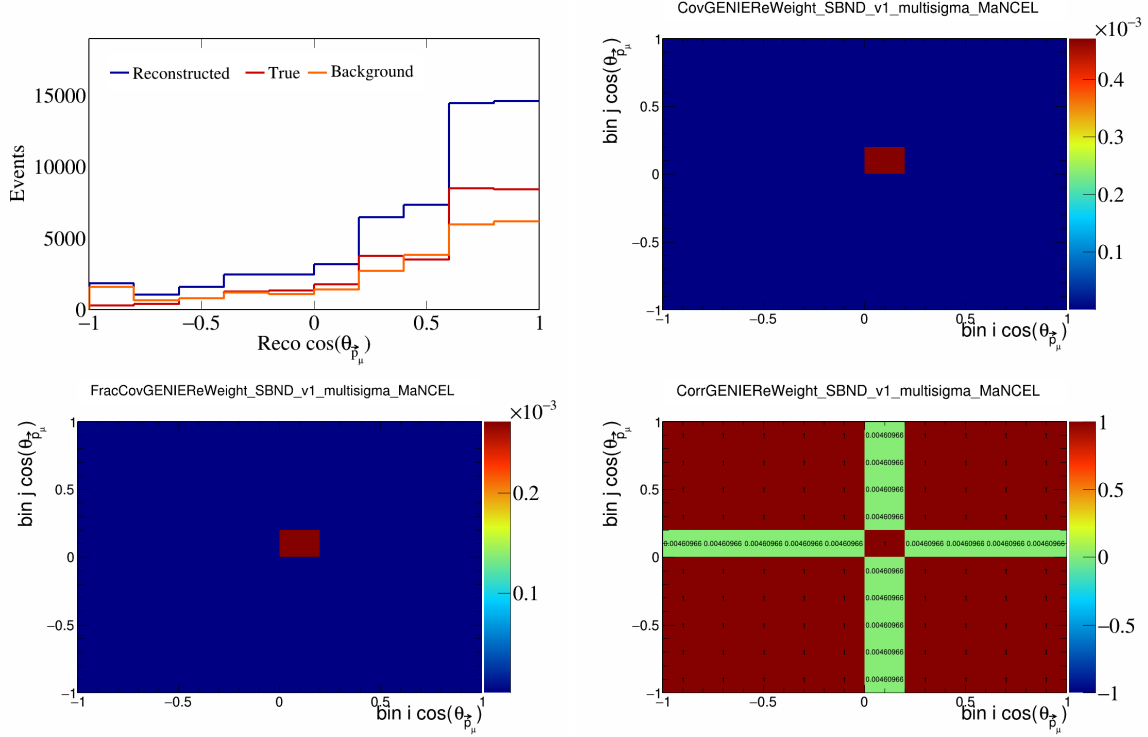


Figure 54: GenieMaNCEL variations for $\cos(\theta_{\vec{p}_\mu})$.

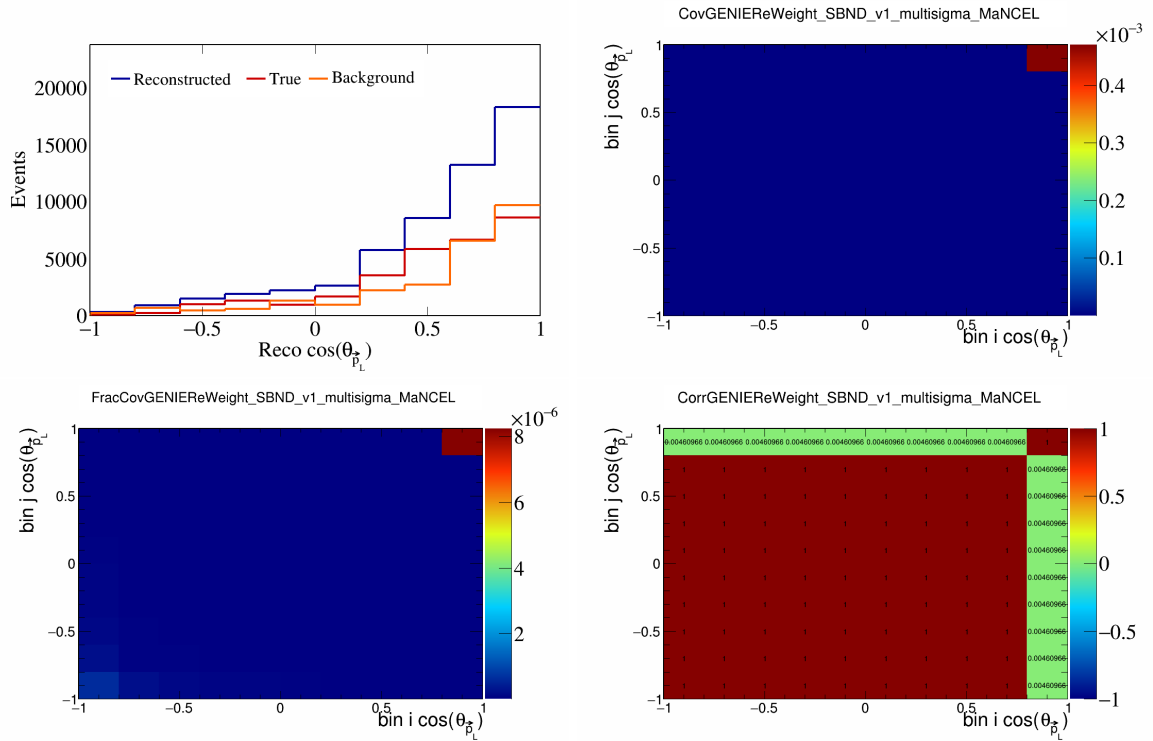


Figure 55: GenieMaNCEL variations for $\cos(\theta_{\vec{p}_L})$.

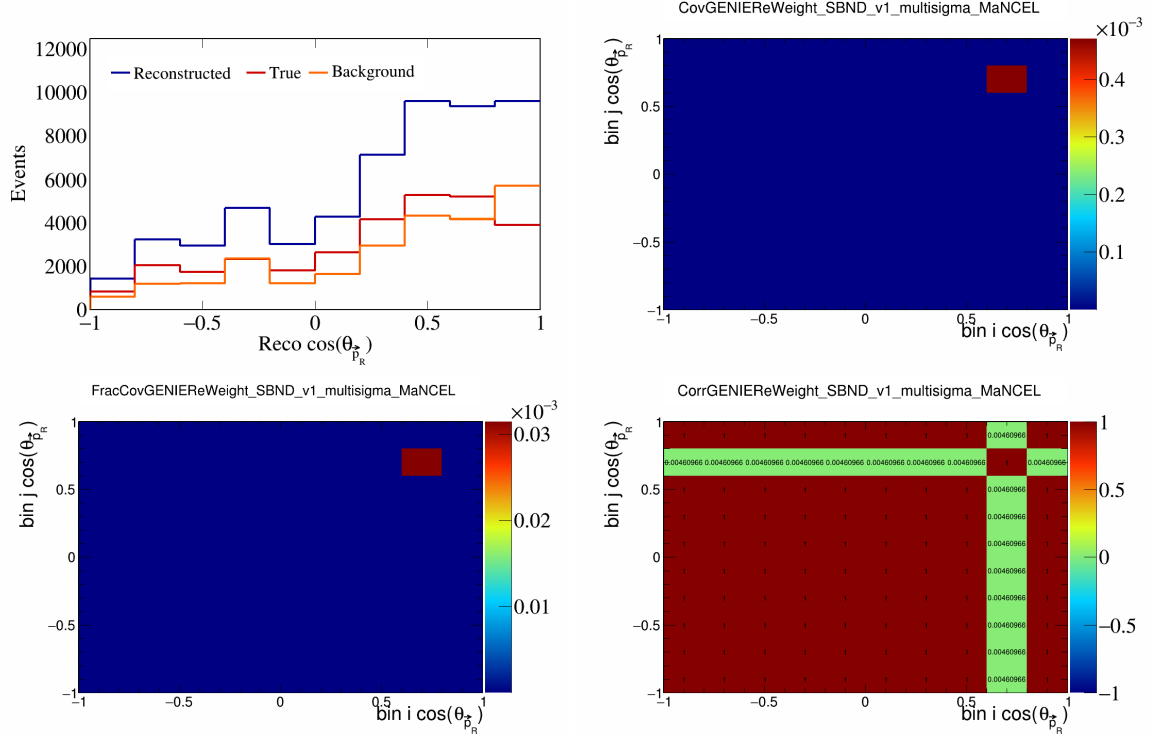


Figure 56: GenieMaNCEL variations for $\cos(\theta_{\vec{p}_R})$.

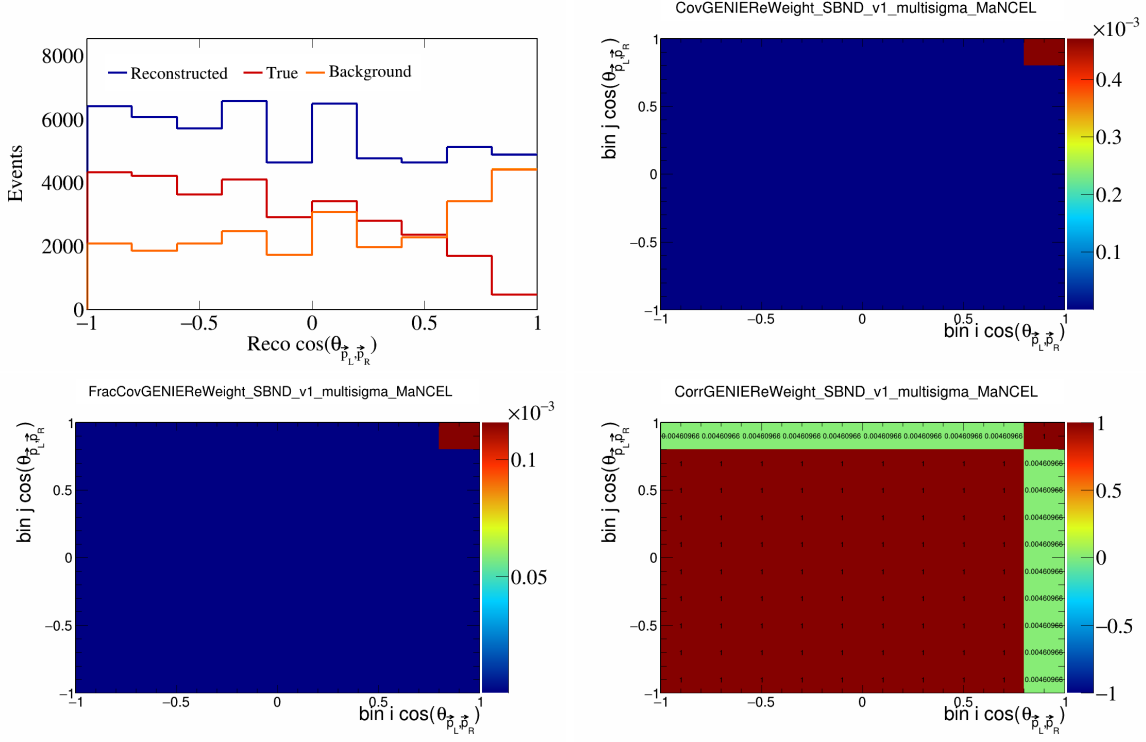


Figure 57: GenieMaNCEL variations for $\cos(\theta_{\vec{p}_L, \vec{p}_R})$.

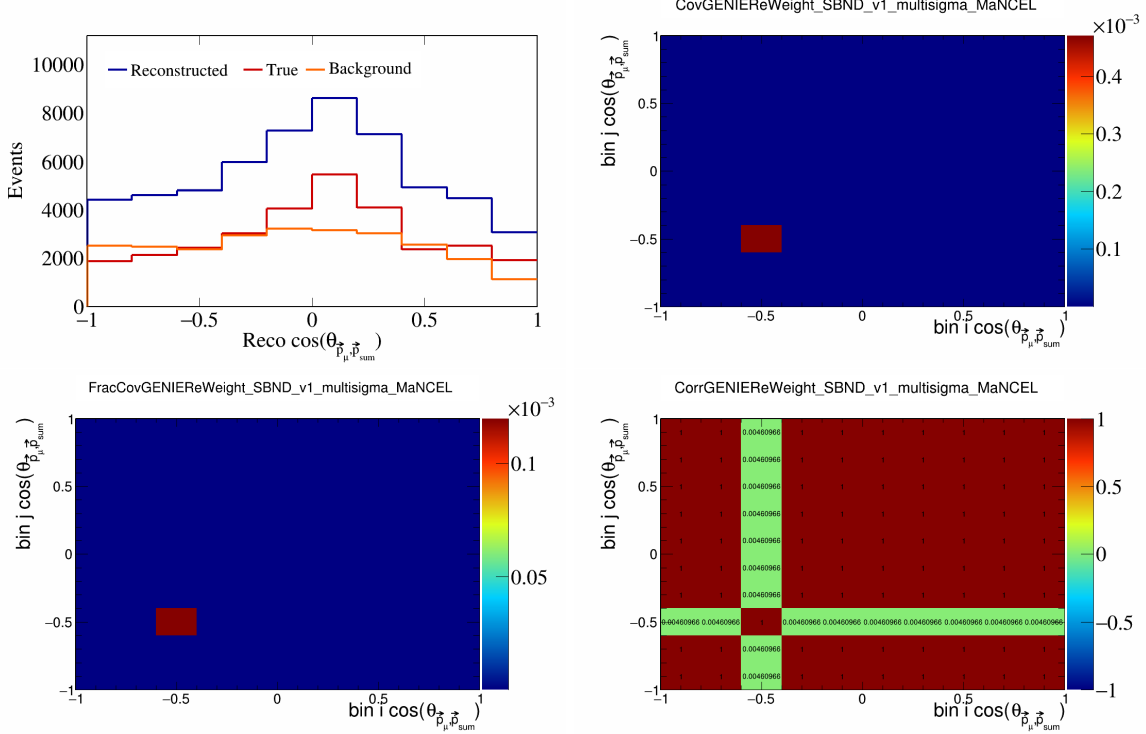


Figure 58: GenieMaNCEL variations for $\cos(\theta_{\vec{p}_\mu, \vec{p}_{\text{sum}}})$.

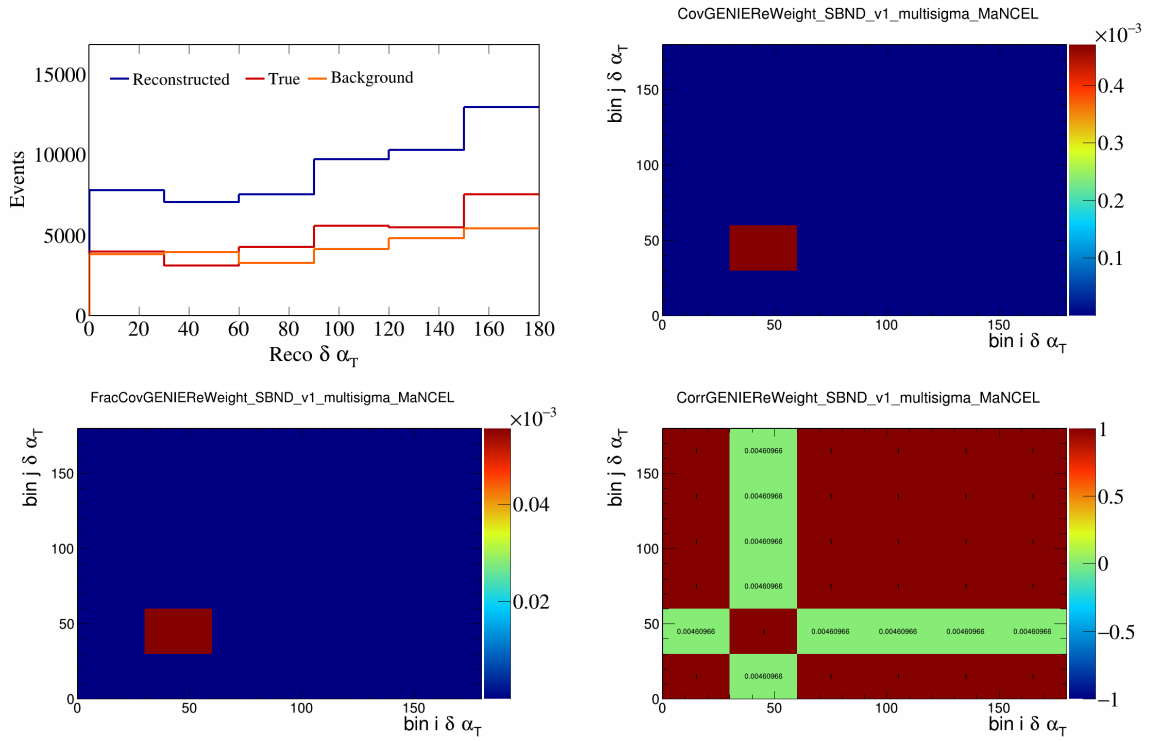


Figure 59: GenieMaNCEL variations for $\delta\alpha_T$.

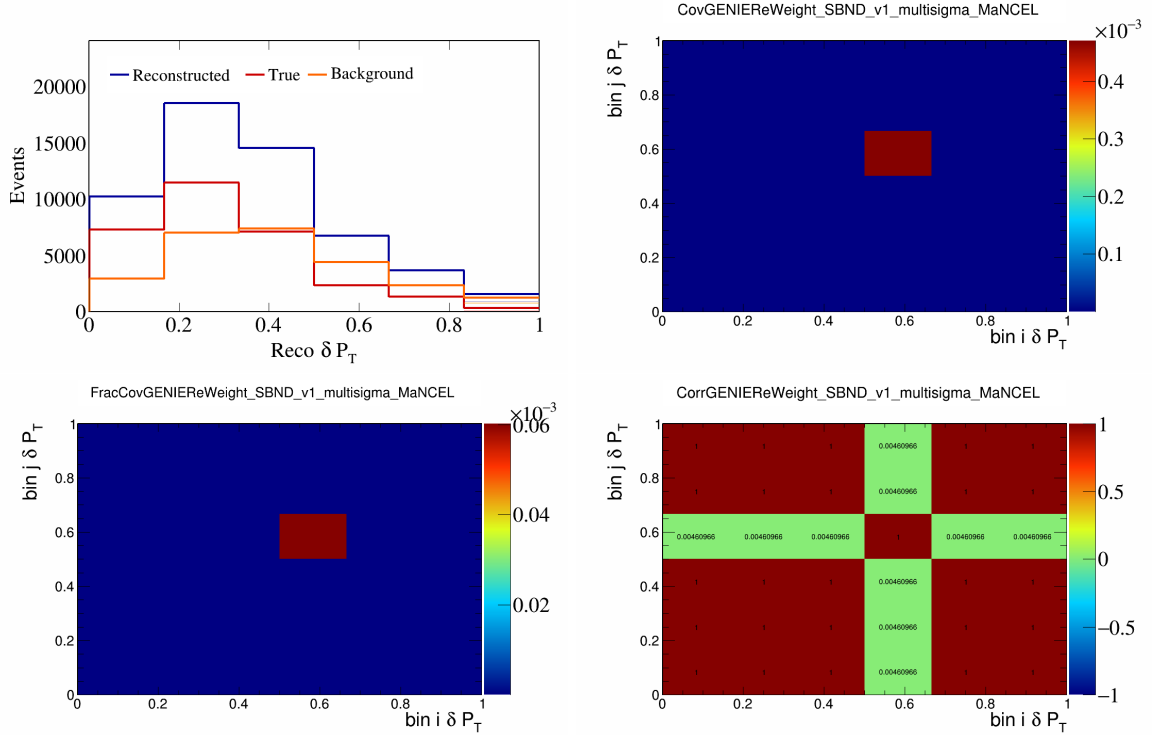


Figure 60: GenieMaNCEL variations for δP_T .

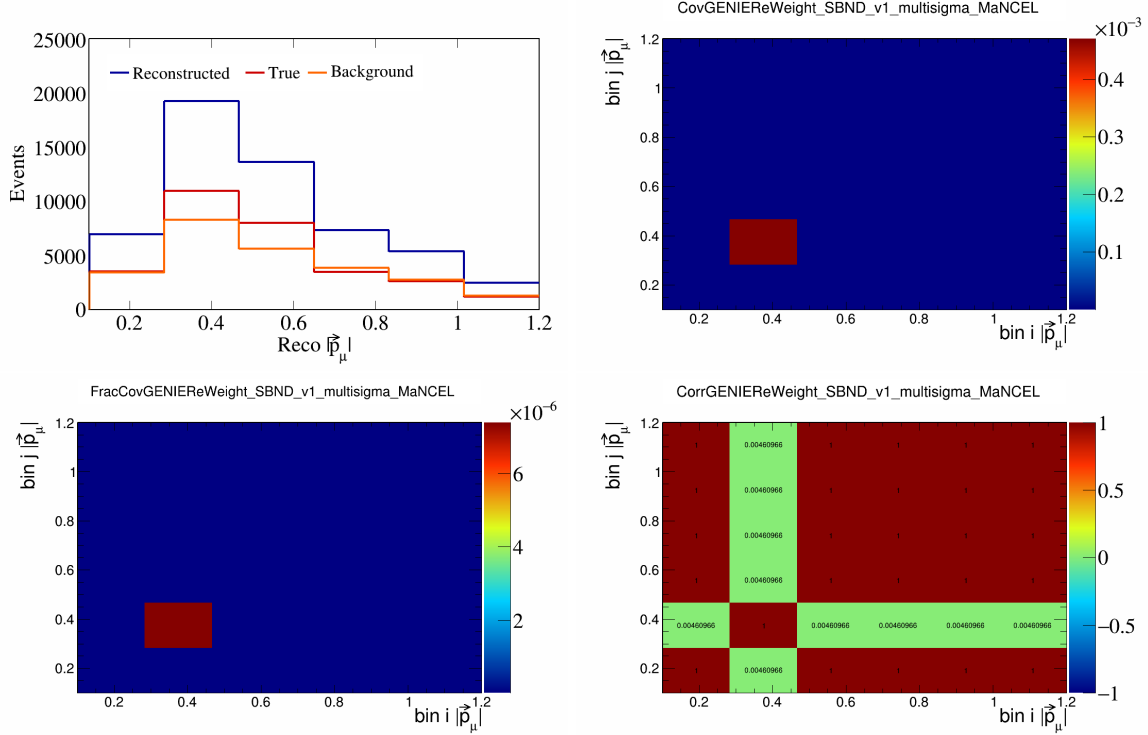


Figure 61: GenieMaNCEL variations for $|\vec{p}_\mu|$.

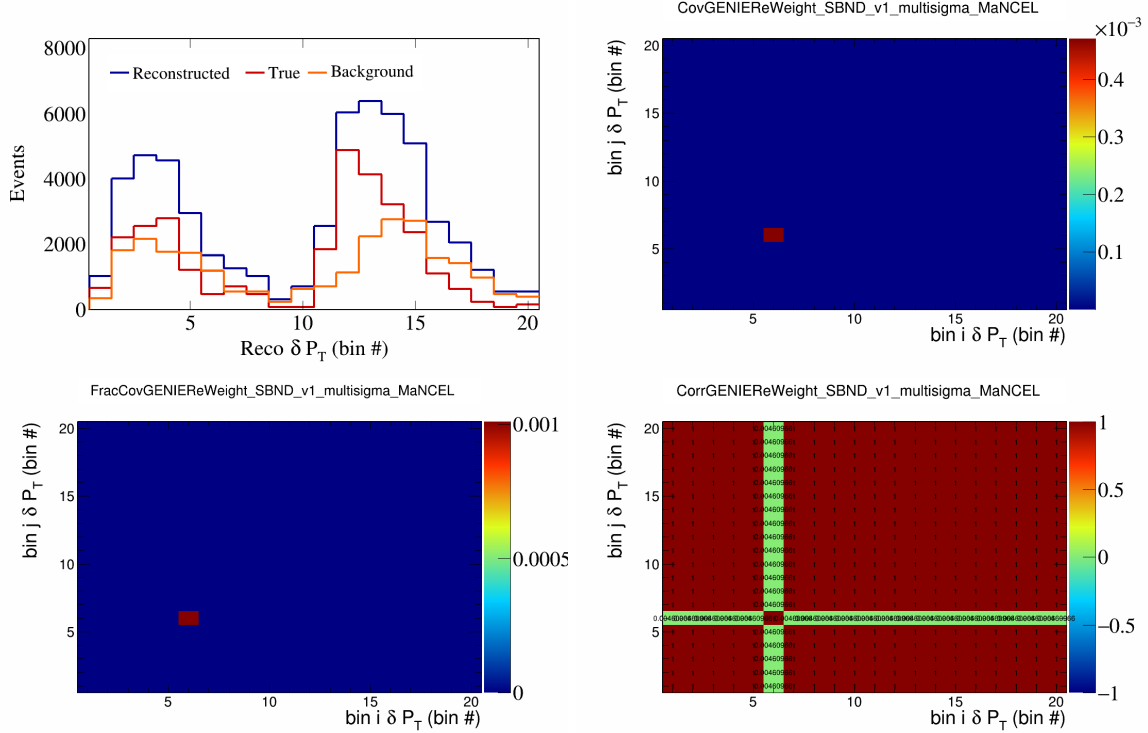


Figure 62: GenieMaNCEL variations for δP_T in $\cos(\theta_{\vec{p}_\mu})$.

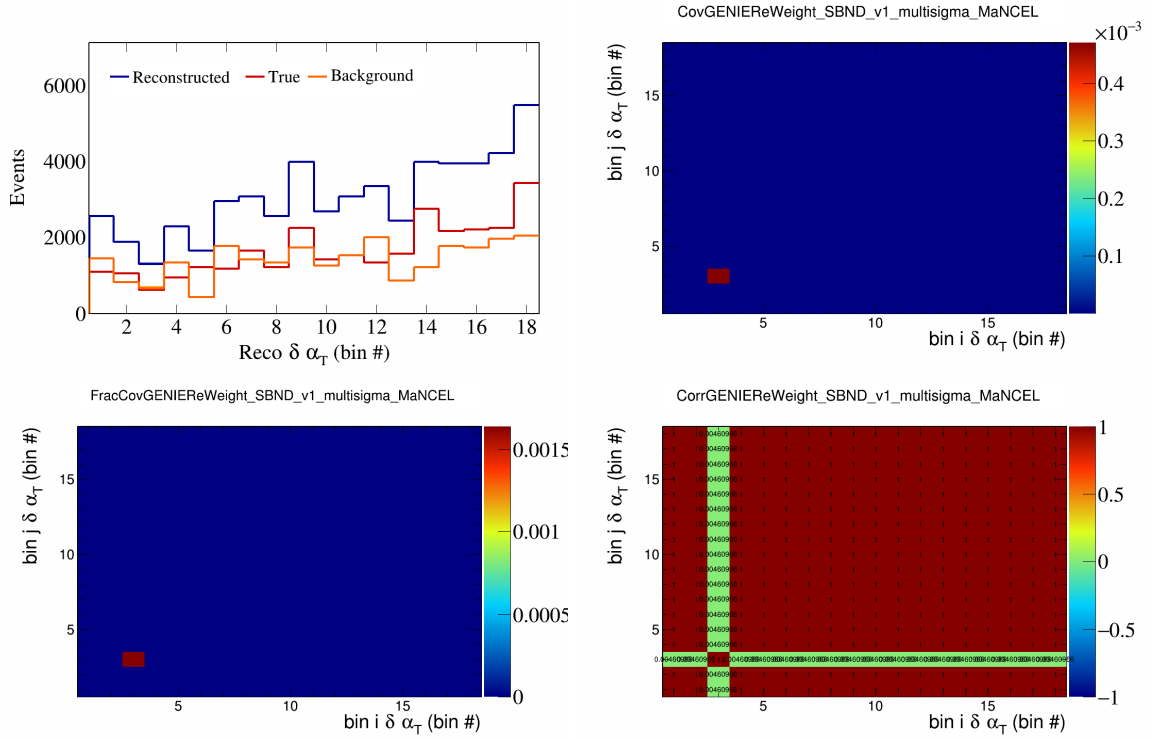


Figure 63: GenieMaNCEL variations for $\delta\alpha_T$ in $\cos(\theta_{\vec{p}_\mu})$.

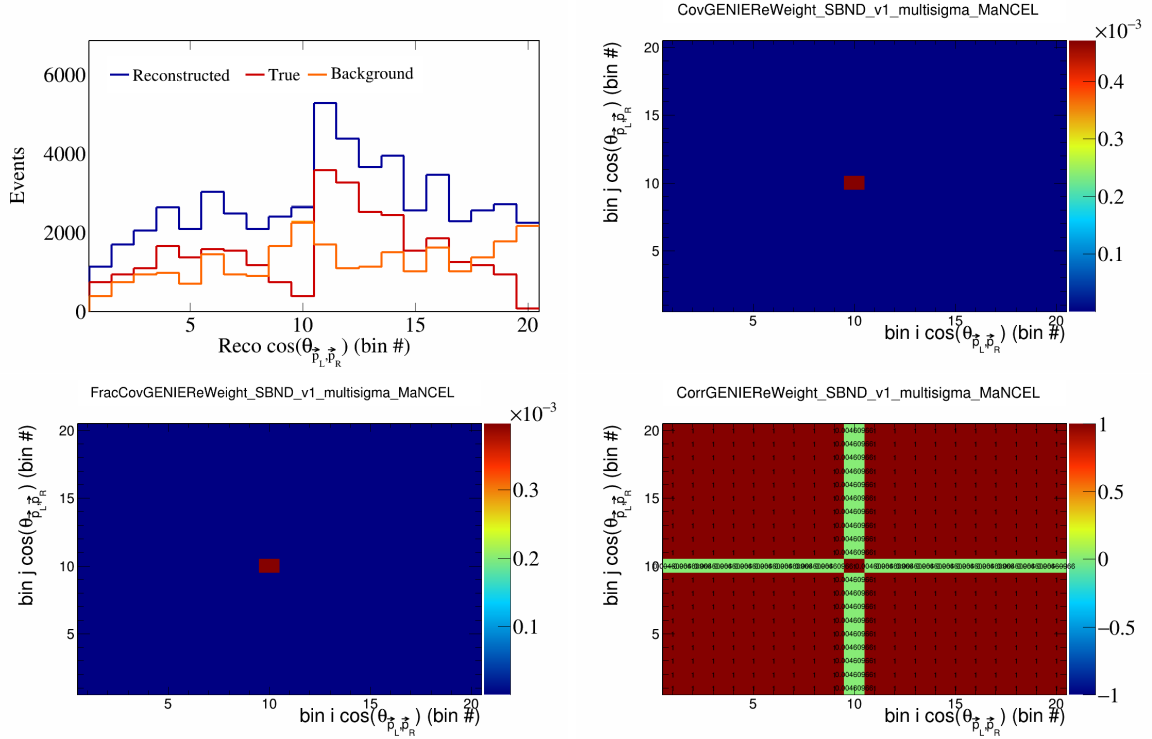


Figure 64: GenieMaNCEL variations for $\cos(\theta_{\vec{p}_L, \vec{p}_R})$ in $\cos(\theta_{\vec{p}_\mu})$.

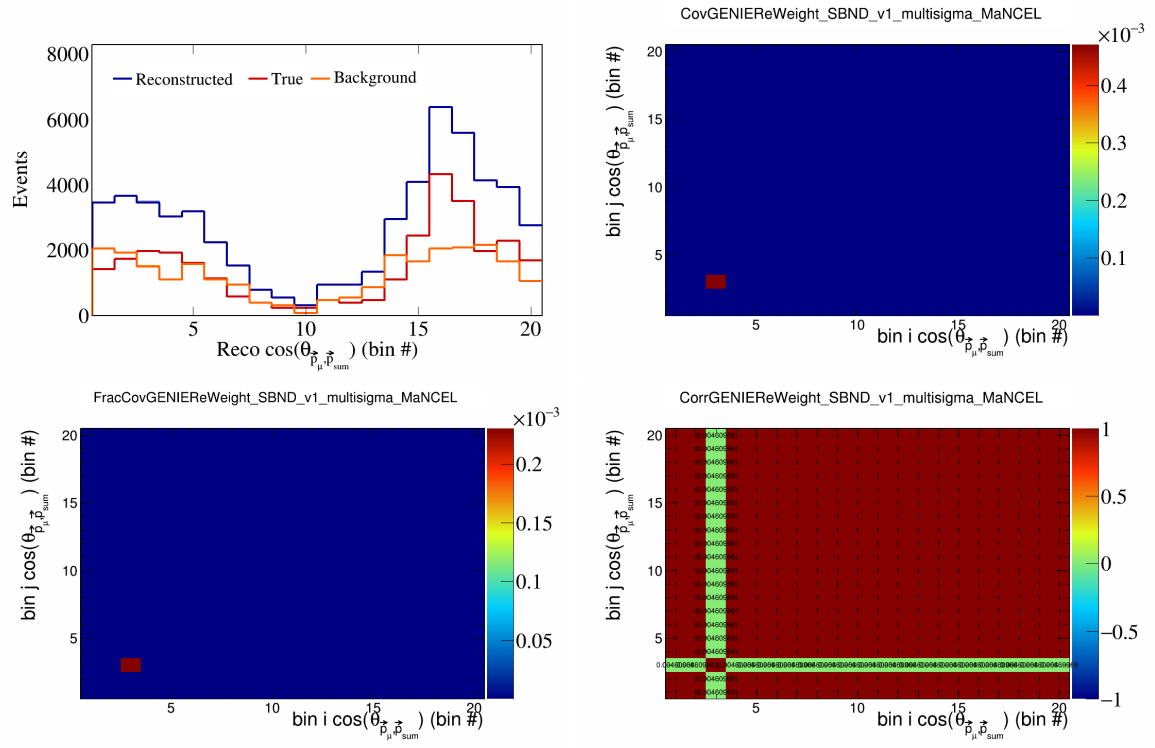


Figure 65: GenieMaNCEL variations for $\cos(\theta_{\vec{p}_\mu, \vec{p}_{\text{sum}}})$ in $\cos(\theta_{\vec{p}_\mu})$.

201 **7 References**

- 202 [1] R. Acciarri, C. Adams, J. Asaadi, B. Baller, T. Bolton, C. Bromberg, F. Cavanna, E. Church, D. Edmunds, A. Ereditato, S. Farooq, B. Fleming, H. Greenlee, G. Horton-Smith, C. James, E. Klein, K. Lang, P. Laurens, R. Mehdiyev, B. Page, O. Palamara, K. Partyka, G. Rameika, B. Rebel, M. Soderberg, J. Spitz, A. M. Szelc, M. Weber, T. Yang, and G. P. Zeller. Detection of back-to-back proton pairs in charged-current neutrino interactions with the argoneut detector in the numi low energy beam line. *Phys. Rev. D*, 90:012008, Jul 2014.
- 203 [2] C. Andreopoulos, A. Bell, D. Bhattacharya, F. Cavanna, J. Dobson, S. Dytman, H. Gallagher, P. Guzowski, R. Hatcher, P. Kehayias, A. Meregaglia, D. Naples, G. Pearce, A. Rubbia, M. Whalley, and T. Yang. The genie neutrino monte carlo generator. *Nuclear Instruments and Methods in Physics Research Section A: Accelerators, Spectrometers, Detectors and Associated Equipment*, 614(1):87–104, 2010.
- 213 [3] Costas Andreopoulos, Christopher Barry, Steve Dytman, Hugh Gallagher, Tomasz Golan, Robert Hatcher, Gabriel Perdue, and Julia Yarba. The genie neutrino monte carlo generator: Physics and user manual, 2015.
- 216 [4] D. Ashery, I. Navon, G. Azuelos, H. K. Walter, H. J. Pfeiffer, and F. W. Schlepütz. True absorption and scattering of pions on nuclei. *Phys. Rev. C*, 23:2173–2185, May 1981.
- 218 [5] P. S. Auchincloss, R. Blair, C. Haber, E. Oltman, W. C. Leung, M. Ruiz, S. R. Mishra, P. Z. Quintas, F. J. Sciulli, M. H. Shaevitz, W. H. Smith, F. S. Merritt, M. Oreglia, P. Reutens, R. Coleman, H. E. Fisk, D. Levinthal, D. D. Yovanovitch, W. Marsh, P. A. Rapidis, H. B. White, A. Bodek, F. Borcherding, N. Giokaris, K. Lang, and I. E. Stockdale. Measurement of the inclusive charged-current cross section for neutrino and antineutrino scattering on isoscalar nucleons. *Zeitschrift für Physik C Particles and Fields*, 48(3):411–431, Sep 1990.
- 224 [6] Ch. Berger and L. M. Sehgal. Lepton mass effects in single pion production by neutrinos. *Phys. Rev. D*, 76:113004, Dec 2007.
- 226 [7] Ch. Berger and L. M. Sehgal. Partially conserved axial vector current and coherent pion production by low energy neutrinos. *Phys. Rev. D*, 79:053003, Mar 2009.
- 228 [8] B. Bourguille, J. Nieves, and F. Sánchez. Inclusive and exclusive neutrino-nucleus cross sections and the reconstruction of the interaction kinematics. *Journal of High Energy Physics*, 2021(4):4, Apr 2021.
- 230 [9] R.C. Carrasco and E. Oset. Interaction of real photons with nuclei from 100 to 500 mev. *Nuclear Physics A*, 536(3):445–508, 1992.
- 232 [10] R. Cruz-Torres, D. Lonardoni, R. Weiss, N. Barnea, D. W. Higinbotham, E. Piasetzky, A. Schmidt, L. B. Weinstein, R. B. Wiringa, and O. Hen. Many-body factorization and position-momentum equivalence of nuclear short-range correlations. *Nature Phys.*, 17(3):306–310, 2021.
- 235 [11] Jonathan Engel. Approximate treatment of lepton distortion in charged-current neutrino scattering from nuclei. *Phys. Rev. C*, 57:2004–2009, Apr 1998.
- 237 [12] T. Golan, J.T. Sobczyk, and J. Źmuda. Nuwro: the wrocław monte carlo generator of neutrino interactions. *Nuclear Physics B - Proceedings Supplements*, 229-232:499, 2012. Neutrino 2010.
- 239 [13] Krzysztof M. Graczyk and Jan T. Sobczyk. Form factors in the quark resonance model. *Phys. Rev. D*, 77:053001, Mar 2008.
- 241 [14] Yoshinari Hayato and Luke Pickering. The neut neutrino interaction simulation program library. *The European Physical Journal Special Topics*, 230(24):4469–4481, Dec 2021.
- 243 [15] Teppei Katori. Meson exchange current (MEC) models in neutrino interaction generators. *AIP Conference Proceedings*, 1663(1):030001, 05 2015.

- 245 [16] Konstantin S. Kuzmin, Vladimir V. Lyubushkin, and Vadim A. Naumov. Lepton polarization in neutrino–nucleon interactions. *Modern Physics Letters A*, 19(38):2815–2829, 2004.
- 246
- 247 [17] T. Leitner, L. Alvarez-Ruso, and U. Mosel. Charged current neutrino-nucleus interactions at intermediate energies. *Phys. Rev. C*, 73:065502, Jun 2006.
- 248
- 249 [18] C.H. Llewellyn Smith. Neutrino reactions at accelerator energies. *Physics Reports*, 3(5):261–379, 1972.
- 250 [19] Selection of numu charged current induced interactions with $N > 0$ protons and performance of events with $N = 2$ protons in the final state in the MicroBooNE detector from the BNB, Oct 2018.
- 251
- 252 [20] First Extraction of Single Differential Cross-Sections on Argon for CC1 μ 2p0 π Event Topologies in the MicroBooNE Detector. May 2022.
- 253
- 254 [21] Ulrich Mosel. Neutrino event generators: foundation, status and future. *Journal of Physics G: Nuclear and Particle Physics*, 46(11):113001, Sep 2019.
- 255
- 256 [22] J. Nieves, J. E. Amaro, and M. Valverde. Inclusive quasielastic charged-current neutrino-nucleus reactions. *Phys. Rev. C*, 70:055503, Nov 2004.
- 257
- 258 [23] J. Nieves, F. Sánchez, I. Ruiz Simo, and M. J. Vicente Vacas. Neutrino energy reconstruction and the shape of the charged current quasielastic-like total cross section. *Phys. Rev. D*, 85:113008, Jun 2012.
- 259
- 260 [24] J. Nieves, I. Ruiz Simo, and M. J. Vicente Vacas. Inclusive charged-current neutrino-nucleus reactions. *Phys. Rev. C*, 83:045501, Apr 2011.
- 261
- 262 [25] J. Schwehr, D. Cherdack, and R. Gran. Genie implementation of ific valencia model for qe-like 2p2h neutrino-nucleus cross section, 2017.
- 263
- 264 [26] Torbjörn Sjöstrand, Stephen Mrenna, and Peter Skands. Pythia 6.4 physics and manual. *Journal of High Energy Physics*, 2006(05):026, may 2006.
- 265
- 266 [27] Júlia Tena-Vidal, Costas Andreopoulos, Adi Ashkenazi, Christopher Barry, Steve Dennis, Steve Dytman, Hugh Gallagher, Steven Gardiner, Walter Giele, Robert Hatcher, Or Hen, Libo Jiang, Igor D. Kakorin, Konstantin S. Kuzmin, Anselmo Meregaglia, Vadim A. Naumov, Afroditi Papadopoulou, Gabriel Perdue, Marco Roda, Vladyslav Syrotenko, and Jeremy Wolcott. Neutrino-nucleon cross-section model tuning in genie v3. *Phys. Rev. D*, 104:072009, Oct 2021.
- 267
- 268 [28] U. K. Yang and A. Bodek. Parton distributions, d/u , and higher twist effects at high x . *Phys. Rev. Lett.*, 82:2467–2470, Mar 1999.
- 269
- 270
- 271
- 272